PACIFIC EARTHQUAKE ENGINEERING
RESEARCH CENTER

Dynamic Modeling of the UC San Diego NHERI Six-Degree-of-Freedom Large High-Performance Outdoor Shake Table

Chin-Ta Lai
Joel P. Conte

Department of Structural Engineering
University of California at San Diego
La Jolla, California

PEER Report No. 2024/07
Pacific Earthquake Engineering Research Center
Headquarters at the University of California, Berkeley
August 2024

PEER 2024/07
August 2024

Dynamic Modeling of the UC San Diego NHERI Six-Degree-of-Freedom Large High-Performance Outdoor Shake Table

Chin-Ta Lai

Joel P. Conte

Department of Structural Engineering
University of California at San Diego, La Jolla, California

PEER Report 2024/07
Pacific Earthquake Engineering Research Center
Headquarters at the University of California, Berkeley
August 2024

ABSTRACT

The UC San Diego Large High-Performance Outdoor Shake Table (LHPOST), which was commissioned on October 1, 2004 as a shared-use experimental facility of the National Science Foundation (NSF) Network for Earthquake Engineering Simulation (NEES) program, was upgraded from its original one degree-of-freedom (LHPOST) to a six degree-of-freedom configuration (LHPOST6) between October 2019 and April 2022. The LHPOST6 is a shared-use experimental facility of the NSF Natural Hazard Engineering Research Infrastructure (NHERI) program. A mechanics-based numerical model of the LHPOST6 able to capture the dynamics of the upgraded 6-DOF shake table system under bare table condition is presented in this report. The model includes: (i) a rigid body kinematic model that relates the platen motion to the motions of components attached to the platen, (ii) a hydraulic dynamic model that calculates the hydraulic actuator forces based on all fourth-stage servovalve spool positions, (iii) a hold-down strut model that determines the pull-down forces produced by the three hold-down struts, (iv) a 2-D and various 1-D Bouc-Wen models utilized to represent the dissipative forces in the shake table system, and (v) a 6-DOF rigid body dynamic model governing the translational and rotational motions of the platen subjected to the forces from the various components attached to the platen. In this report, the rigid body dynamics is studied utilizing the platen twist (combination of platen translational and rotational velocities) and wrench (combination of force and moment resultants acting on the platen) following principles from the robotic analysis literature. The numerical model of the LHPOST6 is validated extensively using experimental data from the acceptance tests performed following the shake table upgrade, and the model predictions of the shake table system response are found to be consistently in very good agreement with the experimental results for tri-axial and six-axial earthquake shake table tests. The validated mechanics-based numerical model of the LHPOST6 presented in this study can be coupled with finite element models of shake table test specimens installed on the rigid platen to study the dynamic interaction between the shake table system and the specimens. Another important potential use of the model is to improve the motion tracking performance of the LHPOST6 through either off-line tuning of the shake table controller and/or development of more advanced shake table controllers.

Keywords: LHPOST6, six-degree-of-freedom shake table, servo-hydraulic shake table, mechanics-based shake table model, shake table tests, experimental model validation.

ACKNOWLEDGMENTS AND DISCLAIMER

This research study was funded by the National Science Foundation, under Award No. CMMI-1840870, with partial support from the Eric and Johanna Reissner Chair in the Department of Structural Engineering at UC San Diego, for which we are grateful. The opinions, findings, conclusions, and recommendations expressed in this publication are those of the author(s) and do not necessarily reflect the view of the National Science Foundation, Pacific Earthquake Engineering Research (PEER) Center, or the Regents of the University of California.

This research could not have been completed without the support of MTS Systems Corporation and the staff of UC San Diego Englekirk Structural Engineering Center, which houses the NHERI 6-DOF Large High-Performance Outdoor Shake Table (LHPOST6). Mr. Brad Thoen at MTS engaged in multiple insightful discussions about the control aspect of the LHPOST6. Mr. Mike Nemeth at MTS provided detailed and thoughtful explanations about the mechanical and servo-hydraulic components of the LHPOST6. Mr. Michael Baumann, Dr. Glen Grenier, and Mr. Wilbur Khan from MTS operated the LHPOST6 during the commissioning and acceptance tests, generating and organizing the experimental data used in this study.

Many thanks to Dr. Koorosh Lotfizadeh and Mr. Abdullah Hamid from the Englekirk Structural Engineering Center for their support and organizational efforts in completing the commissioning and acceptance tests of the LHPOST6.

CONTENTS

LIST OF TABLES

LIST OF FIGURES

1 INTRODUCTION

Seismic shake tables provide effective ways to study the dynamic response of structural or geotechnical specimens by reproducing earthquake ground motions on the shake table platen. Typically, a shake table is composed of a steel platen to which the specimen is attached, actuators (electric or hydraulic) to drive the platen, and a controller to control/regulate the motion that will be reproduced on the platen. Among all types of shake table systems, servo-hydraulic shake tables are most often used to conduct large- or full-scale experiments and study the large/full-scale specimen dynamics with highly nonlinear or velocity-dependent behaviors that cannot be extrapolated from small-scale or quasi-static tests. UC San Diego large high-performance outdoor shake table (LHPOST) was designed in 2001-2002 to have a six degrees-of-freedom (6-DOFs) motion capability and built in 2002-2004 as a one-degree-of-freedom (1-DOF) shake table (see LHPOST in Figure 1.1(a)) to fit the funding available at the time. The LHPOST was commissioned on October 1, 2004, as a shared-use experimental facility of the National Science Foundation (NSF) Network for Earthquake Engineering Simulation (NEES) program. Since then, many landmark projects were conducted on the LHPOST with its large platen size and high motion capacity. In 2018-2021, with a major equipment grant from the NSF and additional financial resources from UC San Diego, the LHPOST was upgraded to its full 6-DOF motion capability (see LHPOST6 in Figure 1.1(b)) by increasing the capacity of the hydraulic power system and the number of actuators and hold-down struts [Van Den Einde et al. 2021]. More specifically, the 6-DOF upgrade was achieved by adding: (1) two pump sets and increasing the accumulator bank volume from 9500 liters to 36900 liters, (2) two horizontal linear actuators and rearranging them in V-shape configuration with the two existing and refurbished actuators, (3) a new high-flow and high-speed servovalve to each vertical actuator, and (4) a third hold-down strut under the center of the platen. The LHPOST6 reopened for operations in April 2022, as the world's highest payload capacity 6-DOF shake table.

The main objective of using a shake table system is to reproduce earthquake ground motions as accurately as possible, and the signal tracking performance of a shake table (i.e., how close is the achieved/feedback motion of the platen to the reference/input signal time histories) can be assessed in many ways (e.g., time-domain approach by calculating the root mean square error between the reference and feedback signals, and frequency-domain methods by comparing the Fourier spectra or response spectra of the reference and feedback signals) [Chen et al. 2018; Guo et al. 2019]. Given the complexity of a shake table dynamic system and the various sources of nonlinearities within the system components, the signal reproduction of a shake table remains imperfect. Previous studies identified and described the main sources of nonlinearity in a shake table system (e.g., servo-hydraulic nonlinearity, friction and other energy dissipation mechanisms, geometric nonlinearities due to changes in configuration of the platen and other components, and the interaction between the table and nonlinear specimens attached to the table, etc.) [Kusner et al. 1992; Chase et al. 2005; Ozcelik et al. 2008]. The signal tracking performance of a shake table is deteriorated by the linear dynamics and the various sources of nonlinearity of the shake table system, if not compensated for [Luco et al. 2010]. To improve the signal tracking performance, the most widely used practical overall strategy utilizes the following steps [Guo et al. 2019]: (1) identify the linear dynamic transfer function of the shake table by running low-amplitude white noise tests on the system (table with mounted specimen) assumed to be linear, (2) tune the controller based on the linear dynamic transfer function, (3) perform several iterations by iteratively modifying the drive file (i.e., conditioning the input to the shake table controller) to minimize the error (from the nonlinear sources of signal distortion) between the reference and feedback table motion signals and obtain the optimized drive signal for earthquake ground motion reproduction at a reduced scale (small enough to prevent damage to the specimen), and (4) scale up the optimized drive signal to reproduce the earthquake ground motion at the desired/target scale. However, this strategy is based on the assumption that the dynamics of the "shake table – specimen" combined system is linear, which is not the case, and the resulting accuracy in signal reproduction may not be sufficient. Therefore, a comprehensive study of the shake table system (here LHPOST6) through detailed nonlinear modeling and simulation is necessary since the actual system dynamics cannot be extrapolated from a linear transfer function that is identified using low-amplitude white noise excitation about the control zero-position of the platen.

A limited number of studies focused on modeling and dynamic analysis of entire seismic shake table systems. Dyke et al. [1995] studied the dynamic coupling between a small, uni-axial shake table system and a specimen mounted on the table and developed a linear model for both the servo-hydraulic system and the specimen. Conte and Trombetti [2000] developed a linear model of a small, uni-axial shake table system by constructing the transfer functions representing the three-stage servovalve, hydraulic actuator, PID with feed-forward and delta-pressure feedback controller, shake table dynamics involving the foundation compliance effects, and linear multi-degree-of-freedom specimen dynamics. Thoen and Laplace [2004] presented a comprehensive dynamic model of a bi-axial medium-size shake table for the purpose of tuning the controller and shaping the time histories offline. Their shake table system model includes the servovalve spool dynamics, a nonlinear servo-hydraulic actuator model, an accumulator model based on the adiabatic gas law, a linear specimen model, and a visco-plastic friction model. Plummer [2008] developed a bare-table model of a $5\text{m} \times 5\text{m}$ 6-DOF shake table accounting for the hydraulic system nonlinearities and joint frictions. An approximating linear model derived from his nonlinear model was used to identify the model parameters. Ozgur et al. [2021] developed a comprehensive numerical model of the LHPOST (in its 1-DOF configuration) by considering the nonlinear dynamics of the hydraulic components, Coulomb friction and nonlinear viscous properties of the energy dissipation mechanisms and approximating the hold-down struts as linear springs acting on the platen. However, this model applies to an obsolete configuration of the LHPOST, and hence a comprehensive model is needed for the new 6-DOF configuration of the LHPOST, i.e., the LHPOST6, which is the main objective and innovation of this report.

An important source of (geometric) nonlinearity comes from the change of geometric configuration of the actuators during a shake table test. Most six-degree-of-freedom shake tables and (e.g., flight) simulators are built as Stewart platforms (a platen driven by six linear actuators) [Dasgupta et al. 2000; Huang et al. 2016; Lai et al. 2022] or following similar designs (e.g., a platen driven by more than six linear actuators) [Airouche et al. 2014; Nakashima et al. 2018; Suzuki et al. 2018]. In the past three decades, numerous studies have focused on the analytical formulation of the equations of motion of Stewart platforms using different methods such as the Newton-Euler approach [Dasgupta and Mruthvunjava 1998; Harib and Srinivasan 2003; Kyrgic and Vidakovic 2020], Lagrangian approach [Lebret et al. 1993; Guo and Li 2006], and Kane's method [Liu et al. 2000; Asadi and Sadati 2018]. Among these approaches, the Newton-Euler approach, which will be used in the study presented herein, is the most straightforward method with the advantage of higher numerical efficiency and less computational complexity of the associated numerical solution methods [Kyrgic and Vidakovic 2020]. However, to achieve the LHPOST6 high payload capacity and corresponding high overturning moment capacity, the vertical, roll (rotation about the longitudinal axis of the platen) and pitch (rotation about the transversal axis of the platen) table motions are mainly driven by six single-acting, compact vertical actuators with pressure balanced bearings, which makes the LHPOST6 a very unique shake table actively driven by four linear horizontal actuators and six vertical actuators with pressure balanced bearings and passively reacted against by three pneumatic actuators (i.e, hold-down struts). The modeling of this unique design and configuration of the LHPOST6 is at the heart of this report. This report uses the twist and wrench representation from modern robotics [Featherstone 2014; Lynch and Park 2017] to efficiently study the 3D rigid body kinematics and dynamics of the shake table platen and components attached to it. Meanwhile, the kinematics of the horizontal linear actuators and hold-down struts are similar to that of the actuators in Stewart platforms, while the pressure balanced bearings on top of the vertical actuators form a smooth surface for the platen to slide on and require a different kinematic model than the other actuators.

The main objective and innovative contribution of this report is to develop a high-fidelity mechanics-based numerical model of the LHPOST6 under bare table condition with full 6-DOF dynamics. The LHPOST6 is a unique shake table system in view of its very large payload capacity and dynamic system complexity. The twist and wrench representation borrowed from modern robotics is used as an effective, elegant, and innovative approach to study the kinematics and dynamics of a 6-DOF shake table system. Chapter 2 provides the system configuration and performance characteristics of the LHPOST6. Then, Chapters 3 and 4 focus on the kinematics and dynamics of the LHPOST6 open-loop model. Chapter 3 presents the kinematics of the shake table platen and components connected to it, namely the horizontal actuators, vertical actuators with pressure balanced bearings, and hold-down struts. Chapter 4 focuses on the dynamic modeling of the components in the open-loop system, including the hydraulic dynamics, actuator and hold-down strut dynamics, energy dissipation mechanisms in the system, and 3D rigid body dynamics of the platen. Chapter 5 describes the controller, including the control algorithm, of the LHPOST6 provided by MTS Systems Corporation, presents the Matlab-Simulink implementation of the LHPOST6 open-loop model, and discusses the closed-loop system consisting of the open-loop model and the controller. The three-step experimental validation of the numerical model of the LHPOST6 is the subject of Chapter 6, and the conclusions are provided in Chapter 7.

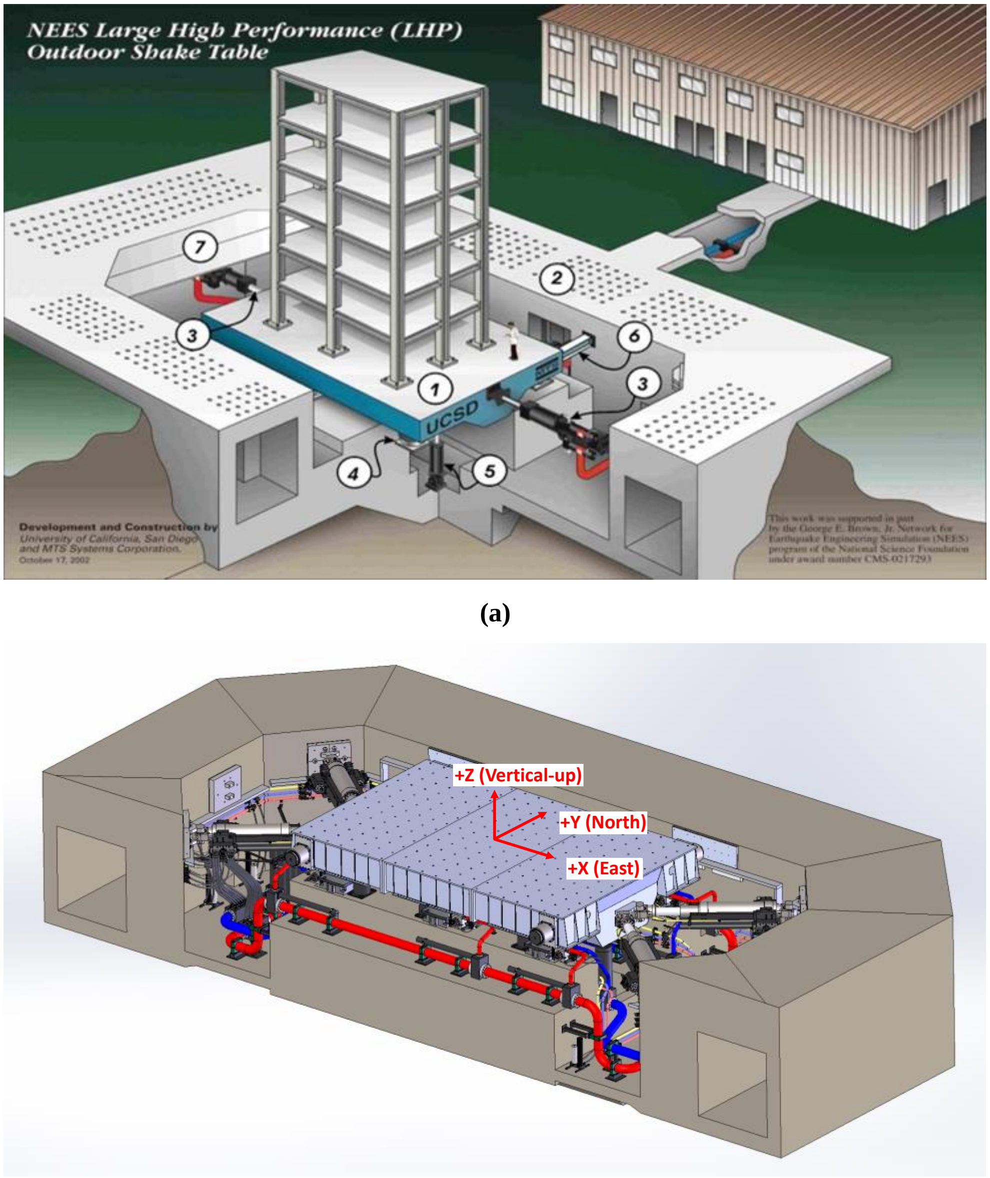

(a)

(b)

Figure 1.1 Schematic picture of (a) the 1-DOF LHPOST before the upgrade and (b) the 6-DOF LHPOST6 after the upgrade. Subfigure (b) includes the fixed inertial reference frame originated at the geometric center of the top surface of the platen in its control zero-position.

2 DESCRIPTION OF THE LHPOST6

2.1 SYSTEM CONFIGURATION OF LHPOST6

A detailed historical introduction of the UC San Diego NEES/NHERI LHPOST and its upgrade to 6-DOFs are provided in [Van Den Einde et al. 2021]. The mechanical components attached to the shake table platen (see Figure 3.1) can be categorized into three types: (1) four horizontal linear actuators able to drive the platen horizontally along the longitudinal (or X), transversal (or Y), and yaw (rotation about Z axis) DOFs (see Figure 1.1). Each one of them is connected to the platen through its front (or platen) swivel and to the reaction mass through its base (or back) swivel. (2) Six vertical actuators with pressure balanced bearings which can drive the platen along the vertical (or Z), roll (rotation about the longitudinal X axis), and pitch (rotation about the transversal Y axis) DOFs. The pressure balanced bearings on top of the vertical actuators create a sliding surface with a hydraulic oil film for the platen to move with very low friction. (3) Three cylinders pre-charged with nitrogen gas in their bottom chamber (referred to in this report as hold-down struts or HDS in short). Each hold-down strut applies a large downward vertical force on the platen to provide the large overturning moment capacity of the LHPOST6. Unlike the horizontal and vertical servo-hydraulic actuators, the HDSs are passive pneumatic components. The type of kinematics between the platen and the components and the source of force generation by the components are summarized in Table 2.1. Meanwhile, the components in Table 2.1 are numbered by an index *i* to facilitate presentation and discussion in the following chapters.

Table 2.1 Type of kinematics between the components and the platen and source of force generation by the components

Components	Kinematics	Force generated by	Control	Number	Numbering
Horizontal Actuators	Linear actuators	Hydraulic pressure	Active	4	$i = 1, 2, 3, 4$
Vertical Actuators	Sliding surfaces	Hydraulic pressure	Active	6	$i = 5, 6, \ldots, 10$
Hold-down Struts	Linear actuators	Pre-charged nitrogen	Passive	3	$i = 11, 12, 13$

2.2 PERFORMANCE CHARACTERISTICS OF LHPOST6

The uniaxial performance characteristics of the LHPOST6 under sinusoidal motions (peak displacement, velocity, acceleration along each of the six DOFs) under both bare table condition and with a 4.9 MN rigid payload centered on the platen are reported in Table 2.2. According to the capacity of the actuators and the actuator configuration, the LHPOST6 is able to move dynamically ± 0.89 m (35 in) in the longitudinal direction. However, its travel range in the transversal direction is only ± 0.38 m (15 in) due to the geometry of the transverse cross-section of the reaction mass and the platen, and the location of the vertical actuators. The travel range of the platen in the vertical direction is determined by the stroke of the vertical actuators, which is ± 0.127 m (±5 in). The velocity capacities of the LHPOST6 depend on the flow capacities of the servovalves feeding the horizontal and vertical hydraulic actuators; they are 3.0 m/s (118 in/s), 2.0 m/s (80 in/s), and 0.45 m/s (17 in/s) in the longitudinal, transverse and vertical directions, respectively. With a centered rigid payload of 4.9 MN, the velocity capacity in the vertical direction increases to 0.55 m/s (21.7 in/s). The acceleration capacities of the LHPOST6 are determined by the hydraulic pressure supplied to the servovalves by the hydraulic system, the piston areas of the actuators, the mass of the platen, and the mass of the moving parts of the components attached to the platen; they are 3.7 g, 1.85 g, and 3.6 g in the longitudinal, transverse and vertical directions, respectively. The rotation, angular velocity, and angular acceleration capacities for each of the three rotational DOFs (roll, pitch and yaw) are also provided in Table 2.2.

Table 2.2 Uniaxial performance characteristics of the LHPOST6 under sinusoidal motions.

Platen size	12.2 m × 7.6 m (40 ft × 25 ft)					
Freq. Bandwidth	0 – 33 Hz					
Payload Capacity	20 MN (4500 kips)					
	Sinusoidal motions – Bare table condition			Sinusoidal motions – Centered rigid payload of weight = 4.9 MN (1100 kips)		
	Translational X (E-W)	Translational Y (N-S)	Translational Z (Vertical)	Translational X (E-W)	Translational Y (N-S)	Translational Z (Vertical)
Peak Displacement	± 0.89 m (± 35 in)	± 0.38 m (± 15 in)	± 0.127 m (±5 in)	± 0.89 m (± 35 in)	± 0.38 m (± 15 in)	± 0.127 m (±5 in)
Peak Velocity	3.0 m/s (118 in/s)	2.0 m/s (80 in/s)	0.45 m/s (17 in/s)	3.0 m/s (118 in/s)	2.0 m/s (80 in/s)	0.55 m/s (21 in/s)
Peak Acceleration	(5.8 g)(1) 3.7 g(2)	(4.7 g)(1) 1.85 g(2)	-3.6 g +31.1 g(1) +11.9 g(3)	(1.6 g)(1) 1.0 g(2)	(1.25 g)(1) 0.50 g(2)	-1.64 g +7.5 g(1) +2.5 g(2)
Peak Force	10.6 MN(1) (2380 kips)(1) 6.8 MN(2) (1530 kips)(2)	8.38 MN(1) (1890 kips)(1) 3.4 MN(2) (765 kips)(2)	-4.67 MN(4) (1018 kips)(4) +57.0 MN(5) (12800 kips)(5) +22.9 MN(6) (5150 kips)(6)	10.6 MN(1) (2380 kips)(1) 6.8 MN(2) (1530 kips) (2)	8.38 MN(1) (1890 kips)(1) 3.4 MN(2) (765 kips)(2)	-4.3 MN(4) (967 kips)(4) +57.0 MN(5) (12800 kips)(5) +22.9 MN(6) (5150 kips)(6)
	Rotational X (Roll)	Rotational Y (Pitch)	Rotational Z (Yaw)			
Peak Rotation	2.22 deg(7)	1.45 deg(7)	3.80 deg			
Peak Angular Velocity	8.98 deg/s	5.58 deg/s	18.79 deg/s			
Peak Angular Acceleration	772 deg/s^2 (2)	439 deg/s^2 (2)	339 deg/s^2 (2)			

(1) Peak acceleration controlled by the actuator force capacities in the control zero-position of the platen (i.e., without considering the change in geometric configuration of the horizontal actuators due to the motion of the platen).
(2) Acceleration limit controlled by the design strength of the reaction mass until further studies.
(3) Acceleration limit controlled by the design strength of the steel honeycomb platen.
(4) Assuming a pressure of 125 psi in the chamber of each vertical actuator and accounting for the hold-down forces in the control zero-position of the table.
(5) Peak force controlled by the vertical actuator force capacities and accounting for the hold-down forces in the control zero-position of the table.
(6) Force limit controlled by the design strength of the steel honeycomb platen and accounting for the hold-down forces in the control zero-position of the table.
(7) Due to kinematics of the piston seals of the vertical actuators.

3 KINEMATICS OF THE LHPOST6

3.1 Instantaneous Inertial Reference Frames Used to Formulate the Kinematics of the LHPOST6

A proper reference frame system plays an important role in describing the kinematics and dynamics of a system with translational and rotational motions. In general, reference frames may be referred to as inertial or co-moving ones. An inertial reference frame is fixed at a point in space and does not move in time, which is useful for defining the location and/or orientation of a body; while a co-moving frame is moving and rotating with a body, which leads to a more compact description of the dynamics of the body since the mass and mass moment of inertia properties remain constant with respect to a co-moving body-oriented frame. In robotics analysis, the instantaneous inertial reference frame, a more efficient reference frame, was introduced to utilize the advantages and avoid the drawbacks of the inertial and co-moving reference frames.

An instantaneous inertial reference frame is always considered an inertial frame that is motionless (i.e., frozen) at every instant of time when observing the motion of the system, which helps studying the kinematic relations between platen and component displacements at a specific time step. This definition is consistent with that of a conventional inertial frame attached to a fixed point in space and not rotating over time; however, defining an instantaneous inertial frame attached to a body must be done carefully. In the robotics literature, the instantaneous inertial frame attached to a body is defined to coincide with the co-moving body-oriented frame at the instant of time of interest. In this report, the following three major instantaneous inertial reference frames are used to formulate the kinematics of the LHPOST6:

- Frame fixed at the center of the platen top surface (referred to herein as platen surface center) in the control zero-position of the table (defined as fixed point O in space and called global origin) and with fixed orientation. It is denoted as frame {s} and is considered the basic reference frame while defining the other reference frames (see Figure 3.1). The control zero-position is the configuration of the platen when the system is ready for conducting an experiment, which means that the hydraulic pressure was built up, the platen left its parking (or idle) position and moved up 5.25 in. In this study, the control zero-position of the platen also corresponds to the initial condition of the shake table motion simulations presented herein.
- Frame attached to the platen surface center (defined as particle C moving with the platen, i.e., co-moving) with fixed orientation frame (the same as for the global fixed frame) and denoted as frame {c}. This frame updates its origin as the shake table is in operation (see Figure 3.1). This frame is suitable for describing the velocity (translational and angular) of the platen. The incremental translational displacements of the platen relative to the global fixed

frame {s} and the incremental rotations of the platen about the axes of the co-moving frame {c} can be directly obtained from the velocity (translational and angular) of the platen expressed in frame {c}.

- Body-oriented frame attached to the center of gravity of the platen (defined as particle B moving with the platen; the C.G. of the platen considers the moving masses of the horizontal and vertical actuators and of the hold-down struts): this frame, referred to as frame {b}, updates both its origin and orientation as the shake table is in operation (see Figure 3.1). This is the proper frame for studying the 3-D rigid body dynamics of the platen since the inertial properties of the platen about the axes of this frame (which are taken as the principal axes of the platen) remain constant during the operation of the shake table.

To analyze and formulate the kinematics and dynamics of the shake table system, a number of additional instantaneous inertial reference frames will be used and are defined in Table 3.1 and Figure 3.1; they are denoted as a lower-case letter inside curly brackets (see first column of Table 3.1) and their origins are denoted as upper-case letters (see fourth column of Table 3.1). Figure 3.1(c) shows the different reference frames used to study the relative motion between the platen and components for friction modeling. The orientation of a reference frame is commonly described by a set of three mutually perpendicular right-handed unit vectors. These vectors, forming a basis of 3D vectors, delineate the orientation of the reference frame in three-dimensional space. In this study, a 3D vector itself is a quantity, coordinate-free and denoted by a bold letter, (e.g., $\mathbf{u}$), while its three components expressed in a reference frame are denoted as a bold letter with left superscript (e.g., ${}^{\mathrm{s}}\mathbf{u}$), indicating that the same vector can be expressed in different reference frames and the vector components can be defined as below, considering reference frames {s} and {b} for example:

$$\mathbf{u} = {}^{\mathrm{s}}u_x\,\hat{\mathbf{x}}_{\mathrm{s}} + {}^{\mathrm{s}}u_y\,\hat{\mathbf{y}}_{\mathrm{s}} + {}^{\mathrm{s}}u_z\,\hat{\mathbf{z}}_{\mathrm{s}} = {}^{\mathrm{b}}u_x\,\hat{\mathbf{x}}_{\mathrm{b}} + {}^{\mathrm{b}}u_y\,\hat{\mathbf{y}}_{\mathrm{b}} + {}^{\mathrm{b}}u_z\,\hat{\mathbf{z}}_{\mathrm{b}} \tag{3-1}$$

$${}^{\mathrm{s}}\mathbf{u} = \begin{bmatrix} {}^{\mathrm{s}}u_x & {}^{\mathrm{s}}u_y & {}^{\mathrm{s}}u_z \end{bmatrix}^T, \quad {}^{\mathrm{b}}\mathbf{u} = \begin{bmatrix} {}^{\mathrm{b}}u_x & {}^{\mathrm{b}}u_y & {}^{\mathrm{b}}u_z \end{bmatrix}^T \tag{3-2}$$

where $\hat{\mathbf{x}}_{\mathrm{s}}$, $\hat{\mathbf{y}}_{\mathrm{s}}$, $\hat{\mathbf{z}}_{\mathrm{s}}$ denote the unit vectors along the global reference frame {s}, and $\hat{\mathbf{x}}_{\mathrm{b}}$, $\hat{\mathbf{y}}_{\mathrm{b}}$, $\hat{\mathbf{z}}_{\mathrm{b}}$ denote the unit vectors along the body reference frame {b}. Two time differential operators are also defined here: (1) a dot superimposed on the vector notation (e.g., $\dot{\mathbf{u}}$) denotes the time derivative of the vector, but the components of $\dot{\mathbf{u}}$ can be expressed in different reference frames according to the definition above (e.g., ${}^{\mathrm{s}}\dot{\mathbf{u}}$ or ${}^{\mathrm{b}}\dot{\mathbf{u}}$); (2) the time derivative of the vector components without considering whether the reference frame changes in time, and this operator is written as $\frac{d}{dt}\left({}^{\mathrm{b}}\mathbf{u}\right)$ or simply as $\frac{d}{dt}\,{}^{\mathrm{b}}\mathbf{u}$. Note that when a vector is expressed in the fixed frame {s}, the two time differential operators are equivalent, as the frame {s} remains unchanged over time, which implies that ${}^{\mathrm{s}}\dot{\mathbf{u}} = \frac{d}{dt}\,{}^{\mathrm{s}}\mathbf{u}$.

Table 3.1 Definition of the instantaneous inertial reference frames attached to various components of the shake table system.

	Location updating	Orientation updating	Origin (Notation and definition)		Orientation
$\{s\}$	No	No	O	Fixed at the platen surface center when the platen is in the control zero-position, also defined as the global origin.	X-direction is the E-W direction. Y-direction is the N-S direction. Z-direction is the same as gravity.
$\{c\}$	Yes	No	C	Center of the top surface of the platen.	Same as frame $\{s\}$
$\{b\}$	Yes	Yes	B	Center of gravity of the platen including the moving parts of the horiz. and vertical actuators, and of the HDS.	Same as the principal axes of the platen
$\{p'_i\}$	Yes	No	P'_i	Connection point between the platen and components attached to the platen but on the platen side.	Same as frame $\{s\}$
$\{p_i\}$	Yes	No	P_i	Connection point between the platen and components attached to the platen but on the component side.	Same as frame $\{s\}$
$\{n_i\}$	Yes	Yes	P_i	Connection point between the platen and vertical actuator surface plate.	Same as the principal axes of the vertical actuator surface plate
$\{a_i\}$	No	Yes	A_i	Connection point between the component and the reaction mass.	The X-direction of the frame is the same as the component longitudinal axis. The Y- and Z-direction are aligned with the other two principal axes of the component.

3.2 KINEMATICS OF ROTATIONAL MOTIONS

Using a vector to describe arbitrarily large translational motions is straightforward but large rotational motions cannot be treated vectorially. Three different vector representations of a general rotation matrix are typically used for different purposes:

- *Euler angles*: a general rotation matrix can be decomposed into three elementary rotation matrices multiplied sequentially, with each rotation defined in terms of the rotation angle and the axis of rotation. Among all 12 possible rotation sequences, the intrinsic yaw-pitch-roll (z-y′-x″) rotations sequence is the most widely used. The 12 possible rotation sequences are: x-y′-z″, y-z′-x″, z-x′-y″, x-z′-y″, z-y′-x″, y-x′-z″, and z-x′-z″, x-y′-x″, y-z′-y″, z-y′-z″, x-z′-x″, y-x′-y″.
- *Axis-angle* representation: It is also known in the literature as the *rotation vector* or *pseudo rotation vector* representation. A rotation vector can be decomposed as the

product of a scalar which represents the rotation angle and a unit vector which represents the axis of rotation.

- *Quaternion*: a quaternion is a four-component vector which is typically expressed as the product of the Euclidean norm of this vector and the corresponding unit vector (or unit quaternion). The axis-angle representation of a large rotation can be readily converted into the corresponding unit quaternion. Quaternions are very efficient for analyzing situations where rotations in 3D are involved. Furthermore, the angular velocity in a fixed reference frame can be obtained easily from the time derivative of the quaternion and the use of the quaternion representation does not suffer from the Gimble lock issue (loss of one rotational DOF caused by Euler angles when the pitch is at 90 degrees).

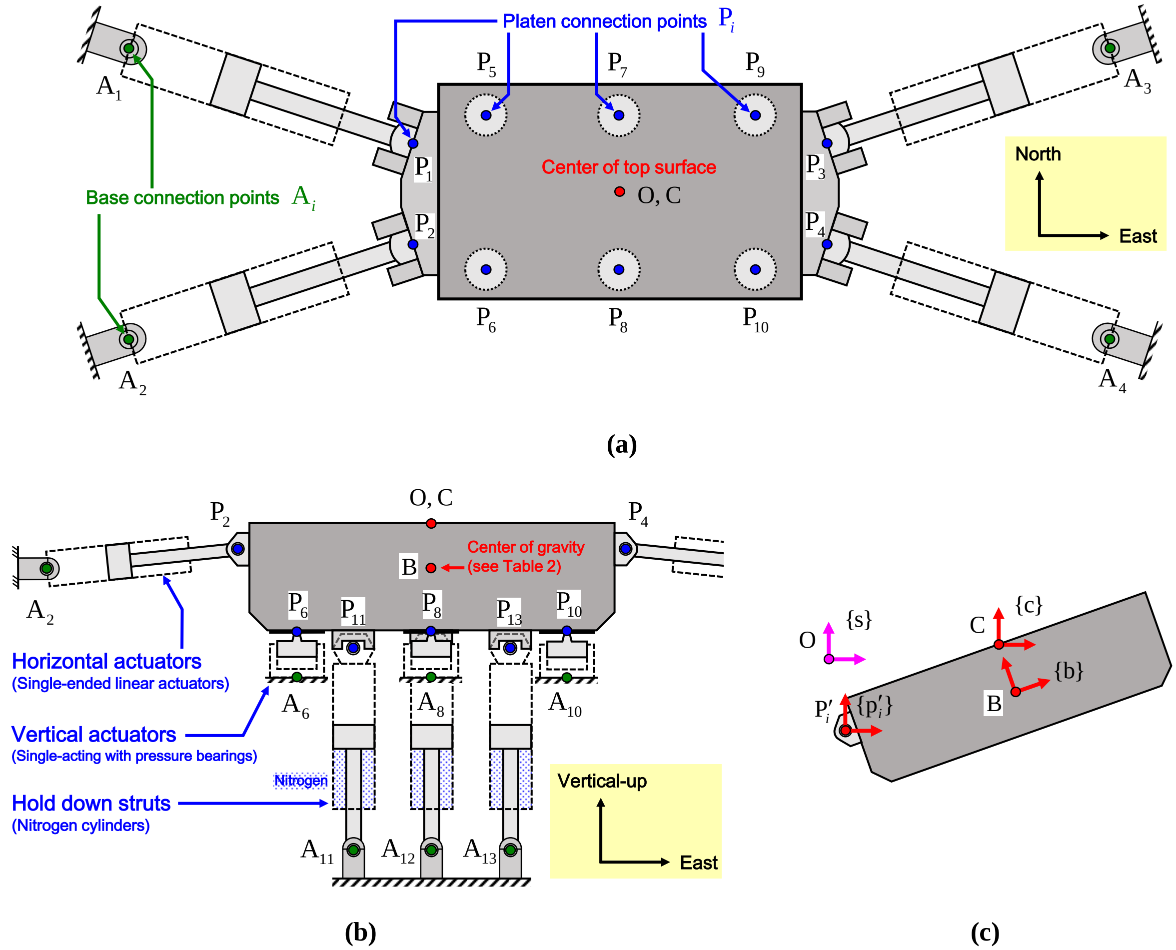

Figure 3.1 **Reference points and instantaneous inertial reference frames used for LHPOST6. Subfigure (a) shows the top view, subfigure (b) shows South view of reference points when the platen is in its control zero-position; and subfigure (c) shows the reference frames attached to the platen in a translated and rotated position.**

3.2.1 Euler Angles

Euler angles are a set of three angles and are often written in vector form, but the vector itself has no special meaning. The rotation matrix is composed of three elementary extrinsic rotation matrices; each of the three extrinsic rotations $\alpha,\ \beta,$ and γ is about the global axes, which has the same direction as the reference frame {s}:

$$
\begin{aligned}
{}^{s}\mathbf{R}_{\hat{x}}(\alpha) &= \begin{bmatrix} 1 & 0 & 0 \\ 0 & \cos\alpha & -\sin\alpha \\ 0 & \sin\alpha & \cos\alpha \end{bmatrix}, \quad \alpha \in [-\pi, \pi] \\
{}^{s}\mathbf{R}_{\hat{y}}(\beta) &= \begin{bmatrix} \cos\beta & 0 & \sin\beta \\ 0 & 1 & 0 \\ -\sin\beta & 0 & \cos\beta \end{bmatrix}, \quad \beta \in [-\pi/2, \pi/2] \\
{}^{s}\mathbf{R}_{\hat{z}}(\gamma) &= \begin{bmatrix} \cos\gamma & -\sin\gamma & 0 \\ \sin\gamma & \cos\gamma & 0 \\ 0 & 0 & 1 \end{bmatrix}, \quad \gamma \in [-\pi, \pi]
\end{aligned}
\tag{3-3}
$$

In this study, the convention of the intrinsic yaw-pitch-roll sequence is used, which defines the three rotation steps: (1) rotate by γ about the z axis (x-y-z represents the fixed reference frame {s}). Then, (2) rotate by β about the y′ axis (x′-y′-z′ represents the reference frame after the first rotation γ about the z axis). Finally, (3) rotate by α about the x″ axis (x″-y″-z″ represents the reference frame after the second rotation β about the y′ axis). The resulting reference frames after (1) and (2) are also called intermediate frames, while the resulting frame after (3) coincides with the body frame {b}. Note that rotation matrices can be multiplied together when all rotation axes are defined in the same reference frame. For the intrinsic rotations, the axes of the intermediate frames expressed in the fixed reference frame {s} are shown in Equation (3-4).

$$
\begin{aligned}
&{}^{s}\hat{\mathbf{y}}' = {}^{s}\mathbf{R}_{\hat{z}}(\gamma)\,{}^{s}\hat{\mathbf{y}}_{s}, \qquad {}^{s}\hat{\mathbf{x}}'' = {}^{s}\mathbf{R}_{\hat{y}'}(\beta)\,{}^{s}\hat{\mathbf{x}}' = {}^{s}\mathbf{R}_{\hat{y}'}(\beta)\,{}^{s}\mathbf{R}_{\hat{z}}(\gamma)\,{}^{s}\hat{\mathbf{x}}_{s}, \\
&{}^{s}\hat{\mathbf{y}}_{s} = \begin{bmatrix} 0 & 1 & 0 \end{bmatrix}^{T}, \qquad {}^{s}\hat{\mathbf{x}}_{s} = \begin{bmatrix} 1 & 0 & 0 \end{bmatrix}^{T}
\end{aligned}
\tag{3-4}
$$

where ${}^{s}\hat{\mathbf{y}}'$ and ${}^{s}\hat{\mathbf{x}}''$ denote the unit vector of the intermediate reference frame defined in the global reference system {s}, ${}^{s}\mathbf{R}_{\hat{y}'}(\beta)$ denotes the rotation matrix defined in the reference frame {s} corresponding to the rotation β about the axis ${}^{s}\hat{\mathbf{y}}'$, and similarly for the rotation matrix ${}^{s}\mathbf{R}_{\hat{x}''}$ in Equation (3-5) It can be shown that the intrinsic rotation sequence yaw-pitch-roll results in the same rotation matrix as the extrinsic rotations applied in the reverse order with the same rotation angles $(\alpha,\ \beta,\ \gamma)$. In other words, the intrinsic yaw-pitch-roll rotations γ, β, α about axes

z, y', x'', respectively, lead to the same rotation matrix as the extrinsic roll-pitch-yaw rotations $(\alpha,\ \beta,\ \gamma)$ about axes x, y, z, respectively, i.e.,

$$\begin{aligned} {}^{\mathrm{s}}\mathbf{R}_{\mathrm{b}} &= {}^{\mathrm{s}}\mathbf{R}_{\hat{x}''}(\alpha)\,{}^{\mathrm{s}}\mathbf{R}_{\hat{y}'}(\beta)\,{}^{\mathrm{s}}\mathbf{R}_{\hat{z}}(\gamma) = \left({}^{\mathrm{s}}\mathbf{R}_{\hat{z}}\,{}^{\mathrm{s}}\mathbf{R}_{\hat{y}}\,{}^{\mathrm{s}}\mathbf{R}_{\hat{x}}\,{}^{\mathrm{s}}\mathbf{R}_{\hat{y}}^{-1}\,{}^{\mathrm{s}}\mathbf{R}_{\hat{z}}^{-1}\right)\left({}^{\mathrm{s}}\mathbf{R}_{\hat{z}}\,{}^{\mathrm{s}}\mathbf{R}_{\hat{y}}\,{}^{\mathrm{s}}\mathbf{R}_{\hat{z}}^{-1}\right){}^{\mathrm{s}}\mathbf{R}_{\hat{z}} \\ &= {}^{\mathrm{s}}\mathbf{R}_{\hat{z}}(\gamma)\,{}^{\mathrm{s}}\mathbf{R}_{\hat{y}}(\beta)\,{}^{\mathrm{s}}\mathbf{R}_{\hat{x}}(\alpha) \end{aligned} \tag{3-5}$$

where $\mathbf{R}$ is a general 3D rotation or orientation matrix, and ${}^{\mathrm{s}}\mathbf{R}_{\mathrm{b}}$ denotes the orientation of the reference frame {b} relative to the reference frame {s} in the robotics literature. Now, the time derivative of the rotation matrix (i.e., time derivative of the nine components of the matrix) can be expressed in terms of the time derivatives of the Euler angles as

$$\frac{d}{dt}\,{}^{\mathrm{s}}\mathbf{R}_{\mathrm{b}} = \frac{\partial\,{}^{\mathrm{s}}\mathbf{R}_{\hat{z}}}{\partial\gamma}\,{}^{\mathrm{s}}\mathbf{R}_{\hat{y}}\,{}^{\mathrm{s}}\mathbf{R}_{\hat{x}}\,\dot{\gamma} \;+\; {}^{\mathrm{s}}\mathbf{R}_{\hat{z}}\,\frac{\partial\,{}^{\mathrm{s}}\mathbf{R}_{\hat{y}}}{\partial\beta}\,\mathbf{R}_{\hat{x}}\,\dot{\beta} \;+ {}^{\mathrm{s}}\mathbf{R}_{\hat{z}}\,{}^{\mathrm{s}}\mathbf{R}_{\hat{y}}\,\frac{\partial\,{}^{\mathrm{s}}\mathbf{R}_{\hat{x}}}{\partial\alpha}\,\dot{\alpha} \tag{3-6}$$

3.2.2 Fixed/Body Frame Angular Velocity and Euler Angle Rates

By definition, the rotation matrix can be written as a column concatenation of the unit vectors of the body frame defined in the fixed frame, ${}^{\mathrm{s}}\hat{\mathbf{x}}_{\mathrm{b}}$, ${}^{\mathrm{s}}\hat{\mathbf{y}}_{\mathrm{b}}$, and ${}^{\mathrm{s}}\hat{\mathbf{z}}_{\mathrm{b}}$, i.e., ${}^{\mathrm{s}}\mathbf{R}_{\mathrm{b}} = \left[\ {}^{\mathrm{s}}\hat{\mathbf{x}}_{\mathrm{b}}\quad {}^{\mathrm{s}}\hat{\mathbf{y}}_{\mathrm{b}}\quad {}^{\mathrm{s}}\hat{\mathbf{z}}_{\mathrm{b}}\ \right]$. The time derivative of an arbitrary vector is contributed by the rate of change of both its length and direction. Since the length of unit vectors remains constant over time, the time derivative of a unit vector is equivalent to the changing rate of its direction, which is perpendicular to the unit vector itself. The relationship between a unit vector and its time derivative can be expressed as ${}^{\mathrm{s}}\dot{\hat{\mathbf{a}}} = {}^{\mathrm{s}}\boldsymbol{\omega}\times{}^{\mathrm{s}}\hat{\mathbf{a}}$, where ${}^{\mathrm{s}}\boldsymbol{\omega}$ represents the angular velocity expressed in the fixed frame. Additionally, this equation illustrates the property that the unit vector is perpendicular to its time derivative, i.e., ${}^{\mathrm{s}}\hat{\mathbf{a}} \perp {}^{\mathrm{s}}\dot{\hat{\mathbf{a}}}$. Then, the time derivative of the rotation matrix can be written as

$$\frac{d}{dt}\,{}^{\mathrm{s}}\mathbf{R}_{\mathrm{b}} = {}^{\mathrm{s}}\dot{\mathbf{R}}_{\mathrm{b}} = \left[\ {}^{\mathrm{s}}\dot{\hat{\mathbf{x}}}_{\mathrm{b}}\quad {}^{\mathrm{s}}\dot{\hat{\mathbf{y}}}_{\mathrm{b}}\quad {}^{\mathrm{s}}\dot{\hat{\mathbf{z}}}_{\mathrm{b}}\ \right] = \left[\ {}^{\mathrm{s}}\boldsymbol{\omega}\times{}^{\mathrm{s}}\hat{\mathbf{x}}_{\mathrm{b}}\quad {}^{\mathrm{s}}\boldsymbol{\omega}\times{}^{\mathrm{s}}\hat{\mathbf{y}}_{\mathrm{b}}\quad {}^{\mathrm{s}}\boldsymbol{\omega}\times{}^{\mathrm{s}}\hat{\mathbf{z}}_{\mathrm{b}}\ \right] = \left[\ {}^{\mathrm{s}}\boldsymbol{\omega}\right]_{\times}\,{}^{\mathrm{s}}\mathbf{R}_{\mathrm{b}} \tag{3-7}$$

where $[\,\cdot\,]_{\times}$ denotes the skew-symmetric matrix operator. The skew-symmetric matrix operator is useful in the matrix form for calculating the cross product of two vectors. The skew-symmetric matrix operator is defined as

$$[\mathbf{x}]_{\times} = \begin{bmatrix} 0 & -x_3 & x_2 \\ x_3 & 0 & -x_1 \\ -x_2 & x_1 & 0 \end{bmatrix},\quad \mathbf{x} = \begin{bmatrix} x_1 \\ x_2 \\ x_3 \end{bmatrix},\quad \mathbf{y} = \begin{bmatrix} y_1 \\ y_2 \\ y_3 \end{bmatrix},\quad [\mathbf{x}]_{\times}\,\mathbf{y} = \mathbf{x}\times\mathbf{y} \tag{3-8}$$

The right-hand side (RHS) of Equation (3-7) can be rewritten as follows by: (1) recognizing the relationship ${}^{\mathrm{s}}\boldsymbol{\omega} = {}^{\mathrm{s}}\mathbf{R}_{\mathrm{b}}\,{}^{\mathrm{b}}\boldsymbol{\omega}$ between the angular velocity vectors defined in the fixed and body frames (${}^{\mathrm{s}}\boldsymbol{\omega}$ and ${}^{\mathrm{b}}\boldsymbol{\omega}$, respectively), and (2) using the rotational invariance property of the vector cross product, i.e., $\mathbf{Rx}\times\mathbf{Ry}=\mathbf{R}(\mathbf{x}\times\mathbf{y})$, which can be expressed in matrix form as $[\mathbf{Rx}]_\times\mathbf{Ry}=\mathbf{R}[\mathbf{x}]_\times\mathbf{y}$ implying that $[\mathbf{Rx}]_\times\mathbf{R}=\mathbf{R}[\mathbf{x}]_\times$ since **y** is an arbitrary nonzero vector.

$$\left[{}^{\mathrm{s}}\boldsymbol{\omega}\right]_\times {}^{\mathrm{s}}\mathbf{R}_{\mathrm{b}}=\left[{}^{\mathrm{s}}\mathbf{R}_{\mathrm{b}}{}^{\mathrm{b}}\boldsymbol{\omega}\right]_\times {}^{\mathrm{s}}\mathbf{R}_{\mathrm{b}}={}^{\mathrm{s}}\mathbf{R}_{\mathrm{b}}\left[{}^{\mathrm{b}}\boldsymbol{\omega}\right]_\times \tag{3-9}$$

The geometrical meaning of the rotational invariance of the vector cross product is that the operation of the cross product and rotation can be interchanged. In other words, performing the rotation first or performing the cross product first yields the same results. By using Equations (3-6) , (3-7), and (3-9), the Jacobian matrix between the angular velocity vector and the time derivatives of the Euler angles, which are also called Euler angle rates, can be obtained as

$${}^{\mathrm{s}}\boldsymbol{\omega} = {}^{\mathrm{s}}\mathbf{J}_{\mathrm{E}}{}^{\mathrm{E}}\boldsymbol{\omega}=\begin{bmatrix}\cos\beta\cdot\cos\gamma & -\sin\gamma & 0\\ \cos\beta\cdot\sin\gamma & \cos\gamma & 0\\ -\sin\beta & 0 & 1\end{bmatrix}\begin{bmatrix}\dot{\alpha}\\ \dot{\beta}\\ \dot{\gamma}\end{bmatrix} \tag{3-10}$$

$${}^{\mathrm{b}}\boldsymbol{\omega} = {}^{\mathrm{b}}\mathbf{J}_{\mathrm{E}}{}^{\mathrm{E}}\boldsymbol{\omega}=\mathbf{R}^{-1}\cdot{}^{\mathrm{s}}\mathbf{J}_{\mathrm{E}}{}^{\mathrm{E}}\boldsymbol{\omega}=\begin{bmatrix}1 & 0 & -\sin\beta\\ 0 & \cos\alpha & \cos\beta\cdot\sin\alpha\\ 0 & -\sin\alpha & \cos\beta\cdot\cos\alpha\end{bmatrix}\begin{bmatrix}\dot{\alpha}\\ \dot{\beta}\\ \dot{\gamma}\end{bmatrix} \tag{3-11}$$

where ${}^{\mathrm{E}}\boldsymbol{\omega}=\begin{bmatrix}\dot{\alpha} & \dot{\beta} & \dot{\gamma}\end{bmatrix}^T$, and ${}^{\mathrm{s}}\mathbf{J}_{\mathrm{E}}$ and ${}^{\mathrm{b}}\mathbf{J}_{\mathrm{E}}$ are the 3×3 Jacobian matrices between ${}^{\mathrm{s}}\boldsymbol{\omega}$, ${}^{\mathrm{b}}\boldsymbol{\omega}$ and ${}^{\mathrm{E}}\boldsymbol{\omega}$, respectively.

3.3 KINEMATICS OF THE RIGID PLATEN

The (translational and rotational) velocity kinematics of different particles on the platen is derived from the rigid platen position and orientation using basic geometry and then it is shown that the results are identical to those obtained using the rigid body transformation of the twist (defined below) from the frame $\{\mathrm{c}\}$ to frame $\{\mathrm{p}_i'\}$ as commonly done in the robotic literature. In this study, position vectors are written in the form of a bold letter **r**, with initial and terminal points in the right superscript, and the left superscript indicating the frame in which the vector components are defined. A ″0″ placed in the right subscript indicates that the position vector is defined when the platen is in its control zero-position, otherwise in the absence of a right subscript, the platen is in a displaced configuration.

For platen kinematics, the position of particle P_i' on the platen is the sum of two position vectors: (1) the platen translation vector ${}^{\mathrm{s}}\mathbf{r}^{\mathrm{OC}}$, and (2) the vector ${}^{\mathrm{s}}\mathbf{r}^{\mathrm{CP}_i'}={}^{\mathrm{s}}\mathbf{R}_{\mathrm{b}}\cdot{}^{\mathrm{s}}\mathbf{r}_0^{\mathrm{CP}_i'}$ which contains the information about the platen orientation:

$$ {}^{s}\mathbf{r}^{OP_i'} = {}^{s}\mathbf{r}^{OC} + {}^{s}\mathbf{r}^{CP_i'} = {}^{s}\mathbf{r}^{OC} + {}^{s}\mathbf{R}_{b} \cdot {}^{s}\mathbf{r}_{0}^{CP_i'} = {}^{s}\mathbf{r}^{OC} + {}^{s}\mathbf{R}_{b} \cdot {}^{s}\mathbf{r}_{0}^{OP_i'} \tag{3-12} $$

where ${}^{s}\mathbf{R}_{b}$ is the orientation matrix of the platen, and note that particle C (the platen surface center) coincides with fixed point O when the platen is in its control zero-position. Taking the time derivative on both sides of Equation (3-12) provides the relation between the velocity of particle P_i' and the velocity of particle C as

$$ {}^{s}\dot{\mathbf{r}}^{OP'} = {}^{s}\dot{\mathbf{r}}^{OC} + \left[{}^{s}\boldsymbol{\omega}\right]_{\times} {}^{s}\mathbf{R}_{b}\,{}^{s}\mathbf{r}_{0}^{OP_i'} = {}^{s}\dot{\mathbf{r}}^{OC} - \left[{}^{s}\mathbf{R}_{b}\,{}^{s}\mathbf{r}_{0}^{OP_i'}\right]_{\times} {}^{s}\boldsymbol{\omega} = \begin{bmatrix} -\left[{}^{s}\mathbf{R}_{b}\,{}^{s}\mathbf{r}_{0}^{OP_i'}\right]_{\times} & \mathbf{I}_{3} \end{bmatrix} \begin{bmatrix} {}^{s}\boldsymbol{\omega} \\ {}^{s}\dot{\mathbf{r}}^{OC} \end{bmatrix} \tag{3-13} $$

Given that: (1) the frames {s}, {c}, and $\{p_i'\}$ have the same orientation (see Table 3.1 and Figure 3.1), which implies that the angular velocities of the platen defined in these frames, ${}^{s}\boldsymbol{\omega} = {}^{c}\boldsymbol{\omega} = {}^{p_i'}\boldsymbol{\omega}$, are identical, (2) the platen linear translational velocity $\mathbf{v}^{C}$ is defined as the velocity of particle C , i.e., ${}^{c}\mathbf{v}^{C} = {}^{s}\mathbf{v}^{C} = {}^{s}\dot{\mathbf{r}}^{OC}$, and (3) the particle translational velocity $\mathbf{v}^{P_i'}$ has the same property as (2), i.e., ${}^{p_i'}\mathbf{v}^{P_i'} = {}^{s}\mathbf{v}^{P_i'} = {}^{s}\dot{\mathbf{r}}^{OP_i'}$, and using Equation (3-13), ${}^{p_i'}\mathbf{V} = \begin{bmatrix} \left({}^{p_i'}\boldsymbol{\omega}\right)^{T} & \left({}^{p_i'}\mathbf{v}^{P_i'}\right)^{T} \end{bmatrix}^{T}$ can be expressed as

$$ \begin{aligned} {}^{p_i'}\mathbf{V} &= \begin{bmatrix} {}^{p_i'}\boldsymbol{\omega} \\ {}^{p_i'}\mathbf{v}^{P_i'} \end{bmatrix} = \begin{bmatrix} {}^{s}\boldsymbol{\omega} \\ {}^{s}\dot{\mathbf{r}}^{OP_i'} \end{bmatrix} \\ &= \begin{bmatrix} \mathbf{I}_{3} & \mathbf{0} \\ -\left[{}^{s}\mathbf{R}_{b}\,{}^{s}\mathbf{r}_{0}^{OP_i'}\right]_{\times} & \mathbf{I}_{3} \end{bmatrix} \begin{bmatrix} {}^{s}\boldsymbol{\omega} \\ {}^{s}\dot{\mathbf{r}}^{OC} \end{bmatrix} = \begin{bmatrix} \mathbf{I}_{3} & \mathbf{0} \\ -\left[{}^{s}\mathbf{R}_{b}\,{}^{s}\mathbf{r}_{0}^{OP_i'}\right]_{\times} & \mathbf{I}_{3} \end{bmatrix} \begin{bmatrix} {}^{c}\boldsymbol{\omega} \\ {}^{c}\mathbf{v}^{C} \end{bmatrix} = {}^{p_i'}\mathbf{J}_{c}\,{}^{c}\mathbf{V} \end{aligned} \tag{3-14} $$

where ${}^{c}\mathbf{V}$ and ${}^{p_i'}\mathbf{V}$ are six-component vectors which are a concatenation of the angular velocity of the body and linear velocity of the particle at which the origin of the frame ({c} or $\{p_i'\}$) in the left superscript is located, with the components of the angular and linear velocities defined in frame {c} and $\{p_i'\}$, respectively.

The six-component vector $\mathbf{V}$ is referred to as twist in the robotics literature [Lynch and Park 2017]; it is a very convenient quantity to analyze the kinematics and dynamics of rigid bodies in both translational and rotational directions jointly. The two twists ${}^{c}\mathbf{V}$ and ${}^{p_i'}\mathbf{V}$ represent the same rigid body motion of the platen but measure the velocity of two different particles on the platen, and Equation (3-14) shows that they are related by the Jacobian matrix ${}^{p_i'}\mathbf{J}_{c}$, which depends on the orientation of the platen (i.e., depends on ${}^{s}\mathbf{R}_{b}$). A more general form of a Jacobian matrix that relates the twists of the same rigid body motion defined in different frames {f} and {g} is given below [Lynch and Park 2017]:

$$ {}^{\mathrm{f}}\mathbf{V} = \begin{bmatrix} {}^{\mathrm{f}}\boldsymbol{\omega} \\ {}^{\mathrm{f}}\mathbf{v}^{\mathrm{F}} \end{bmatrix} = \begin{bmatrix} {}^{\mathrm{f}}\mathbf{R}_{\mathrm{g}} & \mathbf{0} \\ \left[{}^{\mathrm{f}}\mathbf{r}^{\mathrm{FG}}\right]_{\times} {}^{\mathrm{f}}\mathbf{R}_{\mathrm{g}} & {}^{\mathrm{f}}\mathbf{R}_{\mathrm{g}} \end{bmatrix} \begin{bmatrix} {}^{\mathrm{g}}\boldsymbol{\omega} \\ {}^{\mathrm{g}}\mathbf{v}^{\mathrm{G}} \end{bmatrix} = {}^{\mathrm{f}}\mathbf{J}_{\mathrm{g}}\,{}^{\mathrm{g}}\mathbf{V} \qquad (3\text{-}15) $$

where ${}^{\mathrm{f}}\mathbf{V}$ and ${}^{\mathrm{g}}\mathbf{V}$ are the same rigid body motion defined in two arbitrary reference frames {f} and {g} with their origins located at F and G, and with ${}^{\mathrm{f}}\mathbf{R}_{\mathrm{g}}$ and ${}^{\mathrm{f}}\mathbf{r}^{\mathrm{FG}}$ providing the relation between frame {f} and frame {g}. Switching the relation between ${}^{\mathrm{f}}\mathbf{V}$ and ${}^{\mathrm{g}}\mathbf{V}$ in Equation (3-15) yields

$$ {}^{g}\mathbf{V} = {}^{g}\mathbf{J}_{\mathrm{f}}\,{}^{\mathrm{f}}\mathbf{V} \quad \text{where} \quad {}^{\mathrm{g}}\mathbf{J}_{\mathrm{f}} = \left({}^{\mathrm{f}}\mathbf{J}_{\mathrm{g}}\right)^{-1} \qquad (3\text{-}16) $$

Note that the rigid body transformation in Equation (3-15) is valid only when the twists are referring to the same rigid body motion. Therefore, it can be concluded from Table 3.1 that the twists of the shake table rigid platen defined in frames {c}, {b}, and $\{\mathrm{p}'_i\}$ follow the rigid body transformation given in Equation (3-15).

As a special case of Equation (3-15), if we choose {f} = $\{\mathrm{p}'_i\}$ and {g} = {c}, Equation (3-15) reduces to Equation (3-17) after recognizing that: (1) ${}^{\mathrm{p}'_i}\mathbf{R}_{\mathrm{c}} = \mathbf{I}_3$, and (2) ${}^{\mathrm{p}'_i}\mathbf{r}^{\mathrm{P}'_i\mathrm{C}} = {}^{\mathrm{s}}\mathbf{r}^{\mathrm{P}'_i\mathrm{C}} = -{}^{\mathrm{s}}\mathbf{r}^{\mathrm{CP}'_i}$ since the orientations of frames {s}, {c}, $\{\mathrm{p}'_i\}$ coincide. Then Equation (3-17) gives the same Jacobian matrix as Equation (3-14) since ${}^{\mathrm{s}}\mathbf{r}^{\mathrm{CP}'_i} = {}^{\mathrm{s}}\mathbf{R}_{\mathrm{b}} \cdot {}^{\mathrm{s}}\mathbf{r}_0^{\mathrm{CP}'_i} = {}^{\mathrm{s}}\mathbf{R}_{\mathrm{b}} \cdot {}^{\mathrm{s}}\mathbf{r}_0^{\mathrm{OP}'_i}$:

$$ {}^{\mathrm{p}'_i}\mathbf{V} = \begin{bmatrix} \mathbf{I}_3 & \mathbf{0} \\ -\left[{}^{\mathrm{s}}\mathbf{r}^{\mathrm{CP}'_i}\right]_{\times} & \mathbf{I}_3 \end{bmatrix} \begin{bmatrix} {}^{\mathrm{c}}\boldsymbol{\omega} \\ {}^{\mathrm{c}}\mathbf{v}^{\mathrm{C}} \end{bmatrix} = {}^{\mathrm{p}'_i}\mathbf{J}_{\mathrm{c}}\,{}^{\mathrm{c}}\mathbf{V} \qquad (3\text{-}17) $$

By using Equation (3-15) and the rotational invariance of the vector cross product used to derive Equation (3-9), the Jacobian matrix to transform the twist from frame {b} to frame {c} is given by

$$ {}^{\mathrm{c}}\mathbf{J}_{\mathrm{b}} = \begin{bmatrix} {}^{\mathrm{s}}\mathbf{R}_{\mathrm{b}} & \mathbf{0} \\ \left[{}^{\mathrm{s}}\mathbf{r}^{\mathrm{CB}}\right]_{\times} {}^{\mathrm{s}}\mathbf{R}_{\mathrm{b}} & {}^{\mathrm{s}}\mathbf{R}_{\mathrm{b}} \end{bmatrix} = \begin{bmatrix} {}^{\mathrm{s}}\mathbf{R}_{\mathrm{b}} & \mathbf{0} \\ \left[{}^{\mathrm{s}}\mathbf{R}_{\mathrm{b}}\,{}^{\mathrm{s}}\mathbf{r}_0^{\mathrm{CB}}\right]_{\times} {}^{\mathrm{s}}\mathbf{R}_{\mathrm{b}} & {}^{\mathrm{s}}\mathbf{R}_{\mathrm{b}} \end{bmatrix} = \begin{bmatrix} {}^{\mathrm{s}}\mathbf{R}_{\mathrm{b}} & \mathbf{0} \\ {}^{\mathrm{s}}\mathbf{R}_{\mathrm{b}}\left[{}^{\mathrm{s}}\mathbf{r}_0^{\mathrm{CB}}\right]_{\times} & {}^{\mathrm{s}}\mathbf{R}_{\mathrm{b}} \end{bmatrix} \qquad (3\text{-}18) $$

3.4 KINEMATICS OF COMPONENTS

For all components (including the horizontal actuators, vertical actuators, and hold-down struts, $i = 1, 2, 3, \ldots, 13$), the vectors ${}^{\mathrm{s}}\mathbf{r}_0^{\mathrm{OP}_i}$ and ${}^{\mathrm{s}}\mathbf{r}_0^{\mathrm{OA}_i}$ define the position of the platen connection point and base connection point, respectively, of the i^{th} component when the platen is in its control zero-position, and ${}^{\mathrm{s}}\mathbf{r}^{\mathrm{OP}_i}$ defines the position of the platen connection point when the platen is in its displaced configuration. By definition of a position vector and given that the base connection point is fixed, the i^{th} actuator vector pointing from the base connection point to the platen connection point can be written as

$$ {}^{\mathrm{s}}\mathbf{r}^{\mathrm{A}_i\mathrm{P}_i} = {}^{\mathrm{s}}\mathbf{r}^{\mathrm{OP}_i} - {}^{\mathrm{s}}\mathbf{r}^{\mathrm{OA}_i} = {}^{\mathrm{s}}\mathbf{r}^{\mathrm{OP}_i} - {}^{\mathrm{s}}\mathbf{r}_0^{\mathrm{OA}_i} \tag{3-19} $$

The actuator vector can also be expressed as the total length of the actuator L_i (defined as the distance between the platen and base connection points of the i^{th} actuator) multiplied by the unit vector ${}^{\mathrm{s}}\hat{\mathbf{r}}^{\mathrm{A}_i\mathrm{P}_i}$ along the actuator in its displaced configuration (called the unit or normalized actuator vector):

$$ {}^{\mathrm{s}}\mathbf{r}^{\mathrm{A}_i\mathrm{P}_i} = L_i\ {}^{\mathrm{s}}\hat{\mathbf{r}}^{\mathrm{A}_i\mathrm{P}_i} \ \Rightarrow\ L_i = \left({}^{\mathrm{s}}\hat{\mathbf{r}}^{\mathrm{A}_i\mathrm{P}_i}\right)^T {}^{\mathrm{s}}\mathbf{r}^{\mathrm{A}_i\mathrm{P}_i} \tag{3-20} $$

3.4.1 Kinematics of the Linear Actuators

The kinematic constraint between the platen and the linear actuators (i = 1, 2, 3, 4 and 11, 12, 13) can be described as the connection between particle P_i of the i^{th} linear actuator and particle P_i' of the platen at the center of the swivel head of the actuator (i.e., particles P_i and P_i' coincide), and A_i denotes the center of the base swivel of the actuator, which is fixed to the reaction mass (see Figure 3.1). Therefore, the actuator vector of the i^{th} linear actuator can be obtained from the platen configuration, since ${}^{\mathrm{s}}\mathbf{r}^{\mathrm{OP}_i} = {}^{\mathrm{s}}\mathbf{r}^{\mathrm{OP}_i'}$, and substituting Equation (3-12) into Equation (3-19) as

$$ {}^{\mathrm{s}}\mathbf{r}^{\mathrm{A}_i\mathrm{P}_i} = {}^{\mathrm{s}}\mathbf{r}^{\mathrm{OC}} + {}^{\mathrm{s}}\mathbf{R}_{\mathrm{b}} \cdot {}^{\mathrm{s}}\mathbf{r}_0^{\mathrm{OP}_i} - {}^{\mathrm{s}}\mathbf{r}_0^{\mathrm{OA}_i} \tag{3-21} $$

In addition, the actuator velocity (velocity of the piston relative to the cylinder for a horizontal actuator or velocity of the cylinder relative to the piston rod for a hold-down strut) is the projection of the velocity of the swivel head (attached to the platen) of the actuator onto the normalized actuator vector, and can be expressed as, using Equations (3-20) and (3-14),

$$ \begin{aligned} \dot{L}_i &= \left({}^{\mathrm{s}}\hat{\mathbf{r}}^{\mathrm{A}_i\mathrm{P}_i}\right)^T {}^{\mathrm{s}}\dot{\mathbf{r}}^{\mathrm{A}_i\mathrm{P}_i} + \underbrace{\left({}^{\mathrm{s}}\dot{\hat{\mathbf{r}}}^{\mathrm{A}_i\mathrm{P}_i}\right)^T {}^{\mathrm{s}}\mathbf{r}^{\mathrm{A}_i\mathrm{P}_i}}_{0} = \left({}^{\mathrm{s}}\hat{\mathbf{r}}^{\mathrm{A}_i\mathrm{P}_i}\right)^T {}^{\mathrm{p}_i'}\mathbf{v}^{\mathrm{P}_i'} \\ &= \left({}^{\mathrm{s}}\hat{\mathbf{r}}^{\mathrm{A}_i\mathrm{P}_i}\right)^T \begin{bmatrix} -\left[{}^{\mathrm{s}}\mathbf{R}_{\mathrm{b}}\,{}^{\mathrm{s}}\mathbf{r}_0^{\mathrm{OP}_i'}\right]_{\times} & \mathbf{I}_3 \end{bmatrix} {}^{\mathrm{c}}\mathbf{V} = {}^{L_i}\mathbf{J}_{\mathrm{c}}\,{}^{\mathrm{c}}\mathbf{V} \end{aligned} \tag{3-22} $$

since it can be shown that $\hat{\mathbf{r}}^{\mathrm{A}_i\mathrm{P}_i} \perp \dot{\hat{\mathbf{r}}}^{\mathrm{A}_i\mathrm{P}_i}$ by applying the property stated below Equation (3-7), and ${}^{L_i}\mathbf{J}_{\mathrm{c}}$ is a 1×6 matrix.

3.4.2 Kinematics of the Vertical Actuators

In order to allow the platen to move in the roll and pitch directions, the vertical actuators were designed such that the actuator piston can tilt up to 2 degrees within the actuator cylinder. Two seals as shown on the left part of Figure **3.2**(a) ensure that no pressurized fluid leaks between the actuator piston and the cylinder: (1) a piston seal is placed between the base of the piston and the cylinder, and (2) a face seal is partially embedded on top of the piston and provides a sliding surface with an oil film between the piston face and the glider plate bolted to the bottom of the platen. The axes of the piston and the cylinder do not coincide, which complicates the kinematics; therefore, the actual kinematics of the piston and pressure-balanced bearing plate (called surface plate herein) is modified to simplify its modeling as shown on the right part of Figure **3.2**(a), but without implied approximation of the platen kinematics (i.e., equivalent but simpler representation of the vertical actuator kinematics). In this equivalent representation, the piston is separated in two parts: (1) the actuator (piston) rod assumed to always move along the direction of the vertical actuator cylinder without rotating, and (2) the piston surface plate assumed to be connected to the piston rod through a universal joint (a joint that has two independent rotational degrees of freedom) with the constraint that the rotation of the surface plate about its normal vector is not allowed. Under this assumption, the line connecting the center of the bottom of the actuator cylinder to the center of the top surface plate (which is assumed to be massless and of zero thickness) coincides with the vertical actuator axis (or actuator vector).

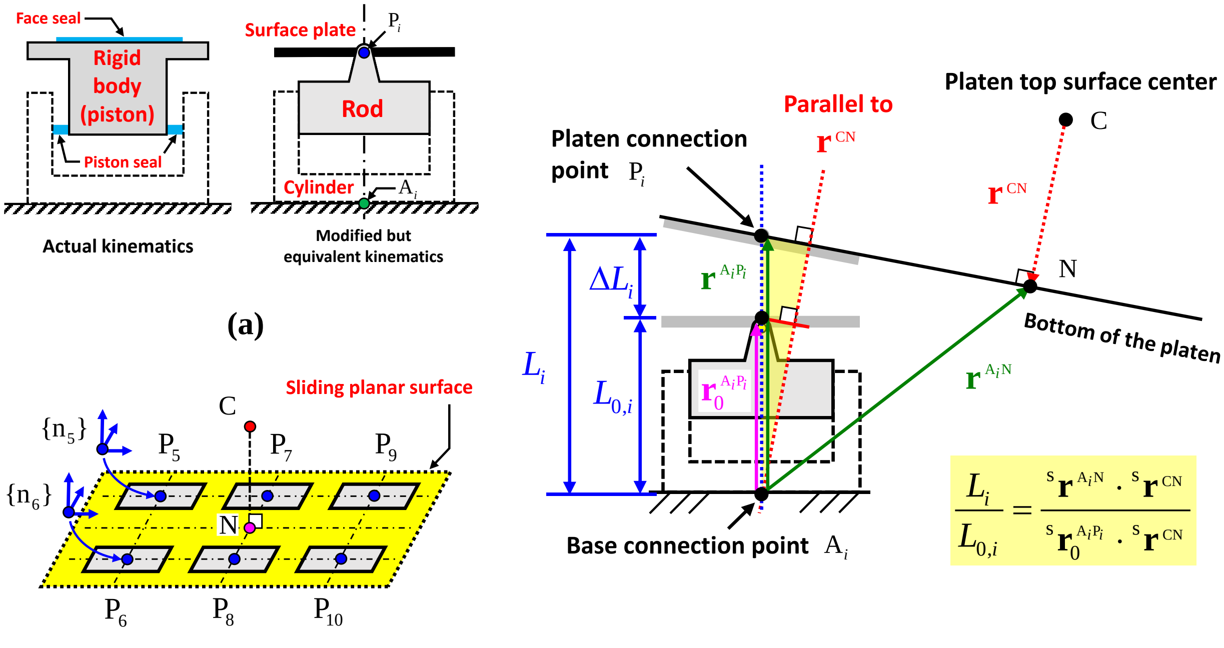

(a)

(b)

(c)

Figure 3.2 **Geometry of the vertical actuators; (a) modification of the vertical actuator kinematics to simplify its modeling, (b) particles and reference frames associated to the vertical actuator surface plates, and (c) geometry of a vertical actuator when the shake table platen is in a displaced configuration.**

Analogous to the base and front swivels of the horizontal actuators, the connection points of the i^{th} vertical actuators to the platen and the base (i.e., reaction mass) are defined as particle P_i at the center of the actuator surface plate and particle A_i at the center of the bottom of the cylinder of the actuator, respectively (see Figure **3.2**(a)). Note that due to the nature of the platen sliding on top of the vertical actuator, particle P_i' of the platen that is in contact with particle P_i of the vertical actuator surface plate at a given instant of time depends on the displaced configuration of the platen. Since the platen is sliding smoothly on the surface plates of all six vertical actuators, the particles P_i of all vertical actuators (i = 5, 6, …, 10) are coplanar and define the sliding surface (see Figure **3.2**(b)). A particle N at the bottom of the platen is defined on the sliding surface with the property that $\mathbf{r}^{\mathrm{CN}} \perp \mathbf{r}^{\mathrm{NP}_i}$ in any arbitrary platen configuration, as shown in Figure **3.2**(b).

By following the same convention as for the horizontal actuators, ${}^{\mathrm{s}}\mathbf{r}_0^{\mathrm{A}_i\mathrm{P}_i}$ is the i^{th} vertical actuator vector (defined in frame {s}) when the platen is in its control zero-position. Meanwhile, to determine the kinematics of the vertical actuators for an arbitrary platen configuration, the position vector from the base connection point A_i of a vertical actuator to the particle N on the platen is expressed from the platen configuration as

$$ {}^{\mathrm{s}}\mathbf{r}^{\mathrm{A}_i\mathrm{N}} = {}^{\mathrm{s}}\mathbf{r}^{\mathrm{OC}} + {}^{\mathrm{s}}\mathbf{r}^{\mathrm{CN}} - {}^{\mathrm{s}}\mathbf{r}_0^{\mathrm{OA}_i} = {}^{\mathrm{s}}\mathbf{r}^{\mathrm{OC}} + {}^{\mathrm{s}}\mathbf{R}_{\mathrm{b}} \cdot {}^{\mathrm{s}}\mathbf{r}_0^{\mathrm{CN}} - {}^{\mathrm{s}}\mathbf{r}_0^{\mathrm{OA}_i} \tag{3-23} $$

Define the two inner products of position vectors $f_i = {}^{\mathrm{s}}\mathbf{r}^{\mathrm{A}_i\mathrm{N}} \cdot {}^{\mathrm{s}}\mathbf{r}^{\mathrm{CN}}$ and $a_i = {}^{\mathrm{s}}\mathbf{r}_0^{\mathrm{A}_i\mathrm{P}_i} \cdot {}^{\mathrm{s}}\mathbf{r}^{\mathrm{CN}}$. Then from Figure **3.2** (c) and the properties of similar triangles, the ratio between the current and initial length (L_i and $L_{0,i}$, respectively) of the i^{th} vertical actuator can be found as

$$ L_i = \frac{f_i}{a_i} \cdot L_{0,i} \tag{3-24} $$

The direction of a vertical actuator vector does not change over time (i.e., it remains aligned with the z-axis of the {s} frame), which implies that

$$ {}^{\mathrm{s}}\mathbf{r}^{\mathrm{A}_i\mathrm{P}_i} = L_i\, {}^{\mathrm{s}}\hat{\mathbf{r}}^{\mathrm{A}_i\mathrm{P}_i} = \frac{L_i}{L_{0,i}}\, {}^{\mathrm{s}}\mathbf{r}_0^{\mathrm{A}_i\mathrm{P}_i} = \frac{f_i}{a_i}\, {}^{\mathrm{s}}\mathbf{r}_0^{\mathrm{A}_i\mathrm{P}_i} \tag{3-25} $$

Since the direction of a vertical actuator remains fixed over time, the time derivative of the actuator vector is obtained by multiplying the piston velocity with the normalized actuator vector as

$$ {}^{\mathrm{p}_i}\mathbf{v}^{\mathrm{P}_i} = {}^{\mathrm{s}}\dot{\mathbf{r}}^{\mathrm{A}_i\mathrm{P}_i} = \dot{L}_i\, {}^{\mathrm{s}}\hat{\mathbf{r}}^{\mathrm{A}_i\mathrm{P}_i} \tag{3-26} $$

The piston velocity $\dot{L}_i$ can be obtained by taking the time derivative on both sides of Equation (3-24) and express the results as a function of the platen twist as

$$ \dot{L}_i = \frac{L_{0,i}}{a_i^2}\left(\dot{f}_i\, a_i - f_i\, \dot{a}_i \right) = \frac{L_{0,i}}{a_i}\left[-\left({}^{\mathrm{s}}\mathbf{r}^{\mathrm{A}_i\mathrm{N}} + {}^{\mathrm{s}}\mathbf{r}^{\mathrm{CN}} - {}^{\mathrm{s}}\mathbf{r}^{\mathrm{A}_i\mathrm{P}_i} \right)^T \left[{}^{\mathrm{s}}\mathbf{r}^{\mathrm{CN}} \right]_\times \quad \left({}^{\mathrm{s}}\mathbf{r}^{\mathrm{CN}} \right)^T \right] {}^{\mathrm{c}}\mathbf{V} = {}^{L_i}\mathbf{J}_{\mathrm{c}}\, {}^{\mathrm{c}}\mathbf{V} \tag{3-27} $$

Appendix 1 provides the details of the derivation of Equation (3-27). For determining the friction and viscous forces between the platen and the surface plates of the vertical actuators, the velocity of particle P_i', ${}^{\mathrm{p}_i'}\mathbf{v}^{\mathrm{P}_i'}$, is needed, which can be obtained from Equation (3-17) by substituting the kinematic relation below:

$$ {}^{\mathrm{s}}\mathbf{r}^{\mathrm{CP}'_i} = {}^{\mathrm{s}}\mathbf{r}^{\mathrm{CP}_i} = {}^{\mathrm{s}}\mathbf{r}^{\mathrm{OA}_i} + {}^{\mathrm{s}}\mathbf{r}^{\mathrm{A}_i\mathrm{P}_i} - {}^{\mathrm{s}}\mathbf{r}^{\mathrm{OC}} \tag{3-28} $$

3.5 INVERSE AND FORWARD KINEMATICS OF THE LHPOST6

In robotics literature, forward kinematics refers to the process of finding the end effector (e.g., the device at the end of a robotic arm) configuration from the known joint displacements (of the robot), while inverse kinematics is the reverse process. In the case of the LHPOST6, the end effector is the platen, and the “joints” consist of the horizontal (i = 1, 2, 3, 4) and vertical actuators (i = 5, …, 10) the displacements (of the piston relative to the cylinder) of which are measured. Therefore, the inverse kinematics problem, which consists of finding the actuator lengths (or “joint” displacements) from the platen location and orientation (end effector configuration), can be solved analytically from the material presented in Sections 3.3 and 3.4. However, the forward kinematics cannot be solved analytically. In this section, the Gauss-Newton method, a modification of Newton-Raphson method, is used to solve the forward kinematics numerically as a nonlinear least-squares problem since the number of equations (10 known/measured actuator lengths) is larger than the number of parameters to be determined (i.e., the 6 DOFs characterizing the rigid platen configuration). The modification applied to the original Newton-Raphson method is to make use of the pseudoinverse of a Jacobian matrix that is non-square instead of taking its inverse, with the objective to find a solution that minimizes the norm of the error function.

The forward kinematics of the LHPOST6 is important since estimating the platen configuration from the measured actuator displacements is more feasible than measuring directly the 6-DOF configuration of the platen. The forward kinematics problem and its solution procedure are described below.

Problem: First define the vector $\mathbf{L} = \begin{bmatrix} L_1 & L_2 & \cdots & L_{10} \end{bmatrix}$ of horizontal and vertical actuator lengths, where an actuator length is defined specifically as the distance between the centers of the two end swivels of a horizontal actuator or the distance between the center of the bottom of the actuator cylinder and the center of the top surface (pressure balanced bearing) plate for a vertical actuator. Given a set of known (measured) actuator lengths $\mathbf{L}_m$, which is a 10-component vector, find the desired platen configuration i.e., $({}^{\mathrm{s}}\mathbf{r}^{\mathrm{OC}}, \alpha, \beta, \gamma)_d$, where ${}^{\mathrm{s}}\mathbf{r}^{\mathrm{OC}}$ denotes the position vector of the top center of the platen, and (α, β, γ) denote the Euler angles defining the platen orientation.

Solution procedure:

Step 1: Define the inverse kinematics function $\boldsymbol{f}_{IK}({}^{\mathrm{s}}\mathbf{r}^{\mathrm{OC}}, \alpha, \beta, \gamma)$ as the mapping from the 6-DOF platen configuration to the corresponding 10 actuator lengths ($\mathbf{L}$), and the error function $\boldsymbol{f}({}^{\mathrm{s}}\mathbf{r}^{\mathrm{OC}}, \alpha, \beta, \gamma)$ as the difference between $\boldsymbol{f}_{IK}({}^{\mathrm{s}}\mathbf{r}^{\mathrm{OC}}, \alpha, \beta, \gamma)$ and $\mathbf{L}_m$. Both the output of $\boldsymbol{f}_{IK}({}^{\mathrm{s}}\mathbf{r}^{\mathrm{OC}}, \alpha, \beta, \gamma)$ and $\boldsymbol{f}({}^{\mathrm{s}}\mathbf{r}^{\mathrm{OC}}, \alpha, \beta, \gamma)$ are 10-component vectors; therefore, a scalar function ε

is defined as the Euclidean norm of $\boldsymbol{f}({}^{\mathrm{s}}\mathbf{r}^{\mathrm{OC}}, \alpha, \beta, \gamma)$ to evaluate the magnitude of the vector error function, i.e.,

$$\boldsymbol{f}({}^{\mathrm{s}}\mathbf{r}^{\mathrm{OC}}, \alpha, \beta, \gamma) = \boldsymbol{f}_{IK}({}^{\mathrm{s}}\mathbf{r}^{\mathrm{OC}}, \alpha, \beta, \gamma) - \mathbf{L}_m = \mathbf{L} - \mathbf{L}_m; \qquad \varepsilon = \left\| \boldsymbol{f}({}^{\mathrm{s}}\mathbf{r}^{\mathrm{OC}}, \alpha, \beta, \gamma) \right\| \tag{3-29}$$

where $\boldsymbol{f}_{IK}({}^{\mathrm{s}}\mathbf{r}^{\mathrm{OC}}, \alpha, \beta, \gamma)$ can be obtained from Equations (3-20) and (3-21) for the horizontal actuators and from Equations (3-20) and (3-25) for the vertical actuators as

$$\boldsymbol{f}_{IK,i}({}^{\mathrm{s}}\mathbf{r}^{\mathrm{OC}}, \alpha, \beta, \gamma) = \begin{cases} \left\| {}^{\mathrm{s}}\mathbf{r}^{\mathrm{OC}} + {}^{\mathrm{s}}\mathbf{R}_{\mathrm{b}} \cdot {}^{\mathrm{s}}\mathbf{r}_0^{\mathrm{OP}_i} - {}^{\mathrm{s}}\mathbf{r}_0^{\mathrm{OA}_i} \right\|_2, & \text{for } i = 1-4 \\ \left\| \dfrac{\left({}^{\mathrm{s}}\mathbf{r}^{\mathrm{OC}} + {}^{\mathrm{s}}\mathbf{R}_{\mathrm{b}} \cdot {}^{\mathrm{s}}\mathbf{r}_0^{\mathrm{CN}} - {}^{\mathrm{s}}\mathbf{r}_0^{\mathrm{OA}_i} \right) \cdot \left({}^{\mathrm{s}}\mathbf{R}_{\mathrm{b}} \cdot {}^{\mathrm{s}}\mathbf{r}_0^{\mathrm{CN}} \right)}{{}^{\mathrm{s}}\mathbf{r}_0^{\mathrm{A}_i\mathrm{P}_i} \cdot \left({}^{\mathrm{s}}\mathbf{R}_{\mathrm{b}} \cdot {}^{\mathrm{s}}\mathbf{r}_0^{\mathrm{CN}} \right)} \cdot {}^{\mathrm{s}}\mathbf{r}_0^{\mathrm{A}_i\mathrm{P}_i} \right\|_2, & \text{for } i = 5-10 \end{cases} \tag{3-30}$$

Step 2: Start with an initial guess $({}^{\mathrm{s}}\mathbf{r}^{\mathrm{OC}}, \alpha, \beta, \gamma)_{j=0}$ where j is the iteration index. In this study, the converged value of $({}^{\mathrm{s}}\mathbf{r}^{\mathrm{OC}}, \alpha, \beta, \gamma)$ at the previous time step was successfully used as initial guess at the current time step.

Step 3: The Jacobian matrix of $\boldsymbol{f}({}^{\mathrm{s}}\mathbf{r}^{\mathrm{OC}}, \alpha, \beta, \gamma)$ is defined as

$$\mathbf{J}_{IK} = \frac{\partial \boldsymbol{f}({}^{\mathrm{s}}\mathbf{r}^{\mathrm{OC}}, \alpha, \beta, \gamma)}{\partial \left({}^{\mathrm{s}}\mathbf{r}^{\mathrm{OC}}, \alpha, \beta, \gamma \right)} = \frac{\partial \boldsymbol{f}_{IK}({}^{\mathrm{s}}\mathbf{r}^{\mathrm{OC}}, \alpha, \beta, \gamma)}{\partial \left({}^{\mathrm{s}}\mathbf{r}^{\mathrm{OC}}, \alpha, \beta, \gamma \right)} \tag{3-31}$$

which is a 10×6 matrix. Using the chain rule of differentiation, the velocities of the actuator pistons (along the instantaneous direction of the actuator) are related to the platen linear translational velocity and Euler angle rates by the Jacobian matrix, i.e.,

$$\frac{dL_i}{dt} = \frac{\partial L_i}{\partial {}^{\mathrm{s}}\mathbf{r}^{\mathrm{OC}}} \cdot \frac{d\,{}^{\mathrm{s}}\mathbf{r}^{\mathrm{OC}}}{dt} + \frac{\partial L_i}{\partial \left(\alpha, \beta, \gamma \right)} \cdot \frac{d\left(\alpha, \beta, \gamma \right)}{dt} = \begin{bmatrix} \dfrac{\partial L_i}{\partial {}^{\mathrm{s}}\mathbf{r}^{\mathrm{OC}}} & \dfrac{\partial L_i}{\partial \left(\alpha, \beta, \gamma \right)} \end{bmatrix} \begin{bmatrix} {}^{\mathrm{s}}\dot{\mathbf{r}}^{\mathrm{OC}} \\ {}^{\mathrm{E}}\boldsymbol{\omega} \end{bmatrix} \tag{3-32}$$

Therefore, each row of the Jacobian matrix of $\boldsymbol{f}({}^{\mathrm{s}}\mathbf{r}^{\mathrm{OC}}, \alpha, \beta, \gamma)$ is determined by substituting Equation (3-10) into Equation (3-22) for the horizontal actuators and into Equation (3-27) for the vertical actuators as

$$\dot{L}_i = \mathbf{J}_{IK,i}\begin{bmatrix} {}^{\mathrm{s}}\dot{\mathbf{r}}^{\mathrm{OC}} \\ {}^{\mathrm{E}}\boldsymbol{\omega} \end{bmatrix}$$

$$= \begin{cases} \left({}^{\mathrm{s}}\hat{\mathbf{r}}^{\mathrm{A}_i\mathrm{P}_i}\right)^T \begin{bmatrix} \mathbf{I}_3 & -\left[{}^{\mathrm{s}}\mathbf{R}_{\mathrm{b}}\,{}^{\mathrm{s}}\mathbf{r}_0^{\mathrm{OP}'_i}\right]_\times {}^{\mathrm{s}}\mathbf{J}_{\mathrm{E}} \end{bmatrix} \begin{bmatrix} {}^{\mathrm{s}}\dot{\mathbf{r}}^{\mathrm{OC}} \\ {}^{\mathrm{E}}\boldsymbol{\omega} \end{bmatrix}, & \text{for } i = 1-4 \\ \dfrac{L_{0,i}}{a_i}\begin{bmatrix} \left({}^{\mathrm{s}}\mathbf{r}^{\mathrm{CN}}\right)^T & -\left({}^{\mathrm{s}}\mathbf{r}^{\mathrm{A}_i\mathrm{N}} + {}^{\mathrm{s}}\mathbf{r}^{\mathrm{CN}} - {}^{\mathrm{s}}\mathbf{r}^{\mathrm{A}_i\mathrm{P}_i}\right)^T \left[{}^{\mathrm{s}}\mathbf{r}^{\mathrm{CN}}\right]_\times {}^{\mathrm{s}}\mathbf{J}_{\mathrm{E}} \end{bmatrix} \begin{bmatrix} {}^{\mathrm{s}}\dot{\mathbf{r}}^{\mathrm{OC}} \\ {}^{\mathrm{E}}\boldsymbol{\omega} \end{bmatrix}, & \text{for } i = 5-10 \end{cases} \tag{3-33}$$

Step 4: The next iteration for the platen configuration is obtained as

$$({}^{\mathrm{s}}\mathbf{r}^{\mathrm{OC}}, \alpha, \beta, \gamma)_{j+1} = ({}^{\mathrm{s}}\mathbf{r}^{\mathrm{OC}}, \alpha, \beta, \gamma)_j - \left(\mathbf{J}_{IK}\right)_j^{+} \boldsymbol{f}({}^{\mathrm{s}}\mathbf{r}^{\mathrm{OC}}, \alpha, \beta, \gamma)_j \tag{3-34}$$

where $\mathbf{J}_{IK}{}^{+} = \left(\mathbf{J}_{IK}{}^{T}\mathbf{J}_{IK}\right)^{-1}\mathbf{J}_{IK}{}^{T}$ is the Moore-Penrose (or pseudo) inverse of $\mathbf{J}_{IK}$ when $\mathbf{J}_{IK}$ is a tall matrix and has linearly independent columns.

Step 5: Iterate by repeating step 3 and step 4 until the error norm ε drops below a specified tolerance threshold.

APPENDIX 1: Derivation of Equation (3-27)

Step 1: From the definitions of Points C and N (the two points are both on the platen), ${}^{\mathrm s}\mathbf{r}^{\mathrm{CN}} = {}^{\mathrm s}\mathbf{R}_{\mathrm b} \cdot {}^{\mathrm s}\mathbf{r}_0^{\mathrm{CN}}$

Taking the time derivative of ${}^{\mathrm s}\mathbf{r}^{\mathrm{CN}} = {}^{\mathrm s}\mathbf{R}_{\mathrm b} \cdot {}^{\mathrm s}\mathbf{r}_0^{\mathrm{CN}}$:

${}^{\mathrm s}\dot{\mathbf{r}}^{\mathrm{CN}} = {}^{\mathrm s}\dot{\mathbf{R}}_{\mathrm b} \cdot {}^{\mathrm s}\mathbf{r}_0^{\mathrm{CN}} = \left[{}^{\mathrm s}\boldsymbol{\omega}\right]_\times \underbrace{{}^{\mathrm s}\mathbf{R}_{\mathrm b}\, {}^{\mathrm s}\mathbf{r}_0^{\mathrm{CN}}}_{{}^{\mathrm s}\mathbf{r}^{\mathrm{CN}}} = -\left[{}^{\mathrm s}\mathbf{r}^{\mathrm{CN}}\right]_\times {}^{\mathrm s}\boldsymbol{\omega}$ by using Equation (3-7) and $\mathbf{a}\times\mathbf{b} = -\,\mathbf{b}\times\mathbf{a}$.

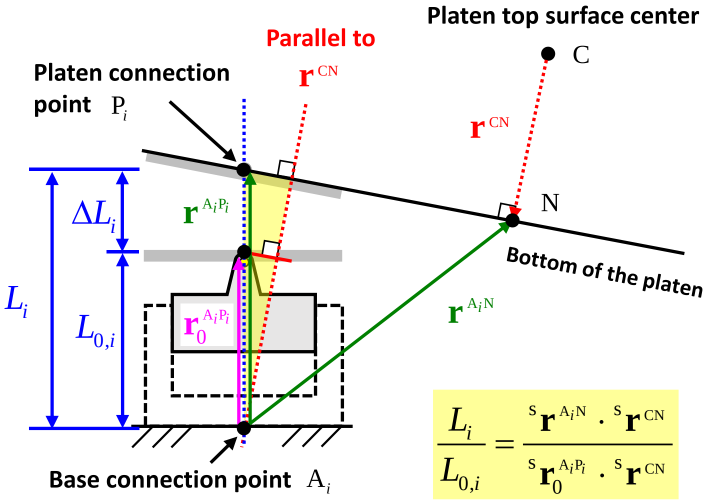

Copy of Figure **3.2**(c)

Step 2: Recalling Equation (3-23), ${}^{\mathrm s}\mathbf{r}^{\mathrm{A}_i\mathrm{N}} = {}^{\mathrm s}\mathbf{r}^{\mathrm{OC}} + {}^{\mathrm s}\mathbf{R}_{\mathrm b} \cdot {}^{\mathrm s}\mathbf{r}_0^{\mathrm{CN}} - {}^{\mathrm s}\mathbf{r}_0^{\mathrm{OA}_i}$.

Taking the time derivative of ${}^{\mathrm s}\mathbf{r}^{\mathrm{A}_i\mathrm{N}}$ and using the results in Step 1:

$${}^{\mathrm s}\dot{\mathbf{r}}^{\mathrm{A}_i\mathrm{N}} = {}^{\mathrm s}\dot{\mathbf{r}}^{\mathrm{OC}} - \left[{}^{\mathrm s}\mathbf{r}^{\mathrm{CN}}\right]_\times {}^{\mathrm s}\boldsymbol{\omega} - \underbrace{{}^{\mathrm s}\dot{\mathbf{r}}_0^{\mathrm{OA}_i}}_{0} = {}^{\mathrm s}\dot{\mathbf{r}}^{\mathrm{OC}} - \left[{}^{\mathrm s}\mathbf{r}^{\mathrm{CN}}\right]_\times {}^{\mathrm s}\boldsymbol{\omega}$$

Step 3: Taking the time derivative of the two scalars $f_i = {}^{\mathrm s}\mathbf{r}^{\mathrm{A}_i\mathrm{N}} \cdot {}^{\mathrm s}\mathbf{r}^{\mathrm{CN}}$ and $a_i = {}^{\mathrm s}\mathbf{r}_0^{\mathrm{A}_i\mathrm{P}_i} \cdot {}^{\mathrm s}\mathbf{r}^{\mathrm{CN}}$ defined above Equation (3-24) and using the results in Step 1 and Step 2:

$$\begin{aligned}\dot{f}_i &= {}^{\mathrm s}\dot{\mathbf{r}}^{\mathrm{A}_i\mathrm{N}} \cdot {}^{\mathrm s}\mathbf{r}^{\mathrm{CN}} + {}^{\mathrm s}\mathbf{r}^{\mathrm{A}_i\mathrm{N}} \cdot {}^{\mathrm s}\dot{\mathbf{r}}^{\mathrm{CN}} = \left({}^{\mathrm s}\dot{\mathbf{r}}^{\mathrm{OC}} - \left[{}^{\mathrm s}\mathbf{r}^{\mathrm{CN}}\right]_\times {}^{\mathrm s}\boldsymbol{\omega}\right) \cdot {}^{\mathrm s}\mathbf{r}^{\mathrm{CN}} + {}^{\mathrm s}\mathbf{r}^{\mathrm{A}_i\mathrm{N}} \cdot \left(-\left[{}^{\mathrm s}\mathbf{r}^{\mathrm{CN}}\right]_\times {}^{\mathrm s}\boldsymbol{\omega}\right)\\ &= {}^{\mathrm s}\mathbf{r}^{\mathrm{CN}} \cdot {}^{\mathrm s}\dot{\mathbf{r}}^{\mathrm{OC}} - \left({}^{\mathrm s}\mathbf{r}^{\mathrm{CN}} + {}^{\mathrm s}\mathbf{r}^{\mathrm{A}_i\mathrm{N}}\right) \cdot \left[{}^{\mathrm s}\mathbf{r}^{\mathrm{CN}}\right]_\times {}^{\mathrm s}\boldsymbol{\omega}\end{aligned}$$

$$\dot{a}_i = \underbrace{{}^{\mathrm s}\dot{\mathbf{r}}_0^{\mathrm{A}_i\mathrm{P}_i}}_{0} \cdot {}^{\mathrm s}\mathbf{r}^{\mathrm{CN}} + {}^{\mathrm s}\mathbf{r}_0^{\mathrm{A}_i\mathrm{P}_i} \cdot {}^{\mathrm s}\dot{\mathbf{r}}^{\mathrm{CN}} = {}^{\mathrm s}\mathbf{r}_0^{\mathrm{A}_i\mathrm{P}_i} \cdot \left(-\left[{}^{\mathrm s}\mathbf{r}^{\mathrm{CN}}\right]_\times {}^{\mathrm s}\boldsymbol{\omega}\right) = -\,{}^{\mathrm s}\mathbf{r}_0^{\mathrm{A}_i\mathrm{P}_i} \cdot \left[{}^{\mathrm s}\mathbf{r}^{\mathrm{CN}}\right]_\times {}^{\mathrm s}\boldsymbol{\omega}$$

Step 4: Substituting all the terms derived in Steps 1 – 3 into Equation (3-27), after the first equal sign:

$$\begin{aligned}\dot{L}_i &= \frac{L_{0,i}}{a_i^2}\left(\dot{f}_i\, a_i - f_i\, \dot{a}_i\right) = \frac{L_{0,i}}{a_i}\left(\dot{f}_i - \frac{f_i}{a_i}\dot{a}_i\right)\\ &= \frac{L_{0,i}}{a_i}\left({}^{\mathrm{s}}\mathbf{r}^{\mathrm{CN}}\cdot{}^{\mathrm{s}}\dot{\mathbf{r}}^{\mathrm{OC}} - \left({}^{\mathrm{s}}\mathbf{r}^{\mathrm{CN}} + {}^{\mathrm{s}}\mathbf{r}^{\mathrm{A}_i\mathrm{N}} - \frac{f_i}{a_i}\cdot{}^{\mathrm{s}}\mathbf{r}_0^{\mathrm{A}_i\mathrm{P}_i}\right)\cdot\left[{}^{\mathrm{s}}\mathbf{r}^{\mathrm{CN}}\right]_{\times}{}^{\mathrm{s}}\boldsymbol{\omega}\right)\end{aligned}$$

Recalling Equation (3-25), ${}^{\mathrm{s}}\mathbf{r}^{\mathrm{A}_i\mathrm{P}_i} = \frac{f_i}{a_i}\cdot{}^{\mathrm{s}}\mathbf{r}_0^{\mathrm{A}_i\mathrm{P}_i}$, and using the definition of the inner product of two vectors $\mathbf{a}\cdot\mathbf{b} = \mathbf{a}^T\mathbf{b}$:

$$\begin{aligned}\dot{L}_i &= \frac{L_{0,i}}{a_i^2}\left({}^{\mathrm{s}}\mathbf{r}^{\mathrm{CN}}\cdot{}^{\mathrm{s}}\dot{\mathbf{r}}^{\mathrm{OC}} - \left({}^{\mathrm{s}}\mathbf{r}^{\mathrm{CN}} + {}^{\mathrm{s}}\mathbf{r}^{\mathrm{A}_i\mathrm{N}} - {}^{\mathrm{s}}\mathbf{r}^{\mathrm{A}_i\mathrm{P}_i}\right)\cdot\left[{}^{\mathrm{s}}\mathbf{r}^{\mathrm{CN}}\right]_{\times}{}^{\mathrm{s}}\boldsymbol{\omega}\right)\\ &= \frac{L_{0,i}}{a_i}\left[-\left({}^{\mathrm{s}}\mathbf{r}^{\mathrm{CN}} + {}^{\mathrm{s}}\mathbf{r}^{\mathrm{A}_i\mathrm{N}} - {}^{\mathrm{s}}\mathbf{r}^{\mathrm{A}_i\mathrm{P}_i}\right)^T\left[{}^{\mathrm{s}}\mathbf{r}^{\mathrm{CN}}\right]_{\times} \quad \left({}^{\mathrm{s}}\mathbf{r}^{\mathrm{CN}}\right)^T\right]\begin{bmatrix}{}^{\mathrm{s}}\boldsymbol{\omega}\\ {}^{\mathrm{s}}\dot{\mathbf{r}}^{\mathrm{OC}}\end{bmatrix}\\ &= \frac{L_{0,i}}{a_i}\left[-\left({}^{\mathrm{s}}\mathbf{r}^{\mathrm{CN}} + {}^{\mathrm{s}}\mathbf{r}^{\mathrm{A}_i\mathrm{N}} - {}^{\mathrm{s}}\mathbf{r}^{\mathrm{A}_i\mathrm{P}_i}\right)^T\left[{}^{\mathrm{s}}\mathbf{r}^{\mathrm{CN}}\right]_{\times} \quad \left({}^{\mathrm{s}}\mathbf{r}^{\mathrm{CN}}\right)^T\right]{}^{\mathrm{c}}\mathbf{V}\end{aligned}$$

Step 5: The Jacobian matrix ${}^{L_i}\mathbf{J}_{\mathrm{c}}$ relates the platen twist ${}^{\mathrm{c}}\mathbf{V}$ to the piston velocity $\dot{L}_i$ as

$$\dot{L}_i = {}^{L_i}\mathbf{J}_{\mathrm{c}}\,{}^{\mathrm{c}}\mathbf{V}$$

where

$${}^{L_i}\mathbf{J}_{\mathrm{c}} = \frac{L_{0,i}}{a_i}\left[-\left({}^{\mathrm{s}}\mathbf{r}^{\mathrm{CN}} + {}^{\mathrm{s}}\mathbf{r}^{\mathrm{A}_i\mathrm{N}} - {}^{\mathrm{s}}\mathbf{r}^{\mathrm{A}_i\mathrm{P}_i}\right)^T\left[{}^{\mathrm{s}}\mathbf{r}^{\mathrm{CN}}\right]_{\times} \quad \left({}^{\mathrm{s}}\mathbf{r}^{\mathrm{CN}}\right)^T\right]$$

4 FORCES FROM COMPONENTS ACTING ON THE PLATEN AND 6-DOF RIGID BODY DYNAMICS OF THE LHPOST6

The platen of the LHPOST6 is acted upon by both active (servo-hydraulic actuators, $i = 1, 2, \ldots, 10$) and passive components (nitrogen pre-charged hold down struts, $i = 11, 12, 13$) as shown in Table 2.1, and the forces that are generated from the hydraulic and nitrogen pressure inside the various components are called component forces. The friction and viscous forces developing at the interface between the moving parts of the various components (including the platen) of the shake table system are referred to as dissipative forces. The component forces and dissipative forces are acting on the platen at their connection points, and the force and moment resultants cause the translational and rotational motion of the platen. In this chapter, the component forces will be introduced first, including how the hydraulic forces are related to the servovalve spool displacements and the traction forces from the hold-down struts are governed by the ideal gas law. Then, the dissipative forces, including sliding friction, seal friction, and viscous damping forces, are considered in the formulation of the numerical model of the LHPOST6. At the end of this chapter, the rigid body dynamics of the platen is formulated to obtain the platen motion from the total forces and moments acting on the platen and expressed in the body frame. A simplified method consisting of lumping the actuator and hold-down strut moving masses as point masses attached to the platen at the connection points is also presented in this chapter.

4.1 HYDRAULIC FORCES

Each hydraulic actuator of the LHPOST6 consists of a cylinder, piston rod assembly, and one 3-way (per vertical actuator) or two 4-way (per horizontal actuator) servovalve(s). The horizontal actuators are double-acting, while the vertical actuators are single-acting (see Figure 4.1). The horizontal actuators have a double-acting piston (with two different effective piston areas in the ″extend″ and ″retract″ directions) with a port on each side of the piston, and the pressurized fluid in the two individual chambers (space between the actuator cylinder and the piston on each side of the piston) generates a resulting pushing or pulling force on the piston which produces an extending or retracting motion of the piston, respectively. On the other hand, the vertical actuators are single-acting with the (downward) pulling force which can be generated by the gravity forces from the platen and specimen and the nitrogen pre-charge in the hold-down struts, and the (upward) pushing force which is generated by the pressurized fluid inside the only actuator chamber located under the piston. Servovalves control how much fluid enters or leaves each actuator chamber by operating the spool displacement. For each of the single-acting vertical actuators, a 3-way servovalve is used to control the flow in each of the following three ways: (i) from the pressure supply line (or port) to the servovalve (uni-directional flow), (ii) from inside the servovalve to the return line (uni-directional flow), and (iii) between the actuator only chamber and the servovalve (two-directional flow) (see Figure 4.1(b)). Similarly, each double-acting horizontal actuator is fitted with two 4-way servovalves operating in parallel to regulate the flow into the actuator chambers (see Figure 4.1(a)). Each actuator piston transfers the force resulting from the pressurized fluid within the two actuator chambers to the platen via additional mechanical components. For the horizontal actuators, the path of the hydraulic force is: piston – piston rod – platen (or front) swivel – platen, while for the vertical actuators, the hydraulic force is transferred directly from the piston to the platen through the hydraulic film between the pressure-balanced bearing on top of the piston and the bottom of the platen.

The hydraulic dynamics can be separated in two parts: (1) the fluid flow controlled by the servovalve spool displacement which changes the volume of each actuator chamber, and (2) the mass continuity (or conservation) of the fluid in each actuator chamber that is governed by a differential equation for the chamber pressure. In this section, the flow nonlinearities are presented first, and then the mass flow continuity differential equation of each chamber is solved for the chamber fluid pressure considering the flow into or out of the chamber. Eventually, the force acted by each actuator is obtained as the resultant of the chamber hydraulic forces (fluid pressure multiplied by effective piston area).

4.1.1 Inner Working of Servovalves

4-way and 3-way servovalves are mounted on the horizontal and vertical actuators, respectively, to control the flows through the actuators, which are governed by the pressure difference between the chamber and supply/return pressures, from the higher to the lower pressure side. Servovalve ports (or servovalve ways) are defined below and shown in Figure 4.1.

- **P**: port feeding the fluid from the supply pressure line to the servovalve (uni-directional).
- **T**: port directing the fluid from the servovalve to the return pressure line (uni-directional).
- **A**: port connecting the servovalve and chamber A of the actuator (bi-directional).
- **B**: port connecting the servovalve and chamber B of the actuator (bi-directional).

Note that the flows through ports P and T are uni-directional, while the flows through ports A and B are bi-directional. In Figure 4.1(a), a 4-way servovalve is controlling a single-ended (i.e., different effective piston areas in chambers A and B) and double-acting horizontal actuator through a spool, and the supply flow and return flows are visualized as solid and dashed arrows, respectively. When the spool moves to the left (defined as positive spool displacement), the supply pressure line is connected to chamber A, and chamber B is connected to the return pressure line. Hence, the volumes of chamber A and chamber B increase and decrease, respectively; then the piston rod extends (defined as positive actuator velocity). Similarly, when the spool moves to the right (negative spool displacement), the piston rod retracts (negative actuator velocity). Based on the two situations described above, 4 flow paths are defined below and also shown in Figure 4.1(a):

- Q_1: flow from port **P** to port **A** (or inflow to actuator chamber A) when the spool displacement is positive.
- Q_2: flow from port **B** to port **T** (or outflow from actuator chamber B) when the spool displacement is positive.
- Q_3: flow from port **A** to port **T** (or outflow from actuator chamber A) when the spool displacement is negative.
- Q_4: flow from port **P** to port **B** (or inflow to actuator chamber B) when the spool displacement is negative.

Figure 4.1(b) shows a 3-way servovalve controlling a single-acting vertical actuator, in which the flows Q_2 and Q_4 are undefined since chamber B does not exist in the vertical actuators.

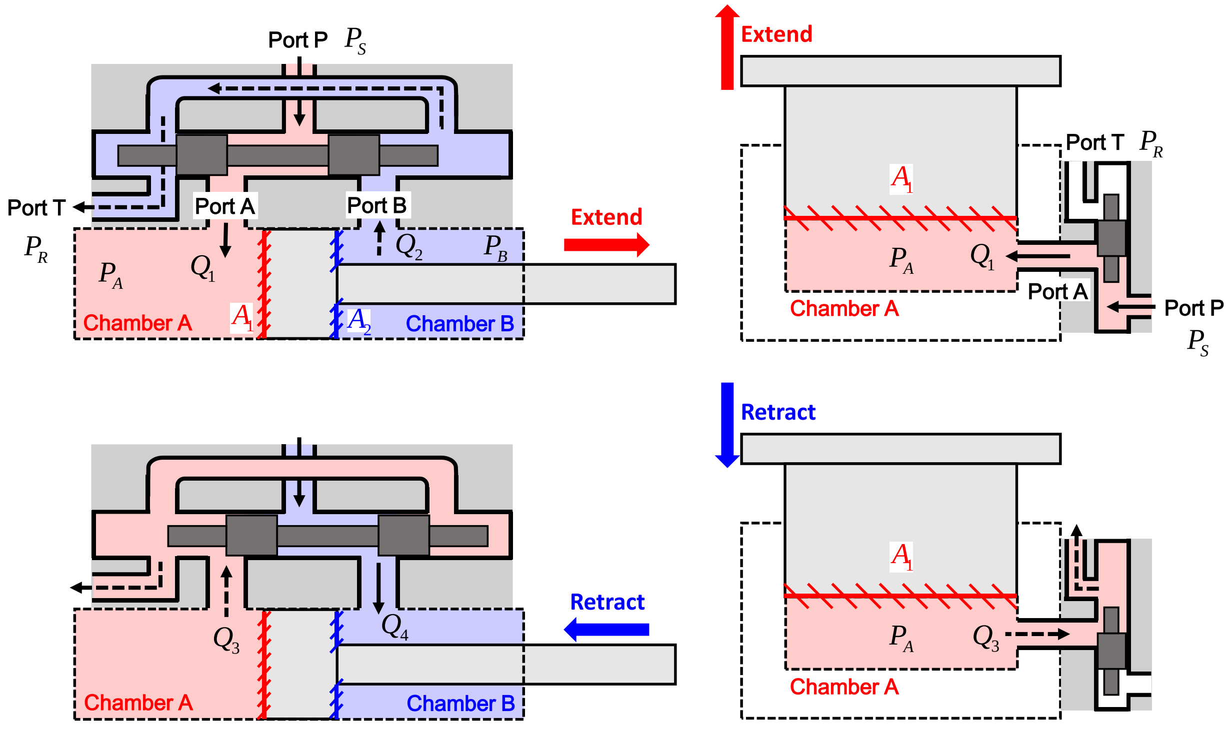

(a) **(b)**

Figure 4.1 **Sectional plots of 4-way and 3-way servovalves and actuators: (a) 4-way servovalve mounted on a horizontal actuator; and (b) 3-way servovalve mounted on a vertical actuator.**

4.1.2 Servovalve Spool Displacement and Flow Nonlinearities

The flow into or out of an actuator chamber is directly proportional to the area of the respective port or orifice, calculated as the product of the port width and the spool displacement. The horizontal actuators of the LHPOST6 are single-ended, which means that the two sides of the piston have different areas (the whole piston cross-section area on one side, and the rod cross-section area subtracted from it on the other side). In order to reduce the pressure discontinuity when the piston motion reverses its direction, the four port widths of a servovalve used to control a single-ended actuator are designed with the following properties [Merritt 1967]:

$$\frac{w_1}{w_3}=\left(\frac{A_2}{A_1}\right)^{0.5},\ \frac{w_2}{w_3}=\left(\frac{A_2}{A_1}\right)^{1.5},\ \frac{w_4}{w_3}=\left(\frac{A_2}{A_1}\right)^{1} \tag{4-1}$$

where w_1, w_2, w_3, w_4 are the port widths of the orifices enabling the flows Q_1, Q_2, Q_3, Q_4, respectively, and A_1 and A_2 denote the piston areas on the side of chamber A and B, respectively, as shown in Figure 4.1(a). The relation between the servovalve spool displacement and the hydraulic flow is nonlinear and is a function of three dimensionless parameters: (1) the servovalve spool displacement normalized by the spool stroke, (2) the servovalve port width ratios defined in Equation (4-1), and (3) the square root of the pressure difference between both sides of the flow path normalized by a constant (characteristic) pressure (originating from Bernoulli's equation/principle to determine the flow through an orifice, also known as *pressure drop – flow nonlinearity*). Integrating all three parameters, the orifice equation which provides the relation between the flow through the orifice, the servovalve spool displacement, and the pressure drop across the orifice result in [Merritt 1967]

$$\begin{aligned}
Q_1&=q\cdot\left(1-e^{-\lambda\cdot|x_v|/x_{v,\max}}\right)\cdot\frac{w_1}{w_3}\cdot\frac{\sqrt{P_S-P_A}}{\sqrt{P_{rated}}} \quad , \quad Q_2=q\cdot\left(1-e^{-\lambda\cdot|x_v|/x_{v,\max}}\right)\cdot\frac{w_2}{w_3}\cdot\frac{\sqrt{P_B-P_R}}{\sqrt{P_{rated}}}\\
Q_3&=q\cdot\left(1-e^{-\lambda\cdot|x_v|/x_{v,\max}}\right)\cdot\frac{w_3}{w_3}\cdot\frac{\sqrt{P_A-P_R}}{\sqrt{P_{rated}}} \quad , \quad Q_4=q\cdot\left(1-e^{-\lambda\cdot|x_v|/x_{v,\max}}\right)\cdot\frac{w_4}{w_3}\cdot\frac{\sqrt{P_S-P_B}}{\sqrt{P_{rated}}}
\end{aligned} \tag{4-2}$$

where q is a flow coefficient which can be calibrated through tests; x_v and $x_{v,\max}$ are the servovalve spool displacement and stroke, respectively; λ is a parameter that determines the nonlinearity of the flow vs. spool displacement curve due to the *flow-gain nonlinearity*; P_S, P_R, P_A, P_B denote the supply pressure, return pressure, and the pressure in the two actuator chambers A and B; P_{rated} is a constant referred to as rated pressure used to calibrate the flow vs. spool displacement curve and normalize the pressure drop. If the internal leakage flow across the actuator piston resulting from the pressure difference between chambers A and B is considered, the net flow into or out of chambers A and B (Q_A and Q_B) can be expressed as

$$\begin{aligned}
x_v>0,&\ \begin{cases} Q_A=Q_1-C_L\left(P_A-P_B\right)\\ Q_B=-Q_2+C_L\left(P_A-P_B\right)\end{cases}\\
x_v<0,&\ \begin{cases} Q_A=-Q_3-C_L\left(P_A-P_B\right)\\ Q_B=Q_4+C_L\left(P_A-P_B\right)\end{cases}
\end{aligned} \tag{4-3}$$

where C_L is the coefficient for the internal leakage flow across the piston, and the leakage flow is assumed to be proportional to the pressure drop across the actuator piston. Equations (4-2) and (4-3) are defined for 4-way servovalves but can be adapted for 3-way servovalves by setting $w_1 = w_3$, $w_2 = w_4 = 0$, $Q_B = 0$ and $P_B = 0$.

4.1.3 Hydraulic Flow Dynamics and Actuator Forces

Assuming that the hydraulic flow is compressible, the following differential equation describing the actuator chamber flow dynamics can be derived from the mass continuity (conservation) equation [Merritt 1967, Eq. (3-53); Ozcelik et al. 2021]:

$$\frac{dP}{dt} = \frac{\beta_e}{V}\left(Q - \frac{dV}{dt}\right) \tag{4-4}$$

where P is the pressure inside the chamber, β_e is the effective bulk modulus of the hydraulic fluid, Q is the net volume flow rate passing through the chamber, and V is the instantaneous volume of the chamber. For actuator chambers, the volume of the chamber (V) corresponds to the piston area (A) multiplied by the instantaneous chamber length (L_c). Hence, Equation (4-4) can be rewritten for each of the two chambers of a double-acting actuator as

$$\frac{dP_A}{dt} = \frac{\beta_e}{L_{c,A}}\left(\frac{Q_A}{A_1} - \dot{L}\right), \qquad \frac{dP_B}{dt} = \frac{\beta_e}{L_{c,B}}\left(\frac{Q_B}{A_2} + \dot{L}\right) \tag{4-5}$$

where $L_{c,A}$ and $L_{c,B}$ are the lengths of chamber A and B, respectively, which depend on the piston position, and $\dot{L}$ is the actuator piston velocity. The piston velocity is related to the chamber length rate of change as $\dot{L}_{c,A} = \dot{L}$ and $\dot{L}_{c,B} = -\dot{L}$ since when the piston rod extends (see Figure 4.1(a)), chamber A's length increases and chamber B's length decreases by the same amount. Once the pressures in both chambers are determined through the above state equations, Equation (4-5), the actuator force is obtained as the net force applied to the piston as

$$f_{hyd} = P_A A_1 - P_B A_2 \tag{4-6}$$

where f_{hyd} is the servo-hydraulic actuator force acting on the ″shake table platen plus moving parts of components attached to it″. Similarly, Equations (4-5) and (4-6) can be adapted for the vertical actuators by setting $P_B = 0$.

4.2 HOLD-DOWN STRUT FORCES

The hold-down struts have pre-charged nitrogen inside their bottom chamber (as shown in Figure 3.1(b)), and the nitrogen pressure depends on the length of the hold-down struts (i.e., the volume of the nitrogen chamber). The nitrogen inside each of the bottom chambers is modeled as an ideal gas following the polytropic process [Borgnakke 2013]:

$$P_{HDS} \cdot V_{HDS}^{n} = P_{0,HDS} \cdot V_{0,HDS}^{n} \tag{4-7}$$

where P_{HDS} and V_{HDS} are the instantaneous pressure of the nitrogen and the instantaneous volume of the chamber, respectively; $P_{0,HDS}$ and $V_{0,HDS}$ denote the pressure and volume of the chamber when the platen is in its control zero-position, and *n* is the polytropic index. Therefore, the pulling downward forces produced by the hold-down struts can be represented as a function of the initial pre-charge pressure and the displacement (i.e., change in length) of the hold-down strut as

$$f_{HDS} = -P_{HDS} \cdot A_{HDS} = -P_{0,HDS} \cdot A_{HDS} \cdot \frac{V_{0,HDS}^{n}}{V_{HDS}^{n}} = -P_{0,HDS} \cdot A_{HDS} \cdot \left(1 + \frac{\Delta L_{HDS}}{L_{c0,HDS}}\right)^{-n} \tag{4-8}$$

where A_{HDS}, $L_{c0,HDS}$, ΔL_{HDS} denote the effective piston area, initial bottom chamber length, and displacement (i.e., elongation) of the hold-down strut.

4.3 DISSIPATIVE FORCES

Three sources of energy dissipation modeled as dissipative forces are mainly considered in this study: (1) the planar sliding friction between the surface plates (pressure balanced bearings) on top of the vertical actuators and the glider plates bolted to the bottom of the platen, (2) the seal friction between the piston, piston rod and the cylinder of all actuators and hold-down struts, and (3) the viscous damping along the actuator direction assumed to be proportional to the actuator piston velocity. However, there are several additional sources of energy dissipation in the system (e.g., friction and viscous processes in the swivels of the actuators and hold-down struts), which are difficult to model and to estimate explicitly based on experimental data. Hence, the dissipative forces in the LHPOST6 are lumped into the three main sources defined above for modeling and simulation purposes.

The first source of energy dissipation is modeled using the two-dimensional Bouc-Wen friction (viscoplastic) model for each vertical actuator surface plate. This model is governed by the following coupled differential equation based on the theory of viscoplasticity [Park et al. 1985] and describes the relation between the relative velocities of the vertical actuator surface plates and platen glider plates and the resulting friction forces [Constantinou et al. 1990]:

$$\begin{cases} Y\dot{Z}_x = v_x - Z_x\left\{\tau \cdot \left(v_x Z_x + v_y Z_y\right) + (1-\tau) \cdot \left(\left|v_x Z_x\right| + \left|v_y Z_y\right|\right)\right\} \\ Y\dot{Z}_y = v_y - Z_y\left\{\tau \cdot \left(v_x Z_x + v_y Z_y\right) + (1-\tau) \cdot \left(\left|v_x Z_x\right| + \left|v_y Z_y\right|\right)\right\} \end{cases} \tag{4-9}$$

where *Y* represents the yield displacement (assumed isotropic) at which the ″material″ transforms its behavior from elastic to inelastic; Z_x and Z_y are two dimensionless (smooth) hysteretic quantities bounded between +1 and −1; v_x and v_y are the x and y components of the in-plane relative velocity between the vertical actuator surface plate and the corresponding glider plate; and τ is a dimensionless parameter controlling the shape of the friction hysteresis loops. Since the platen of the LHPOST6 is moving in all three translational directions (x, y and z), the following simple extension to Equation (4-9) is made (for convenience) to comply with the dimensions of the velocity vectors from the 3D rigid body kinematics component of the shake table model:

$$Y\dot{Z}_z = v_z = 0 \tag{4-10}$$

Upon solving Equations (4-9) and (4-10) for Z_x and Z_y, the friction forces (acting on the platen) along the x and y axes of the sliding plane ($F_{\mu x}$ and $F_{\mu y}$) are obtained as

$$\begin{cases} F_{\mu x} = -\mu W \cdot Z_x = -F_\mu \cdot Z_x \\ F_{\mu y} = -\mu W \cdot Z_y = -F_\mu \cdot Z_y \end{cases}, \qquad F_{\mu z} = 0 \tag{4-11}$$

where μ is the friction coefficient (assumed to be isotropic), W is the normal force acting on the sliding surface, $F_\mu = \mu W$, and $F_{\mu z} = 0$ is added to the set of equations similarly to Equation (4-10) .By combining Equations (4-9), (4-10), and (4-11), the two-dimensional friction model can be expressed in matrix form as

$$\begin{cases} Y \cdot \dot{\mathbf{Z}}_{slide} = \mathbf{v}_{slide} - H \cdot \mathbf{Z}_{slide} \\ H = \tau \cdot \left(\mathbf{v}_{slide} \right)^T \mathbf{Z}_{slide} + (1-\tau) \cdot \left| \mathbf{v}_{slide} \right|^T \left| \mathbf{Z}_{slide} \right| \\ \mathbf{f}_{slide} = -F_\mu \cdot \mathbf{Z}_{slide} \end{cases} \quad \text{where} \quad \begin{cases} \mathbf{v}_{slide} = \begin{bmatrix} v_x & v_y & v_z \end{bmatrix}^T \\ \mathbf{f}_{slide} = \begin{bmatrix} F_{\mu x} & F_{\mu y} & F_{\mu z} \end{bmatrix}^T \\ \mathbf{Z}_{slide} = \begin{bmatrix} Z_x & Z_y & Z_z \end{bmatrix}^T \end{cases} \tag{4-12}$$

However, for the LHPOST6, the surface plate of each vertical actuator is generally not aligned with the reference frame {s}, but is aligned with $\{\mathrm{n}_i\}$. According to the modified kinematics introduced in Section 3.4.2, the surface plate of the i^{th} vertical actuator is not rotating about its normal axis. The orientation of the surface plate can be represented by a set of local Euler angles including only two non-zero rotations (the surface plate is assumed to be connected to the actuator rod through a universal joint, which provides two rotational degrees of freedom as shown in Figure **3.2**). Meanwhile, the z axis of frame $\{\mathrm{n}_i\}$ coincides with the z axis of frame {b} since according to the kinematic constraint shown in Figure **3.2**(b), the vertical actuator surface plates do not separate from the sliding plane/surface. This kinematic constraint can be expressed as

$${}^{\mathrm{s}}\mathbf{R}_{\mathrm{n}_i} \cdot {}^{\mathrm{s}}\hat{\mathbf{z}}_{\mathrm{s}} = {}^{\mathrm{s}}\mathbf{R}_{\hat{y}}(\beta_{slide,i}) \cdot {}^{\mathrm{s}}\mathbf{R}_{\hat{x}}(\alpha_{slide,i}) \cdot {}^{\mathrm{s}}\hat{\mathbf{z}}_{\mathrm{s}} = {}^{\mathrm{s}}\mathbf{R}_{\mathrm{b}} \cdot {}^{\mathrm{s}}\hat{\mathbf{z}}_{\mathrm{s}}, \quad \text{with } {}^{\mathrm{s}}\hat{\mathbf{z}}_{\mathrm{s}} = \begin{bmatrix} 0 & 0 & 1 \end{bmatrix}^T \tag{4-13}$$

where $\alpha_{slide,i}$ and $\beta_{slide,i}$ are the local Euler angles of frame $\{\mathrm{n}_i\}$ relative to the orientation of reference frame {s}, and Equation (4-13) must be solved for these two angles. Then these two angles can be obtained by expanding ${}^{\mathrm{s}}\mathbf{R}_{\mathrm{n}_i}$ as, see Equation (3-3),

$$
{}^{\mathrm{s}}\mathbf{R}_{\mathrm{n}_i} = \begin{bmatrix} \cos\beta_{slide,i} & \sin\beta_{slide,i}\sin\alpha_{slide,i} & \sin\beta_{slide,i}\cos\alpha_{slide,i} \\ 0 & \cos\alpha_{slide,i} & -\sin\alpha_{slide,i} \\ -\sin\beta_{slide,i} & \cos\beta_{slide,i}\sin\alpha_{slide,i} & \cos\beta_{slide,i}\cos\alpha_{slide,i} \end{bmatrix} \tag{4-14}
$$

and by equating the third column of the rotation matrices ${}^{\mathrm{s}}\mathbf{R}_{\mathrm{n}_i}$ and ${}^{\mathrm{s}}\mathbf{R}_{\mathrm{b}}$. The uniqueness of the solution for these two Euler angles is guaranteed by the limited rotational stroke of the vertical actuator surface plates (the piston of a vertical actuator cannot rotate more than 2.0 degrees with respect to the actuator cylinder). The relative velocity between the platen and the center of the surface plate of a vertical actuator can be expressed as

$$
\begin{cases} {}^{\mathrm{s}}\mathbf{v}_{slide,i} = {}^{\mathrm{s}}\mathbf{v}^{\mathrm{P}_i'} - {}^{\mathrm{s}}\mathbf{v}^{\mathrm{P}_i} = {}^{\mathrm{p}_i'}\mathbf{v}^{\mathrm{P}_i'} - {}^{\mathrm{p}_i}\mathbf{v}^{\mathrm{P}_i} \\ {}^{\mathrm{n}_i}\mathbf{v}_{slide,i} = \left({}^{\mathrm{s}}\mathbf{R}_{\mathrm{n}_i}\right)^T \cdot {}^{\mathrm{s}}\mathbf{v}_{slide,i} \end{cases} \tag{4-15}
$$

where ${}^{\mathrm{p}_i'}\mathbf{v}^{\mathrm{P}_i'}$ and ${}^{\mathrm{p}_i}\mathbf{v}^{\mathrm{P}_i}$ are obtained from Equations (3-14) and (3-26), respectively. Note that the z component of ${}^{\mathrm{n}_i}\mathbf{v}_{slide,i}$ is always zero since the surface plates of the vertical actuators and the glider plates attached to the bottom of the platen are assumed to always be in the same sliding plane (see Section 3.4.2). ${}^{\mathrm{n}_i}\mathbf{v}_{slide,i}$ is then applied as $\mathbf{v}_{slide}$ into Equation (4-12) to find the friction forces in the $\{\mathrm{n}_i\}$ frame, ${}^{\mathrm{n}_i}\mathbf{f}_{slide,i}$, as

$$
\begin{cases} Y_i^{(2\mathrm{D})} \cdot \dot{\mathbf{Z}}_{slide,i} = {}^{\mathrm{n}_i}\mathbf{v}_{slide,i} - H_i \cdot \mathbf{Z}_{slide,i} \\ {}^{\mathrm{n}_i}\mathbf{f}_{slide,i} = -F_{\mu,i}^{(2\mathrm{D})} \cdot \mathbf{Z}_{slide,i} \qquad (i = 5, \ldots, 10) \end{cases} \tag{4-16}
$$

where $Y_i^{(2\mathrm{D})}$, $\tau_i^{(2\mathrm{D})}$ and $F_{\mu,i}^{(2\mathrm{D})}$ are the parameters Y, τ and F_μ specified for the sliding friction of the i^{th} vertical actuator. The sliding friction forces between the glider plate and the surface plate of a vertical actuator expressed in reference frame {s} can be obtained by applying the coordinate transformation to ${}^{\mathrm{n}_i}\mathbf{f}_{slide,i}$ as

$$
{}^{\mathrm{s}}\mathbf{f}_{slide,i} = {}^{\mathrm{s}}\mathbf{R}_{\mathrm{n}_i} \cdot {}^{\mathrm{n}_i}\mathbf{f}_{slide,i} \tag{4-17}
$$

The second source of energy dissipation is due to the seal friction of a component (including all horizontal actuators, vertical actuators, and hold-down struts) when its piston and rod are moving relative to its cylinder, which is a one-dimensional motion along the actuator direction. For each component of the LHPOST6, this energy dissipation mechanism is modeled using a uni-dimensional version of the two-dimensional Bouc-Wen friction (viscoplastic) model defined in Equations (4-9)to (4-11). In setting v_y and Z_y in Equation (4-9) to zero, the right hand side of the second state equation is zero, and the two coupled differential equations reduce to a single differential equation. The 1D friction model used to simulate the seal friction along the direction of each component has the form:

$$\begin{cases} Y_i^{(1\mathrm{D})} \cdot \dot{Z}_{seal,i} = \dot{L}_i - Z_{seal,i} \cdot \left\{ \tau_i^{(1\mathrm{D})} \cdot \dot{L}_i \; Z_{seal,i} + (1-\tau_i^{(1\mathrm{D})}) \cdot \left| \dot{L}_i \; Z_{seal,i} \right| \right\} \\ f_{seal,i} = -F_{\mu,i}^{(1\mathrm{D})} \cdot Z_{seal,i} \end{cases} \tag{4-18}$$

where $Y_i^{(1\mathrm{D})}$, $\tau_i^{(1\mathrm{D})}$ and $F_{\mu,i}^{(1\mathrm{D})}$ are the parameters Y, τ and F_μ specified for the seal friction of the i^{th} component, $\dot{Z}_{seal,i}$ is the corresponding dimensionless hysteretic quantity, and $f_{seal,i}$ is the scalar friction force acting on particle P_i' of the platen along the actuator direction. The third source of energy dissipation is due to viscous damping acting along each component (taken as the horizontal and vertical actuators) with the (linear) viscous damping forces assumed to be proportional to the piston velocity, i.e.,

$$f_{viscous,i} = -C_{v,i} \cdot \dot{L}_i \tag{4-19}$$

where $C_{v,i}$ is the viscous coefficient characterizing the i^{th} component, and $f_{viscous,i}$ is the scalar viscous damping force acting on particle P_i' of the platen along the actuator direction. Note that the dissipative forces along the hold-down struts are consolidated with those along the vertical actuators, as discerning between them using experimental data is challenging.

4.4 REFERENCE FRAME TRANSFORMATIONS OF FORCES AND TOTAL WRENCH ACTING ON THE PLATEN

The forces generated by the components (horizontal and vertical actuators and hold-down struts) and the energy dissipation mechanisms presented in Sections 4.1 to 4.3 are acting on the platen at the connection points (particles P_i' of the platen). Therefore, static analysis must be performed to transform these forces to the same reference frame and find the resultant external forces and moments acting on the platen. This section introduces wrenches, which are six-component vectors utilized in robotics and in this study to package the three-dimensional forces and moments together in the form ${}^{\mathrm{f}}\mathbf{F} = \left[\left({}^{\mathrm{f}}\mathbf{m}^{\mathrm{F}} \right)^T \quad \left({}^{\mathrm{f}}\mathbf{f}^{\mathrm{F}} \right)^T \right]^T$. In this notation, the particle F is the origin of reference frame {f}, and ${}^{\mathrm{f}}\mathbf{m}^{\mathrm{F}}$ and ${}^{\mathrm{f}}\mathbf{f}^{\mathrm{F}}$ denote the moment and force vectors, respectively, acting at particle F and with vector components expressed in frame {f}. To derive the frame transformation of wrenches, we employ the reference-independent property of power. Thus, the power produced by a wrench can be equally expressed in two arbitrary reference frames {f} and {g} as

$$\left({}^{\mathrm{g}}\mathbf{V} \right)^T \cdot {}^{\mathrm{g}}\mathbf{F} = \left({}^{\mathrm{f}}\mathbf{V} \right)^T \cdot {}^{\mathrm{f}}\mathbf{F} \tag{4-20}$$

where ${}^{\mathrm{f}}\mathbf{V}$ and ${}^{\mathrm{g}}\mathbf{V}$ are the twists defined in Equation (3-15), and ${}^{\mathrm{f}}\mathbf{F}$ and ${}^{\mathrm{g}}\mathbf{F}$ are the associated wrenches, equivalent to each other but expressed in frames {f} and {g}, respectively. Substituting Equations (3-16) into the left-hand side of Equation (4-20) yields

$$\left({}^{\mathrm{g}}\mathbf{V}\right)^T \cdot {}^{\mathrm{g}}\mathbf{F} = \left({}^{\mathrm{g}}\mathbf{J}_{\mathrm{f}}\,{}^{\mathrm{f}}\mathbf{V}\right)^T \cdot {}^{\mathrm{g}}\mathbf{F} = \left({}^{\mathrm{f}}\mathbf{V}\right)^T \cdot \left({}^{\mathrm{g}}\mathbf{J}_{\mathrm{f}}\right)^T \cdot {}^{\mathrm{g}}\mathbf{F} = \left({}^{\mathrm{f}}\mathbf{V}\right)^T \cdot \left({}^{\mathrm{f}}\mathbf{J}_{\mathrm{g}}^{-1}\right)^T \cdot {}^{\mathrm{g}}\mathbf{F} \tag{4-21}$$

from which the frame transformation of wrenches is obtained by comparing the right-hand sides of Equation (4-20) and (4-21), respectively, as

$${}^{\mathrm{f}}\mathbf{F} = \left({}^{\mathrm{f}}\mathbf{J}_{\mathrm{g}}^{-1}\right)^T \cdot {}^{\mathrm{g}}\mathbf{F} \tag{4-22}$$

In Equation (4-22), the matrix used to transform the wrench from frame {g} to frame {f} is obtained by inverting the Jacobian matrix used to transform the twists from frame {g} to frame {f} and then transposing the resulting matrix. The total forces from each component acting on its platen connection point are determined as

$${}^{\mathrm{P}_i'}\mathbf{f}^{\,\mathrm{P}_i'} = \begin{cases} \left(f_{hyd,i} + f_{seal,i} + f_{viscous,i}\right) \cdot {}^{\mathrm{s}}\hat{\mathbf{r}}^{\mathrm{A}_i\mathrm{P}_i}, & i = 1, 2, 3, 4 \quad \text{(horizontal actuators)} \\ \left(f_{hyd,i} + f_{seal,i} + f_{viscous,i}\right) \cdot {}^{\mathrm{s}}\hat{\mathbf{r}}^{\mathrm{A}_i\mathrm{P}_i} + {}^{\mathrm{s}}\mathbf{f}_{slide,i}\ , & i = 5, \ldots, 10 \quad \text{(vertical actuators)} \\ \left(f_{HDS,i} + f_{seal,i}\right) \cdot {}^{\mathrm{s}}\hat{\mathbf{r}}^{\mathrm{A}_i\mathrm{P}_i}, & i = 11, 12, 13 \quad \text{(hold-down struts)} \end{cases} \tag{4-23}$$

where $f_{hyd,i}$, $f_{HDS,i}$, ${}^{\mathrm{s}}\mathbf{f}_{slide,i}$, $f_{seal,i}$, and $f_{viscous,i}$ are given in Equations (4-6), (4-8), (4-17), (4-18), and (4-19), respectively. By using the frame transformation of wrenches from Equation (4-22), the resultant external wrench acting at the C.G. of the "platen plus moving parts", including the gravity forces, is

$${}^{\mathrm{b}}\mathbf{F}_{ext} = \begin{bmatrix} \mathbf{0} \\ \left({}^{\mathrm{s}}\mathbf{R}_{\mathrm{b}}\right)^T \end{bmatrix} \cdot \mathbf{M} \cdot \begin{bmatrix} 0 \\ 0 \\ -g \end{bmatrix} + \left({}^{\mathrm{c}}\mathbf{J}_{\mathrm{b}}\right)^T \cdot \left\{ \sum_{i=1}^{13} \left({}^{\mathrm{P}_i'}\mathbf{J}_{\mathrm{c}}\right)^T \cdot \begin{bmatrix} \mathbf{0} \\ {}^{\mathrm{P}_i'}\mathbf{f}^{\,\mathrm{P}_i'} \end{bmatrix} \right\} \tag{4-24}$$

where $\mathbf{M}$ is the (translational) mass matrix of the platen including the moving parts of the components, g is the gravitational acceleration, and ${}^{\mathrm{P}_i'}\mathbf{J}_{\mathrm{c}}$ and ${}^{\mathrm{c}}\mathbf{J}_{\mathrm{b}}$ are given in Equations (3-17) and (3-18), respectively.

4.5 RIGID BODY DYNAMICS OF THE PLATEN OF THE LHPOST6

The rigid body dynamics relates the twist and wrench using the dynamics of translational and rotational motions (translation and rotation dynamics), i.e., Newton's second law and Euler's rotation equation, respectively. In order to have constant inertia properties during the dynamic analysis, the equations of motion expressed in the body frame are often used, and their derivation will start from the time derivatives of the linear and angular momentum. Equations (3-1) and (3-2) show the same vector quantity expressed in two different reference frames and are followed by the definition of the two time differential operators. The relation between the two differential operators acting on an arbitrary vector quantity $\mathbf{u}$ considering the time-dependent reference frame can be written as [Lynch et al. 2017]

$$^{\mathrm{b}}\dot{\mathbf{u}} = \frac{d}{dt}\,^{\mathrm{b}}\mathbf{u} + \left[\,^{\mathrm{b}}\boldsymbol{\omega}\right]_{\times}\,^{\mathrm{b}}\mathbf{u} \tag{4-25}$$

where the second term on the RHS of the equation represents the contribution stemming from the time-dependence of the reference frame $\{\mathrm{b}\}$. Newton's 2nd law expresses that the net (translational) force $\mathbf{f}$ acting at the center of mass of a rigid body equals the time derivative of the linear momentum of the body (calculated using the velocity of the body at its center of mass ″B″, see Figure 3.1(c)). The equation of translational motion of the rigid body is obtained using Newton's second law and Equation (4-25) as

$$^{\mathrm{b}}\mathbf{f}^{\mathrm{B}} = \mathbf{M}\cdot\,^{\mathrm{b}}\dot{\mathbf{v}}^{\mathrm{B}} = \mathbf{M}\cdot\left(\frac{d}{dt}\,^{\mathrm{b}}\mathbf{v}^{\mathrm{B}} + \left[\,^{\mathrm{b}}\boldsymbol{\omega}\right]_{\times}\,^{\mathrm{b}}\mathbf{v}^{\mathrm{B}}\right) \tag{4-26}$$

where $\mathbf{M}$ denotes the (translational) mass matrix of the rigid body, which is time-invariant. Similarly, the equation of rotational motion of the rigid body expressed in the body reference frame $\{\mathrm{b}\}$ is obtained by using Euler's rotation equation (the net moment $\mathbf{m}$ acting at the center of mass of a rigid body equals the time derivative of the angular momentum $\boldsymbol{L}$ of the body defined as the product of the mass moment of inertia matrix of the body with respect to the body frame and the angular velocity vector expressed in the body frame) and Equation (4-25) to relate $^{b}\dot{\boldsymbol{L}}$ and $\frac{d}{dt}\,^{\mathrm{b}}\boldsymbol{L}$, i.e.,

$$^{\mathrm{b}}\mathbf{m}^{\mathrm{B}} = \frac{d}{dt}\left(^{\mathrm{b}}\mathbf{I}^{\mathrm{B}}\cdot\,^{\mathrm{b}}\boldsymbol{\omega}\right) + \left[\,^{\mathrm{b}}\boldsymbol{\omega}\right]_{\times}\cdot\left(^{\mathrm{b}}\mathbf{I}^{\mathrm{B}}\cdot\,^{\mathrm{b}}\boldsymbol{\omega}\right) \tag{4-27}$$

where $^{\mathrm{b}}\mathbf{I}^{\mathrm{B}}$ is the mass moment of inertia matrix of the rigid body with respect to the body frame. Since the origin of the reference frame $\{\mathrm{b}\}$ corresponds to the center of gravity ″B″ of the rigid body (see Figure 3.1(c)) and the orientation of frame $\{\mathrm{b}\}$ coincides with the principal axes of inertia of the body, $^{\mathrm{b}}\mathbf{I}^{\mathrm{B}}$ is time-invariant. Therefore, Equation (4-27) reduces to

$$^{\mathrm{b}}\mathbf{m}^{\mathrm{B}} = \,^{\mathrm{b}}\mathbf{I}^{\mathrm{B}}\cdot\frac{d}{dt}\,^{\mathrm{b}}\boldsymbol{\omega} + \left[\,^{\mathrm{b}}\boldsymbol{\omega}\right]_{\times}\,^{\mathrm{b}}\mathbf{I}^{\mathrm{B}}\cdot\,^{\mathrm{b}}\boldsymbol{\omega} \tag{4-28}$$

In the typical scenario where the mass matrix $\mathbf{M}$ can be expressed as $\mathrm{M}\cdot\mathbf{I}$ where M denotes the mass (scalar) of the body and $\mathbf{I}$ is the (3×3) identity matrix, Equations (4-26) and (4-28) for the translational and rotational dynamics of a rigid body, respectively, can be combined into a single equation as

$$ {}^{b}\mathbf{F}_{inert} = \begin{bmatrix} {}^{b}\mathbf{m}^{B} \\ {}^{b}\mathbf{f}^{B} \end{bmatrix} = {}^{b}\mathbf{G}^{B}\cdot\frac{d}{dt}\begin{bmatrix}{}^{b}\boldsymbol{\omega}\\ {}^{b}\mathbf{v}^{B}\end{bmatrix} + \begin{bmatrix}\left[{}^{b}\boldsymbol{\omega}\right]_\times & \mathbf{0}\\ \mathbf{0} & \left[{}^{b}\boldsymbol{\omega}\right]_\times\end{bmatrix}\cdot{}^{b}\mathbf{G}^{B}\cdot\begin{bmatrix}{}^{b}\boldsymbol{\omega}\\{}^{b}\mathbf{v}^{B}\end{bmatrix}, \quad {}^{b}\mathbf{G}^{B} = \begin{bmatrix}{}^{b}\mathbf{I}^{B} & \mathbf{0}\\ \mathbf{0} & \mathbf{M}\end{bmatrix} \tag{4-29}$$

where ${}^{b}\mathbf{F}_{inert}$ is the inertial wrench (vector comprising inertial moments and forces), ${}^{b}\mathbf{G}^{B}$ is the spatial inertia matrix of the rigid body, which combines the mass moment of inertia matrix ${}^{b}\mathbf{I}^{B}$ and the mass matrix $\mathbf{M}$. The equations of translational and rotational dynamics of the platen, also referred to as the equations of rigid body motion of the platen, are given by

$$ {}^{b}\mathbf{F}_{inert} = {}^{b}\mathbf{F}_{ext} \tag{4-30}$$

where ${}^{b}\mathbf{F}_{ext}$ is given in Equation (4-24). When the platen is in its control zero-position, a static analysis is conducted to determine the initial hydraulic actuator forces. This analysis utilizes a least-squares solution to address the under-determinacy of the system, which consists of 6 equilibrium equations with 10 unknowns. This static analysis can be performed by setting the left-hand side of Equation (4-30) to zero, as the platen is stationary. This implies that the hydraulic horizontal and vertical actuator forces are statically balanced by the gravity forces and hold-down strut forces (i.e., ${}^{b}\mathbf{F}_{ext} = \mathbf{0}$).

The mechanical part of the LHPOST6 comprises the platen and the moving parts of all components attached to it. When the platen is in an arbitrary displaced configuration, each component assumes a different relative configuration compared to when the platen is in its control zero-position. Consequently, solving the multi-rigid-body dynamics necessitates considering the dynamics of both the platen and individual components, accounting for the transfer of forces and moments between them, known as interface forces and moments. In this report, the inertial properties of the components are not derived analytically from their distributed mass properties. Instead, the effects of the inertial properties of the components on the effective inertial properties of the platen are derived using the lumped mass method. The effective inertial properties of the platen and moving parts of the components attached to it ($\mathbf{M}$ and ${}^{b}\mathbf{I}^{B}$) are derived in two different ways. In the first way, the weight of the platen alone (without glider plates) was measured during the crane lift-up operation (using the load cells integrated in the lifting cables) to remove the platen from the reaction mass to proceed with the construction of the 6-DOF upgrade. Then, the lumped mass contributions of all components attached to the platen including the new glider plates and the crash protection system (bumpers and their attachment plates) were added analytically to obtain a first estimate of the effective inertial properties, $\mathbf{M}_{\text{eff,1}}$ and ${}^{b}\mathbf{I}^{B}_{\text{eff, 1}}$. The mass moment of inertia properties of the platen alone with the glider plates and the crash protection system were obtained numerically from the detailed SolidWorks geometric model of the shake table with the mass density of the steel honeycomb platen calibrated to match the measured weight of the platen alone. It is important to note that the inertial effects of the steel cover plates (bridging the surrounding gap between the platen and the reaction mass) are not accounted for in this report, since the model validation results presented in Chapter 6 were obtained using experimental data collected during the acceptance tests conducted without the presence of the steel cover plates. In the second way, the effective inertial properties of the platen and moving parts of the components attached to it were obtained through system identification performed using acceptance test data; this second estimate of the effective inertial properties are denoted as $\mathbf{M}_{\text{eff},2}$ and ${}^{b}\mathbf{I}^{B}_{eff,\,2}$. Table 4.1 provides the component contributions to the effective inertial properties of the platen of the LHPOST6 and a comparison of the two estimates of these effective inertial properties. It is observed that: (1) the discrepancy between these two estimates is small, up to 1.5% for the translational masses and up to 6.9% for the mass moments of inertia, and (2) the moving parts of the horizontal and vertical actuators and of the hold-down struts altogether contribute to 10-14% of the effective total translational masses of the platen, and to 5-22% of the effective total mass moments of inertia of the platen. It is also noticed that the effective translational masses in the three directions X, Y, and Z differ slightly (1.5% or less). The LHPOST6 model simulation results presented in Chapter 6 of this report are based on the inertial properties obtained through system identification using acceptance test results, $\mathbf{M}_{\text{eff},2}$ and ${}^{b}\mathbf{I}^{B}_{eff,\,2}$. Details about the comprehensive parameter estimation/identification of the numerical model of the LHPOST6 presented in this report, using acceptance and characterization test data, will be the object of a forthcoming report.

Table 4.1 Estimates of effective inertial properties of the platen and lumped mass contributions of all components attached to the platen.

	Effective Translational Mass [ton] or [KN-sec^2/m]			**Effective Mass Moment of Inertia [ton-m^2] or [KN-sec^2-m]**		
	X-dir	Y-dir	Z-dir	X-dir	Y-dir	Z-dir
Platen alone with glider plates and crash protection system	148.80	148.80	148.80	893.53	2201.57	2973.27
Contributions of horiz. actuators	11.80	11.62	11.32	4.82	434.26	452.10
Contributions of vert. actuators	0	0	3.31	27.29	47.18	0
Contributions of hold-down struts	5.15	5.15	8.95	13.46	177.88	82.67
$\mathbf{M}_{\text{eff},1}$ and ${}^{b}\mathbf{I}^{B}_{eff,\,1}$	165.75	165.57	172.38	939.10	2860.89	3508.04
$\mathbf{M}_{\text{eff},2}$ and ${}^{b}\mathbf{I}^{B}_{eff,\,2}$	168.10	168.06	174.42	907.24	2683.41	3749.49
Discrepancy of second relative to first estimate (%)	1.42	1.50	1.18	-3.39	-6.20	6.88

5 CONTROL SOFTWARE (MTS 469D) AND MECHANICS-BASED NUMERICAL MODEL OF THE LHPOST6

The translational and rotational motions of the LHPOST6 are controlled by the MTS 469D Digital Control System (six-degree-of-freedom version). It was provided to the authors by MTS Systems Corporation [Thoen et al. 2004] for seamless integration into the numerical model of the LHPOST6 presented in Chapters 3 and 4. The 469D digital controller, referred to as 469D hereafter, provides the three-variable-control (TVC) loop for each of the six degrees of freedom of the LHPOST6. It incorporates advanced features including adaptive control methods such as Amplitude-Phase Compensation, Adaptive Harmonic Cancellation and Adaptive Inverse Control, as well as iterative methods like OnLine Iteration. These functionalities are employed to enhance the accuracy of reproducing sinusoidal waves and earthquake ground motions on the shake table platen. The block diagram representation of the 469D for each of the six DOFs of the LHPOST6 is shown in Figure 5.1. The three-variable controller (TVC) provides the basic control loop of the 469D. It uses displacement, velocity, and acceleration as the three state variables to be controlled and calculates the servovalve commands to the horizontal and vertical actuators. The TVC gain tuning is performed under a proper level (6-8%g RMS) of band-limited white noise acceleration in each degree of freedom separately until the ″total″ table transfer function between the reference (or desired) and feedback (or achieved) signals is as close to unity as possible [Luco et al. 2010]. When operating large servo-hydraulic shake tables like the LHPOST6, the TVC displacement loop is closed, meaning the displacement feedback gain is nonzero for each degree of freedom. However, the velocity and acceleration loops are kept open, with the velocity and acceleration feedback gains set to zero. This control setup is crucial for maintaining system stability and facilitating the tuning process. All three state variables as well as the jerk (time derivative of the reference/target acceleration) are used as feedforward signals in the TVC loop with feedforward gains to tune the total table transfer function in various frequency ranges [Conte and Trombetti 2000; Ozcelik et al. 2020]. Reproducing sinusoidal waves on the platen requires the use of amplitude-phase compensation (APC) to minimize the amplitude and phase differences between the reference and feedback signals at the desired (referred to as fundamental) frequency, and adaptive harmonic cancellation (AHC) to cancel the harmonic distortions (caused by the super-harmonics at multiples of the fundamental frequency) due to the flow nonlinearity in the hydraulic dynamics and other sources of nonlinearity in the system. Accurate reproduction of earthquake ground motions (i.e., broad-band random type signals) requires a strategy combining adaptive inverse control (AIC) and online iteration (OLI) both available in the 469D [Luco et al. 2010; Ozcelik et al. 2021]. AIC first identifies (learns) the shake table system dynamics by running band-limited acceleration white noise signals on the platen and estimating the inverse of the (6×6) matrix table transfer function between the 6-DOF command input and the corresponding 6-DOF feedback output within the operating frequency range of the system (0-33 Hz). Then the inverse transfer function is used in the AIC (which is a module of the 469D) to shape (or condition) the reference input so that the achieved table motion is as close as possible to the reference/desired signal. If the shake table was a linear dynamic system, AIC (with the exact system transfer function) would make the platen motion coincide with the reference signal. However, numerous sources of nonlinearity exist in the system, including the flow nonlinearity in the servovalves and friction forces at various component joints and connections, and the estimated table transfer function does not completely and exactly characterize the nonlinear LHPOST6 system dynamics. To further reduce the error between the reference and feedback signals, the 469D uses an iterative time history matching technique called online iteration (OLI) which modifies the command input to the 469D controller (referred to as drive file) repeatedly by adding the results of filtering the error signal through the inverse system transfer function (estimated through AIC) to the drive file at the previous iteration until there is no more improvement in the achieved table motion.

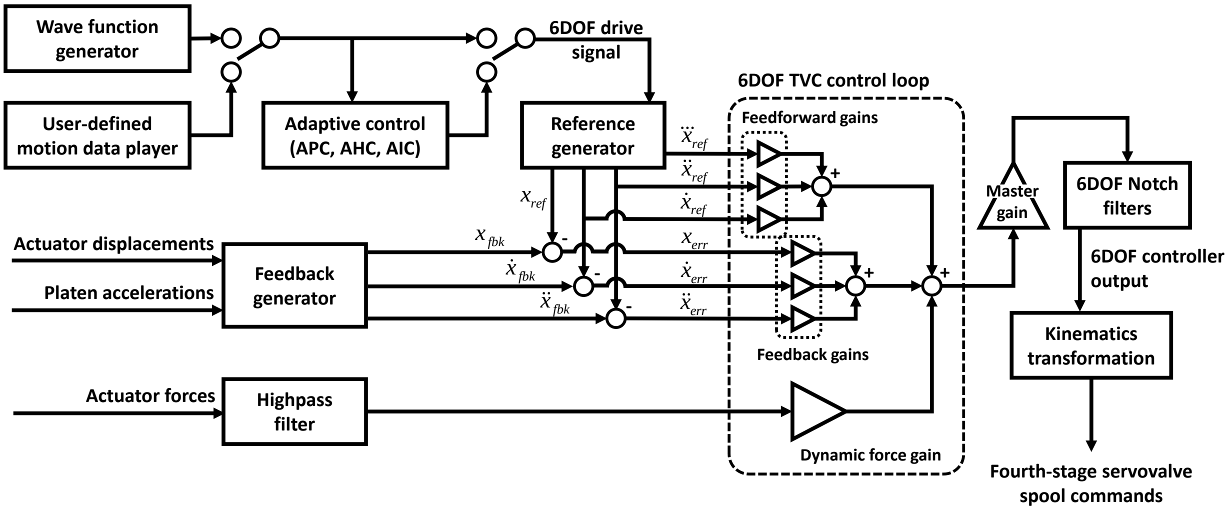

Figure 5.1 Block diagram representation of the MTS 469D Digital Control System for each of the six DOFs of the LHPOST6.

The mechanics-based numerical model of the LHPOST6 is programmed in Matlab/Simulink[1], including the kinematics of the platen and components (Chapter 3), the forces and moments (i.e., wrench) acting on the platen (Sections 4.1–4.4), and the rigid body dynamics of the platen and components (Section 4.5). The communication interface between the 469D and Simulink are also programmed in Simulink using the User Datagram Protocol (UDP) to transfer the calculation results of the 6-DOF TVC of the 469D to Simulink and the simulated actuator and platen motions from Simulink to the 469D. The stability, accuracy and computational efficiency of the numerical model of the LHPOST6-469D closed-loop system were evaluated/tested by repeatedly halving the integration time step starting from $\Delta t = 1/2048$ sec (the sampling rate of the 469D controller is 2048 Hz) until the difference between the simulated responses of the shake table system obtained

---

[1] The MathWorks Inc. (2016). MATLAB version: 9.0.0 (R2016a), Natick, Massachusetts: The MathWorks Inc. https://www.mathworks.com

using a specified value of Δt and $\Delta t/2$, respectively, can be neglected. A good trade-off between stability, accuracy and computational efficiency was reached by using $\Delta t = (1/2048)/4 = 1/8192$ sec when using the explicit forward Euler integration method.

A high-level block diagram of the numerical model of the LHPOST6 (considered as the plant to be controlled) is shown in Figure 5.2, where the input to the open-loop model of the LHPOST6 consists of the (fourth stage) spool displacements of the hydraulic servovalves of the horizontal and vertical actuators (which were measured during some acceptance tests), and the output from the open-loop model is the platen motion and actuator displacements. The open-loop model comprises three subsystems: (1) the hydraulic dynamics subsystem calculates the port flows based on the spool displacements, and then solves the mass flow continuity differential equations to find the chamber pressures and resulting actuator forces; (2) the hold-down strut dynamics subsystem is represented by the governing equation of the polytropic process to determine the pull down forces on the platen applied by the hold-down struts based on their displacements; and (3) the mechanical parts kinematics and dynamics subsystem calculates the total forces and moments acting on the platen, solves the translational and rotational dynamics equations of the rigid platen, and then convert the platen motions to the actuator and hold-down-strut displacements (inverse kinematics) which are needed by the other two subsystems.

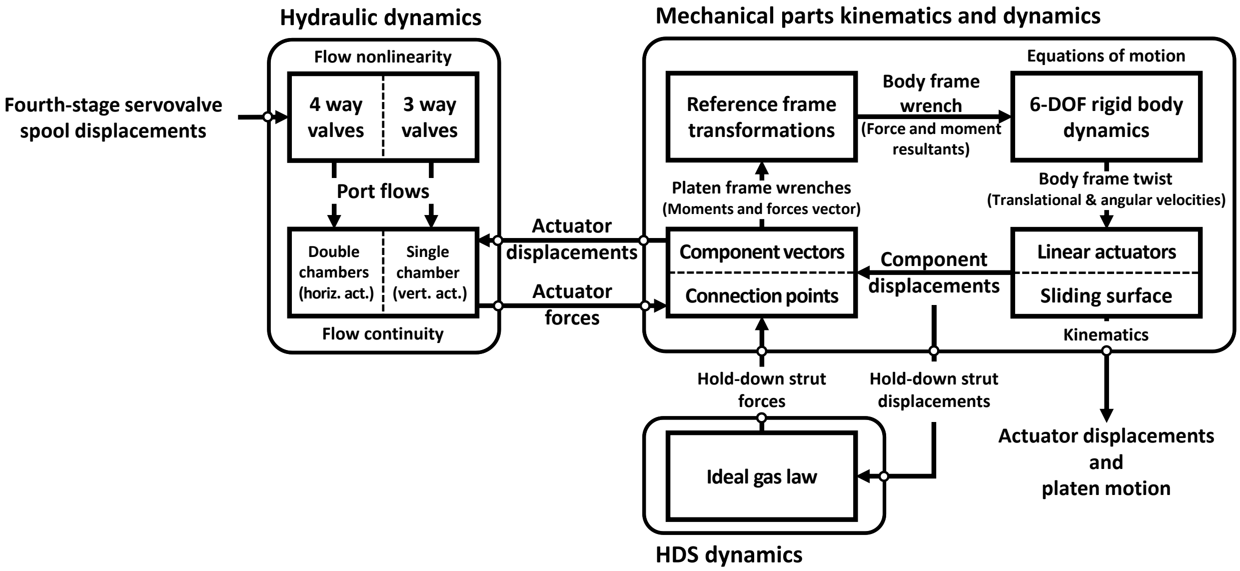

Figure 5.2 **High-level block diagram of the mechanics-based open-loop numerical model of the LHPOST6.**

A detailed block diagram of the kinematics and dynamics of the mechanical parts of the LHPOST6 is shown in Figure 5.3. The wrenches (combinations of forces and moments) exerted by the components on the platen and platen twist (combination of translational and angular velocities) can be expressed in different reference frames (see Table 3.1), and the transformations from one frame to another involve Jacobian matrices as shown in Equations (3-11), (3-14), (3-17) and (3-18) .Meanwhile, the relations between the platen motion (twist) and the component velocities along their axes are given in Equations (3-22) and (3-27). The forces exerted by the components at their connection points with the platen and expressed in frame $\{p_i'\}$ are provided in Equation (4-23). Then frame transformations are performed to obtain the resultant external wrench (including the gravity forces) at the C.G. ″B″ of the "platen plus moving parts" (see Figure 3.1(c)) expressed in frame {b} and given in Equation (4-24).

The equations of translational and rotational dynamics of the rigid platen are formed based on Equations (4-29) and (4-30). These equations are then solved numerically using the forward Euler integration method, yielding the platen twist expressed in reference frame {b}, which is fixed (frozen) at the current time step and serves as an inertial reference frame. Then the twist of the platen relative to frame {c} and the components' configurations (i.e., the locations and velocities of their platen connection points and the time rate of change of their lengths, $\dot{L}_i$) are determined through the utilization of transformations between reference frames. Ultimately, by integrating the translational velocities of the platen expressed in frame {c} over time, along with the Euler angle rates ${}^{E}\boldsymbol{\omega}$ (derived from ${}^{b}\boldsymbol{\omega}$ and using the transformation in Equations (3-11)), the position and orientation of the platen are determined. The latter are then utilized to update the reference frames ({b}, {c}, etc.) and the corresponding Jacobian matrices for the next time step.

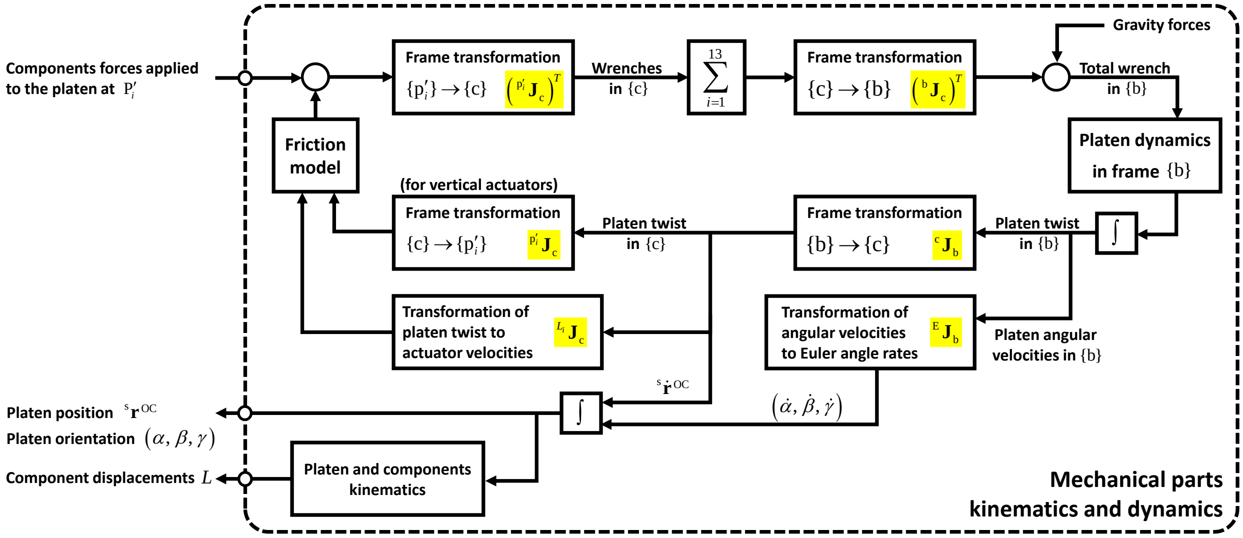

Figure 5.3 **Detailed block diagram of the mechanical parts kinematics and dynamics subsystem.**

6 EXPERIMENTAL VALIDATION OF THE DEVELOPED MODEL OF THE LHPOST6 UNDER BARE TABLE CONDITION

The experimental data used to calibrate and validate the model of the LHPOST6 presented herein were recorded during the acceptance testing conducted in the period August 2021 – February 2022 to verify that the actual performance of the LHPOST6 complies with the designed specifications. The acceptance test procedure involved the reproduction of various types of displacement or acceleration time histories on the platen, including periodic waves (triangular and sinusoidal wave tests) of different frequencies and amplitudes, and earthquake ground acceleration (or displacement) records. The sinusoidal wave tests were conducted to verify that the LHPOST6 can attain the design maximum displacement, velocity, and acceleration for each degree of freedom, while maintaining acceptable harmonic signal distortion. Triangular wave tests were carried out to assess the level of energy dissipation in the shake table system (platen with attached components) pre and post the 6-DOF upgrade. Both the sinusoidal and triangular wave tests were used to calibrate parameters of the numerical model of the LHPOST6 by applying to each degree of freedom separately a least-squares approach similar to the one used by Ozgur et al. [2008]. The numerical values assigned to the model parameters, either through direct specification or calibration using test data, as introduced in the previous sections, are listed in Table 6.1. The earthquake ground motions were selected during the design phase of the shake table upgrade project and reproduced on the shake table platen as part of the acceptance tests to verify the signal reproduction fidelity of the LHPOST6 (under bare table condition) by assessing the relative root mean square error between the reference and feedback earthquake ground acceleration (or displacement) time histories [Luco et al. 2010]. The motions of the platen and components, as well as the forces exerted by the components, which were recorded during the aforementioned tests, are utilized for the validation of the numerical model of the LHPOST6 presented in this report.

6.1 COMPARISON OF NUMERICALLY SIMULATED AND EXPERIMENTAL FORCES ACTING ON THE SHAKE TABLE PLATEN THROUGH INVERSE DYNAMICS

The external forces applied to the platen of the LHPOST6 by the hydraulic actuators are in dynamic equilibrium with the inertia forces (the effective inertial properties account for the translational mass and mass moment of inertia of the platen and of all moving parts of the attached components), energy dissipative forces, and restoring forces produced by the pre-charged nitrogen in the hold-down struts, as expressed by the equations of motion of the platen in Equation (4-30) [Ozcelik et al. 2008]. The recorded or derived (through composite filtering in the 469D) table motion (i.e., the translational acceleration, velocity, and displacement along each of the 3 DOFs expressed in frame {c} and the three Euler angles related to frame {c} as well as their first and second time derivatives) as provided by the 469D for certain acceptance tests are used to construct the experimental platen twist $\left[\left({}^{\mathrm{b}}\boldsymbol{\omega}\right)^{\mathrm{T}}\left({}^{\mathrm{b}}\mathbf{v}^{\mathrm{B}}\right)^{\mathrm{T}}\right]^{\mathrm{T}}$ and its time derivative using the reference frame transformations specified in Equations (3-11) and (3-18). The experimental platen twist and its time derivative are then used as input in the developed model of the LHPOST6 to compute the inertia forces from Equation (4-29), the total dissipative (friction + viscous) forces from Equations (4-23) and (4-24), and the HDS restoring forces from Equation (4-8). This procedure is referred to as inverse dynamics, i.e., use of the table motion to determine the various forces acting on the platen. The individual HDS restoring forces, total dissipative forces and inertia forces are extracted from the experimental forces using the measured nitrogen pressure in the HDS′s and the measured hydraulic actuator forces. Seven tri-axial earthquake ground motion tests are utilized for the subsequent comparison study, namely Tabas, TCU065, Takatori, RRS, Nepal, AC156 [ICC Evaluation Services Inc. 2007], and El Centro, see Table 6.2. The numerical and experimental results are compared, for each translational degree of freedom separately, in Figure 6.1 for the three triangular wave tests defined in Table **6.3**, and in Figure 6.2 through Figure 6.8 for the seven tri-axial earthquake ground motion tests defined in Table 6.2 The numerical and experimental response quantities of the LHPOST6 which are compared in these figures are: (1) the total actuator force components versus time, and corresponding table displacement and velocity components, respectively (see first three rows of Figure 6.1 through Figure 6.8), (2) the total HDS restoring force components versus the corresponding table displacement components (see fourth row of Figure 6.1 through Figure 6.8), and (3) the total dissipative force components versus the corresponding table displacement and velocity components (see last two rows of Figure 6.1 through Figure 6.8). Note that in this comparison, the numerical and experimental platen inertia forces are identical and computed from the experimental/measured platen motion and the inertia properties of the LHPOST6 model.

The recorded total actuator forces and table motions are low-pass filtered at the cut-off frequency of 30 Hz (the upper limit of the operational frequency bandwidth of the LHPOST6). The numerical simulations and experimental results generally exhibit good agreement across various cases. The largest discrepancies between numerical and experimental results are observed for the total dissipative forces in both the triangular wave tests and tri-axial earthquake ground motion tests. It is important to note that the total dissipative forces are considerably smaller in magnitude compared to the inertia forces and HDS restoring forces, which renders them more challenging to extract from the total actuator forces. Also, the dissipative forces stem from more intricate mechanics than the inertia and HDS restoring forces. Nevertheless, the dissipative force models utilized in this study capture the key aspects of the experimentally determined total dissipative forces. These comparative results validate the inertia properties of the platen, the gas constant (n) of nitrogen within the hold-down struts, and the parameters governing the friction and viscous dissipative forces.

Table 6.1 **Numerical values of parameters of the mechanics-based model of the LHPOST6.**

Parameter	**Value**	**Parameter**	**Value**
Hydraulic actuators		Hold-down struts	
A_1, A_2 of horizontal actuators	0.2027, 0.1297 m^2	$P_{0,HDS}$	15.2 MPa
A_1 of vertical actuators	0.5150 m^2	A_{HDS}	0.1500 m^2
q, λ for horizontal actuators	16929 lt/min, 1.30	$L_{c0,HDS}$	1.9638 m
q, λ for vertical actuators	23470 lt/min, 1.05	n (polytropic index)	1.75
P_S, P_R, P_{rated}, β_e	20.7, 0.55, 6.89, 896 MPa		
C_L (leakage coefficient)	2.75 (lt/min)/MPa		
Servovalve time delays	5 msec		
Dissipative forces			
$Y_i^{(2D)}$, $\tau_i^{(2D)}$ for vert. actuators	1 mm, 0.1	$F_{\mu,i}^{(2D)}$ for vert. actuators	17.17 kN
$Y_i^{(1D)}$, $\tau_i^{(1D)}$ for horiz. actuators	0.2 mm, 0.1	$F_{\mu,i}^{(1D)}$ for horiz. actuators	9.25 kN
$Y_i^{(1D)}$, $\tau_i^{(1D)}$ for vert. actuators	0.2 mm, 0.1	$F_{\mu,i}^{(1D)}$ for vert. actuators	13.33 kN
$C_{v,i}$ for horiz. actuators	15.06 kN(s/m)	$C_{v,i}$ for vert. actuators	7.71 kN(s/m)

Table 6.2 **Characteristics of translational earthquake ground motion tests conducted on the LHPOST6.**

Event Name	**Station Name**	**M**	**Abbr.**	**PGA (g)**			**PGV (m/s)**			**PGD (m)**		
				X	**Y**	**Z**	**X**	**Y**	**Z**	**X**	**Y**	**Z**
Tabas, 1978	Tabas, Iran	7.4	Tabas	0.97	0.88	0.72	1.01	0.87	0.33	0.61	0.33	0.12
ChiChi, Taiwan, 1999	TCU065	7.6	TCU065	0.72	0.49	0.23	0.82	0.73	0.38	0.36	0.24	0.10
Kobe, 1995	Takatori, Japan	6.9	Takatori	0.62	0.67	0.28	1.21	1.23	0.16	0.40	0.30	0.04
Northridge, 1994	Renaldi Receiving Station	6.7	RRS	0.87	0.47	0.96	1.48	0.75	0.42	0.42	0.23	0.04
Nepal, 2015	Kathmandu, Nepal	7.8	Nepal	0.16	0.17	0.15	0.42	0.40	0.25	0.30	0.20	0.10
AC-156 compatible earthquake			AC156	1.01	0.96	0.71	1.04	1.13	0.77	0.22	0.21	0.12
Imperial Valley, 1940	El Centro	6.9	El Centro	0.28	0.21	0.18	0.31	0.31	0.09	0.08	0.24	0.03

Table 6.3 **Characteristics of three triangular wave tests conducted on the LHPOST6.**

Tests	**Direction**	**Displacement (m)**	**Velocity (m/s)**	**Frequency (Hz)**
TX5	X	0.762	0.305	0.1
TY4	Y	0.381	0.152	
TZ3	Z	0.127	0.051	

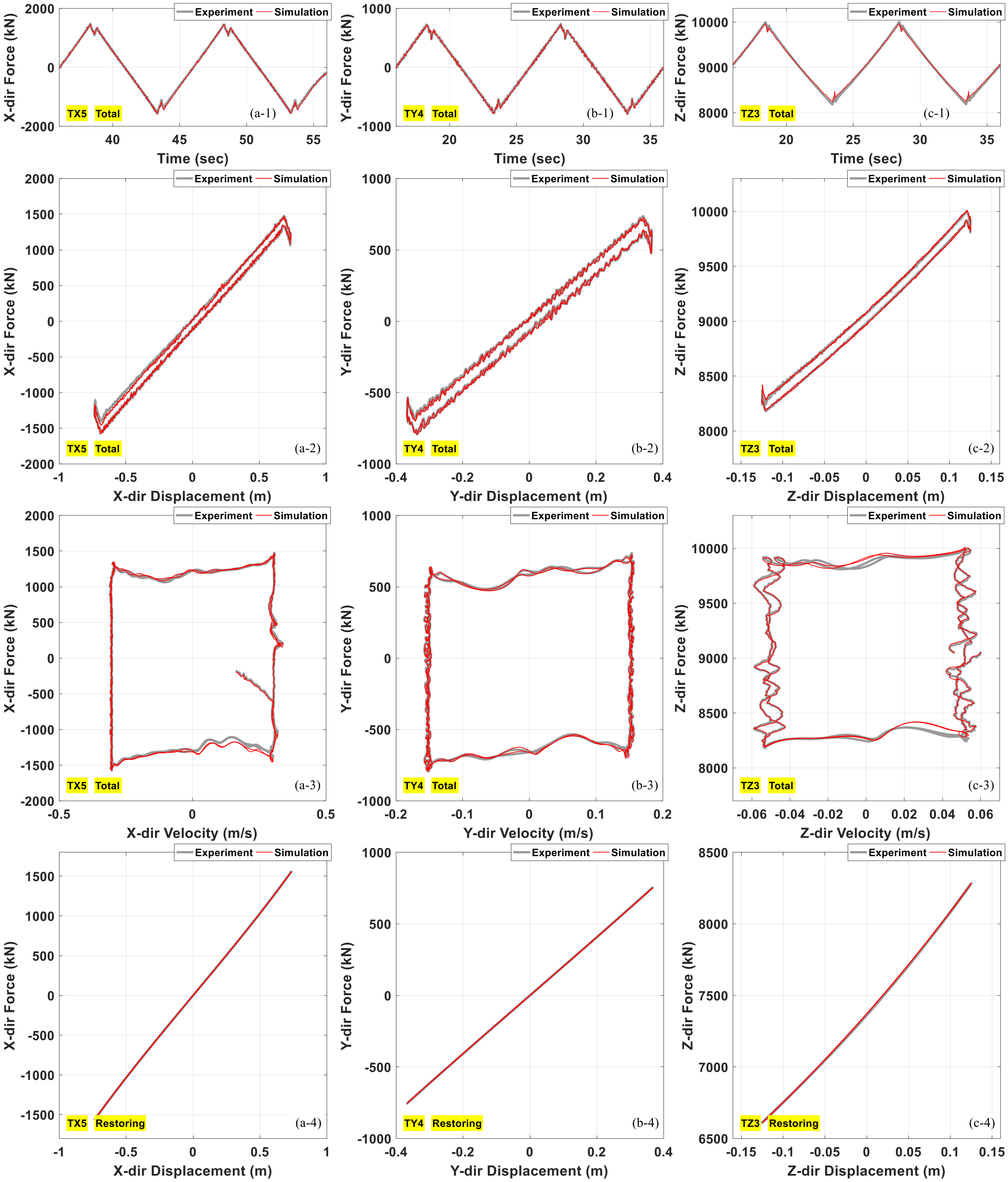

(Figure 6.1 is continued on next page)

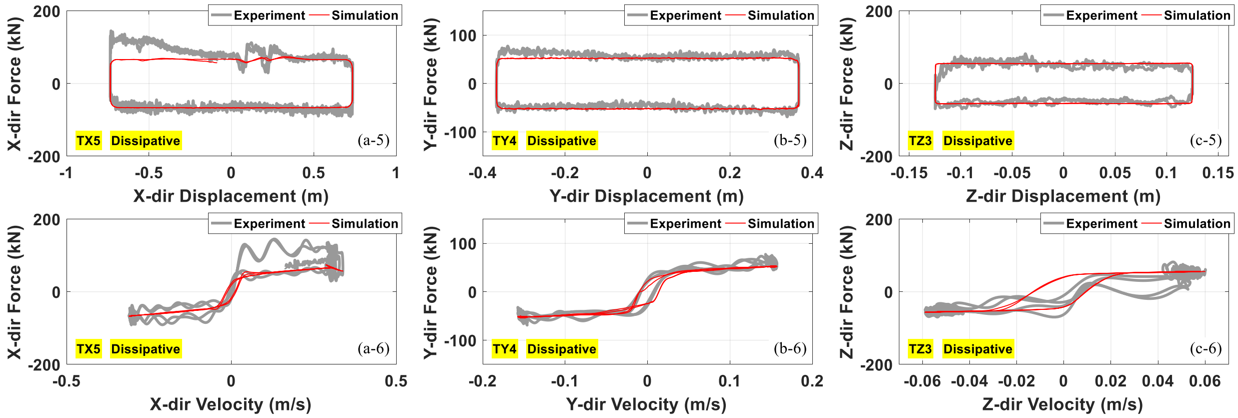

Figure 6.1 **Triangular wave tests TX5, TY4, and TZ4 defined in Table 6.3: Comparison of numerically simulated and experimental results in frame {c} for the total actuator force component time histories (in sub-figures a-1, b-1, c-1), total actuator force components vs. corresponding platen displacement components (in sub-figures a-2, b-2, c-2), total actuator force components vs. corresponding platen velocity components (in sub-figures a-3, b-3, c-3), HDS restoring force components vs. corresponding platen displacement components (in sub-figures a-4, b-4, c-4), total dissipative force components vs. corresponding platen displacement components (in sub-figures a-5, b-5, c-5), and total dissipative force components vs. corresponding platen velocity components (in sub-figures a-6, b-6, c-6).**

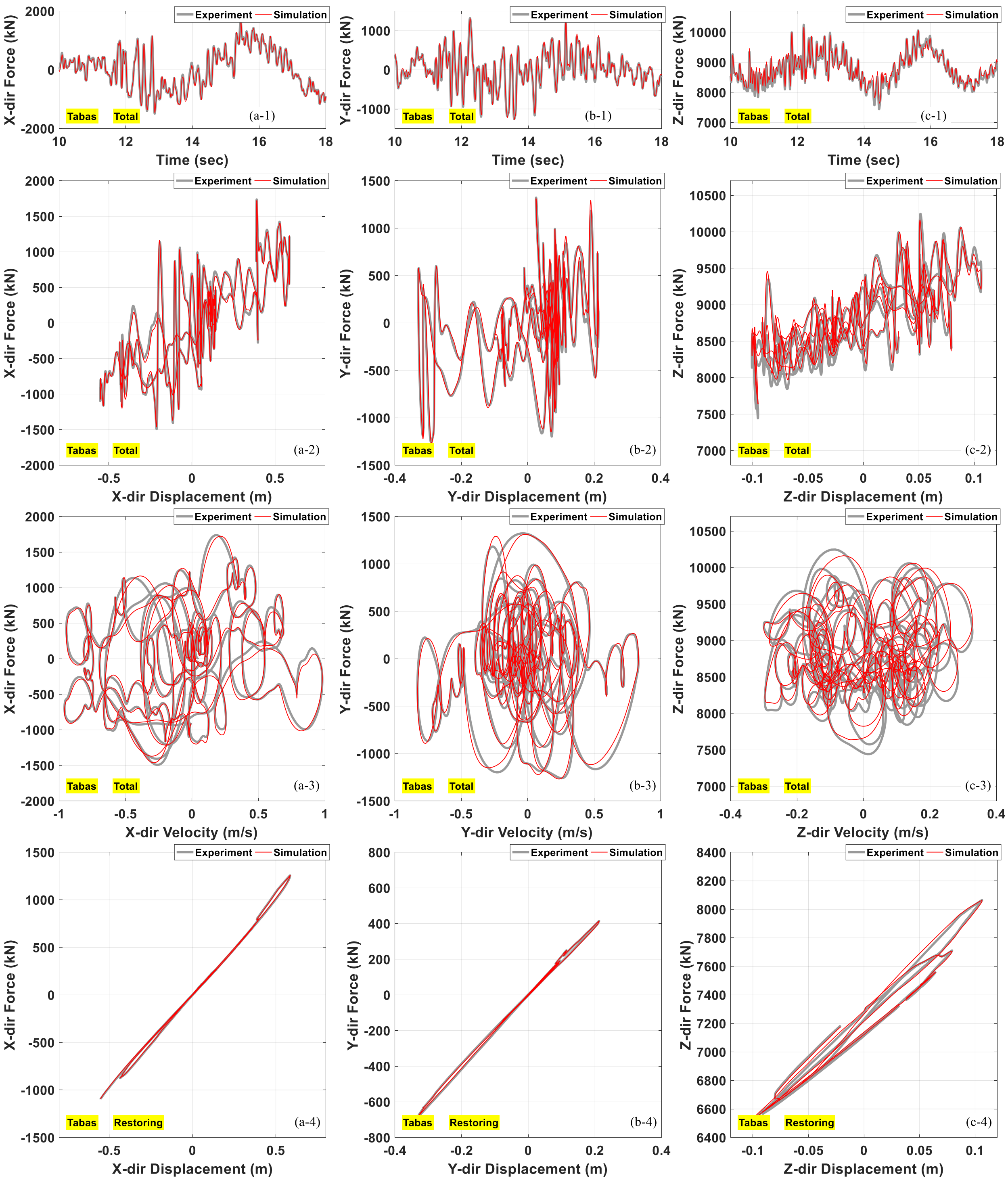

(Figure 6.2 is continued on next page)

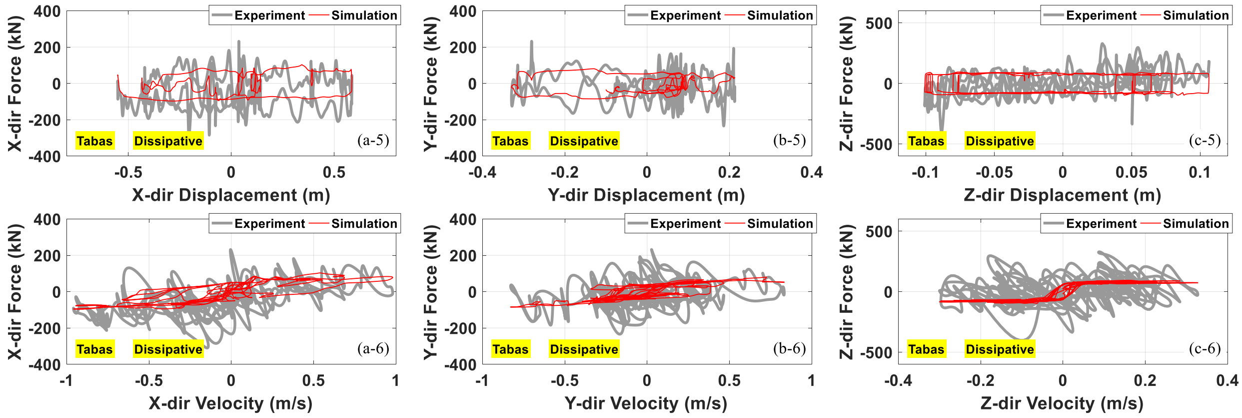

Figure 6.2 Tri-axial earthquake ground motion test Tabas: Comparison of numerically simulated and experimental results in frame {c} for the total actuator force components time histories (in sub-figures a-1, b-1, c-1), total actuator force components vs. corresponding platen displacement components (in sub-figures a-2, b-2, c-2), total actuator force components vs. platen corresponding platen velocity components (in sub-figures a-3, b-3, c-3), HDS restoring force components vs. corresponding platen displacement components (in sub-figures a-4, b-4, c-4), total dissipative force components vs. corresponding platen displacement components (in sub-figures a-5, b-5, c-5), and total dissipative force components vs. corresponding platen velocity component (in sub-figures a-6, b-6, c-6).

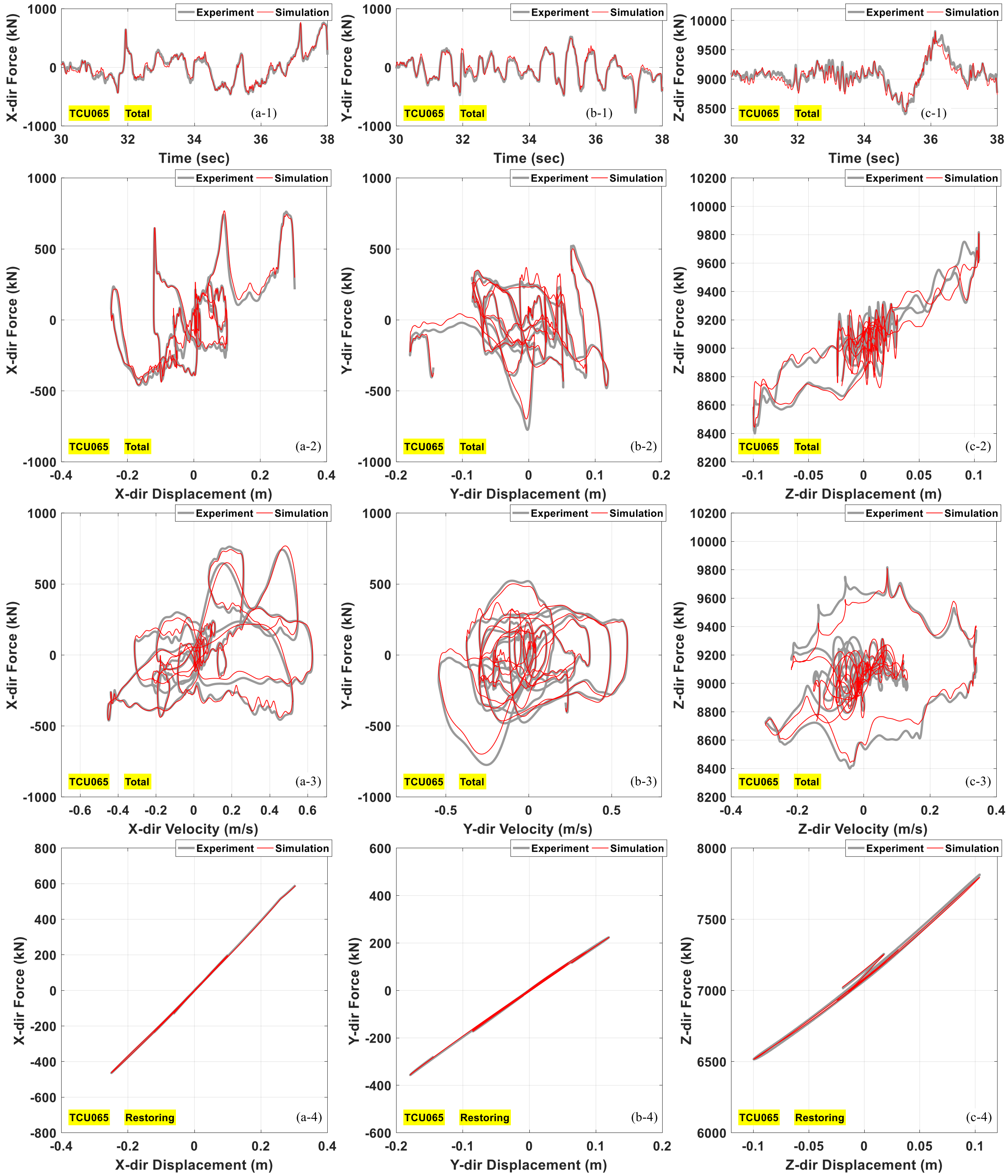

(Figure 6.3 is continued on next page)

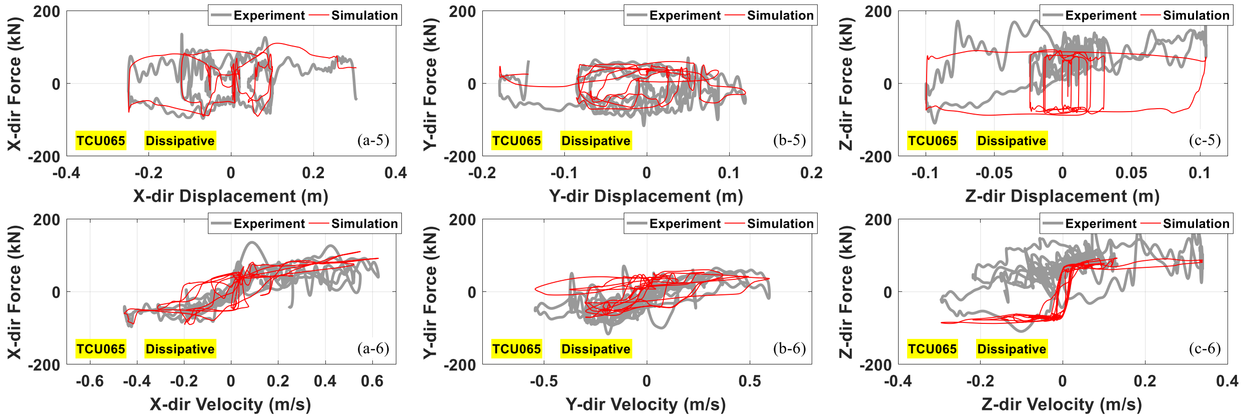

Figure 6.3 Tri-axial earthquake ground motion test TCU065: Comparison of numerically simulated and experimental results in frame {c} for the total actuator force component time histories (in sub-figures a-1, b-1, c-1), total actuator force components vs. corresponding platen displacement components (in sub-figures a-2, b-2, c-2), total actuator force components vs. platen corresponding platen velocity components (in sub-figures a-3, b-3, c-3), HDS restoring force components vs. corresponding platen displacement components (in sub-figures a-4, b-4, c-4), total dissipative force components vs. corresponding platen displacement components (in sub-figures a-5, b-5, c-5), and total dissipative force components vs. corresponding platen velocity components (in sub-figures a-6, b-6, c-6).

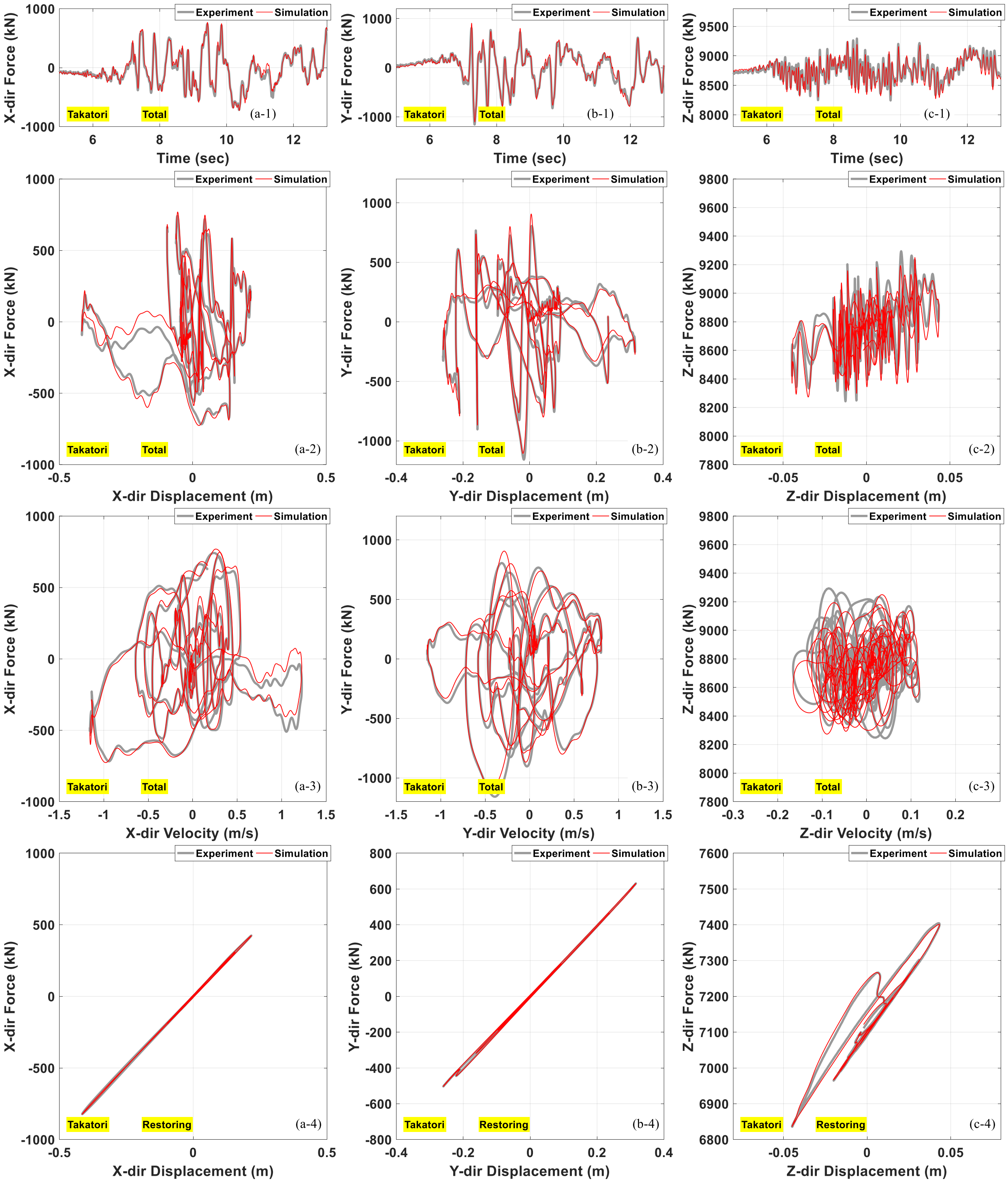

(Figure 6.4 is continued on next page)

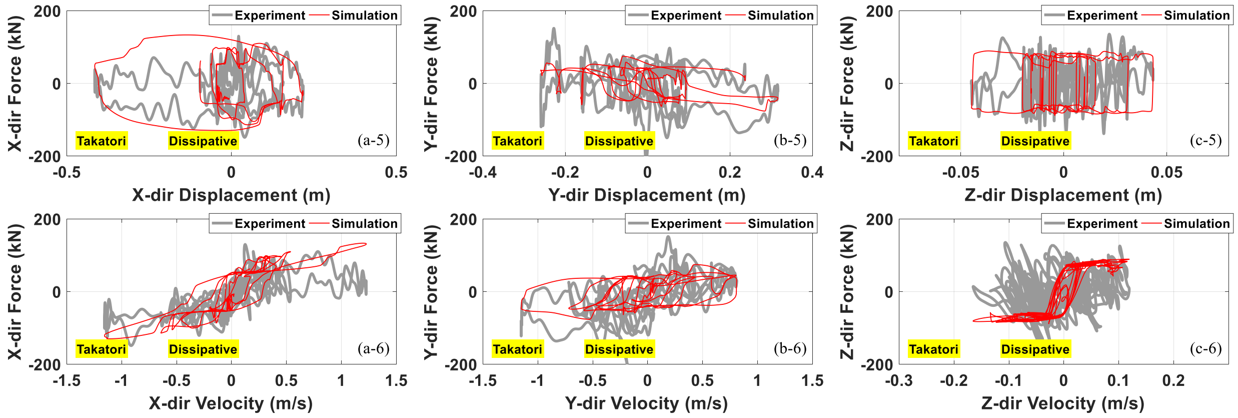

Figure 6.4 **Tri-axial earthquake ground motion test Takatori: Comparison of numerically simulated and experimental results in frame {c} for the total actuator force component time histories (in sub-figures a-1, b-1, c-1), total actuator force components vs. corresponding platen displacement components (in sub-figures a-2, b-2, c-2), total actuator force components vs. platen corresponding platen velocity components (in sub-figures a-3, b-3, c-3), HDS restoring force components vs. corresponding platen displacement components (in sub-figures a-4, b-4, c-4), total dissipative force components vs. corresponding platen displacement components (in sub-figures a-5, b-5, c-5), and total dissipative force components vs. corresponding platen velocity components (in sub-figures a-6, b-6, c-6).**

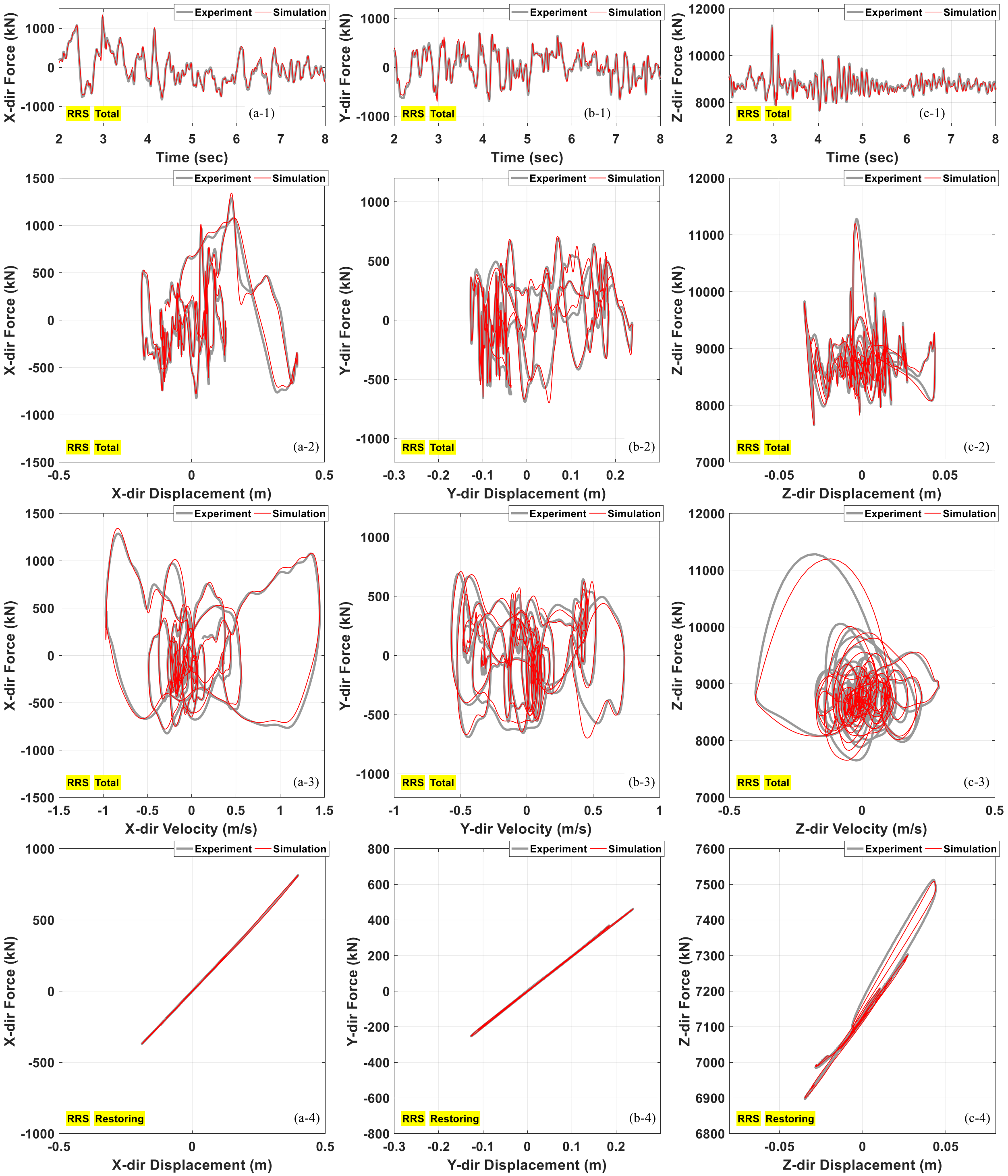

(Figure 6.5 is continued on next page)

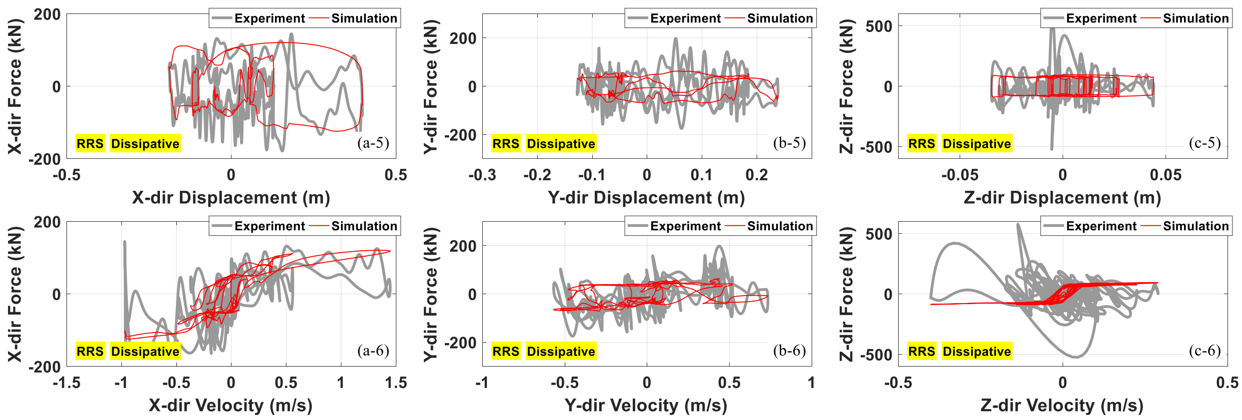

Figure 6.5 **Tri-axial earthquake ground motion test RRS: Comparison of numerically simulated and experimental results in frame {c} for the total actuator force component time histories (in sub-figures a-1, b-1, c-1), total actuator force components vs. corresponding platen displacement components (in sub-figures a-2, b-2, c-2), total actuator force components vs. corresponding platen velocity components (in sub-figures a-3, b-3, c-3), HDS restoring force components vs. corresponding platen displacement components (in sub-figures a-4, b-4, c-4), total dissipative force components vs. corresponding platen displacement components (in sub-figures a-5, b-5, c-5), and total dissipative force components vs. corresponding platen velocity components (in sub-figures a-6, b-6, c-6).**

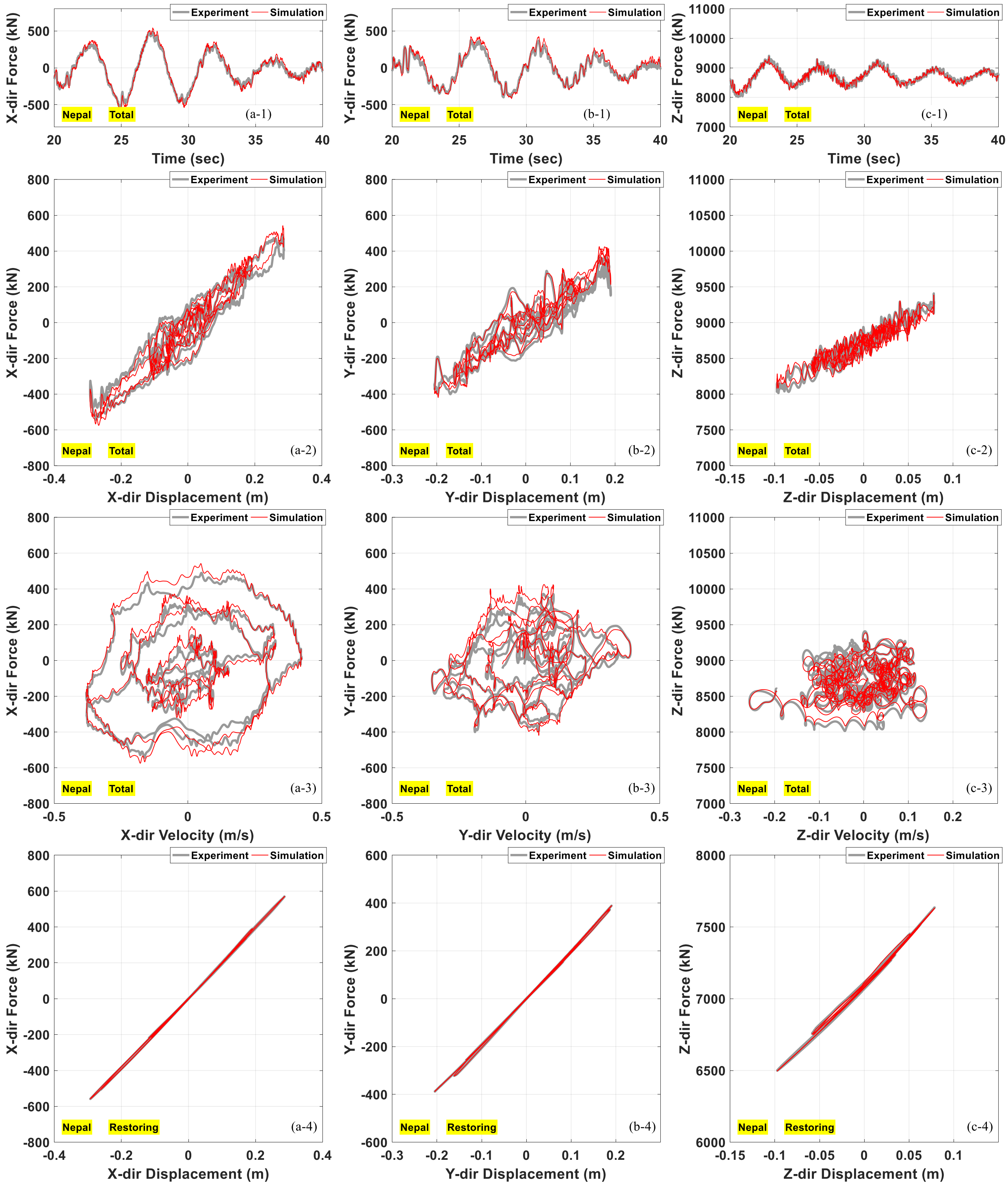

(Figure 6.6 is continued on next page)

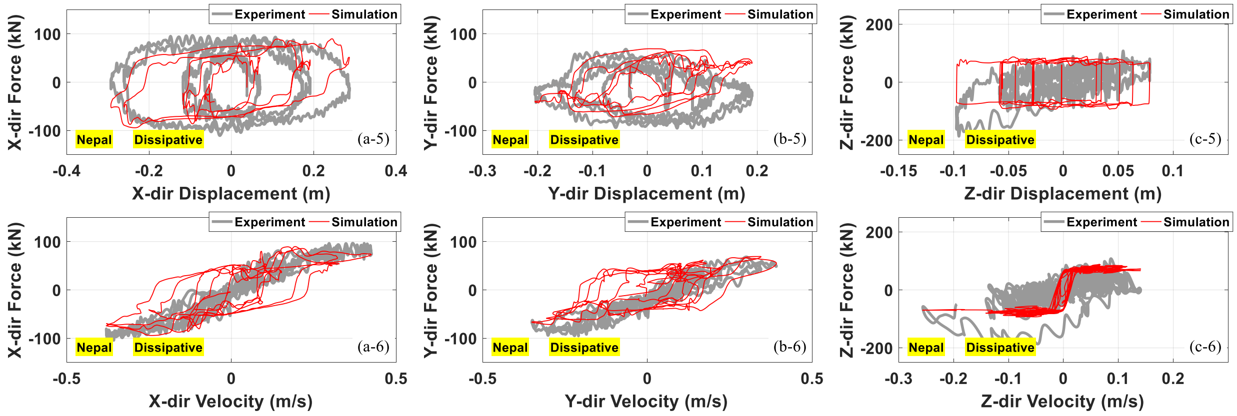

Figure 6.6 Tri-axial earthquake ground motion test Nepal: Comparison of numerically simulated and experimental results in frame {c} for the total actuator force component time histories (in sub-figures a-1, b-1, c-1), total actuator force components vs. corresponding platen displacement components (in sub-figures a-2, b-2, c-2), total actuator force components vs. corresponding platen velocity components (in sub-figures a-3, b-3, c-3), HDS restoring force components vs. corresponding platen displacement components (in sub-figures a-4, b-4, c-4), total dissipative force components vs. corresponding platen displacement components (in sub-figures a-5, b-5, c-5), and total dissipative force components vs. corresponding platen velocity components (in sub-figures a-6, b-6, c-6).

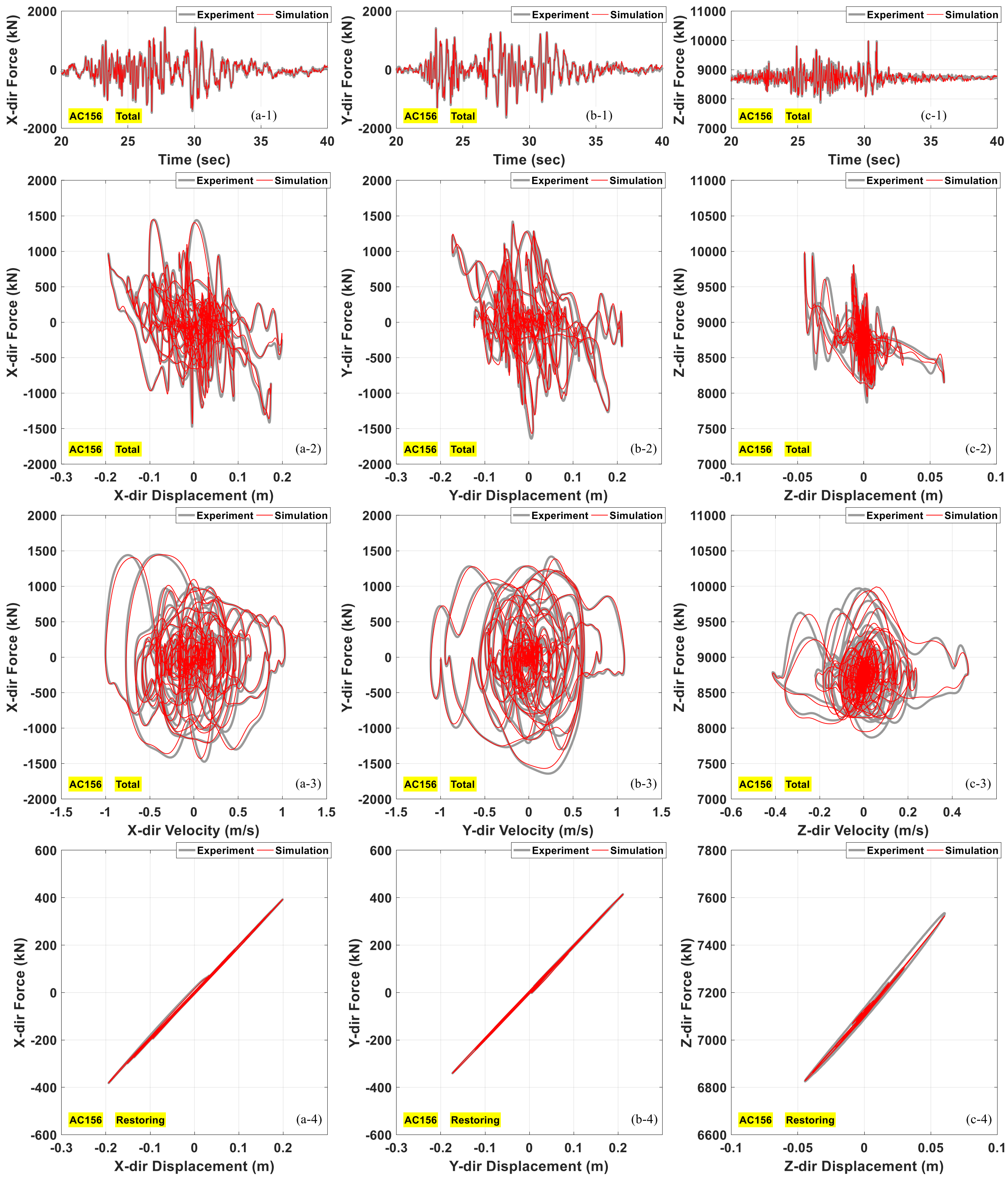

(Figure 6.7 is continued on next page)

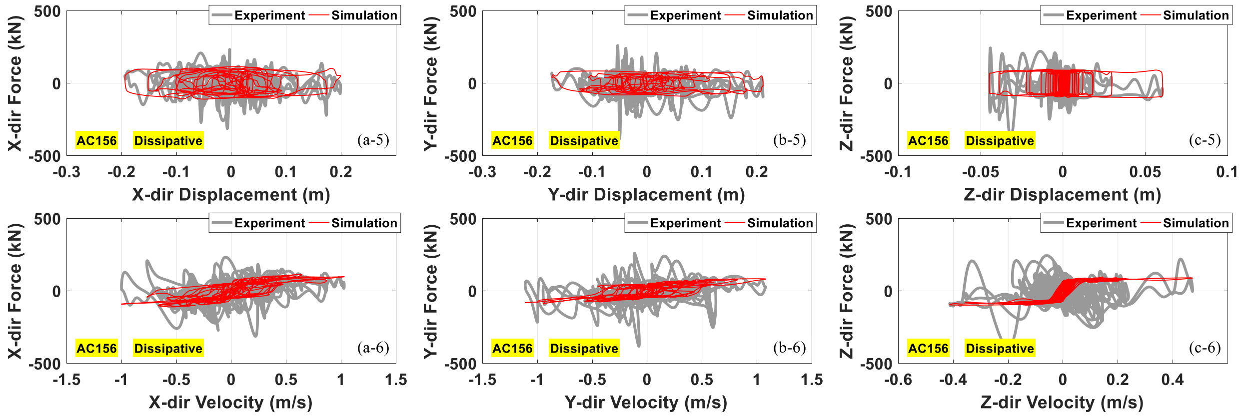

Figure 6.7 **Tri-axial earthquake ground motion test AC156: Comparison of numerically simulated and experimental results in frame {c} for the total actuator force component time histories (in sub-figures a-1, b-1, c-1), total actuator force components vs. corresponding platen displacement components (in sub-figures a-2, b-2, c-2), total actuator force components vs. corresponding platen velocity components (in sub-figures a-3, b-3, c-3), HDS restoring force components vs. corresponding platen displacement components (in sub-figures a-4, b-4, c-4), total dissipative force components vs. corresponding platen displacement components (in sub-figures a-5, b-5, c-5), and total dissipative force components vs. corresponding platen velocity components (in sub-figures a-6, b-6, c-6).**

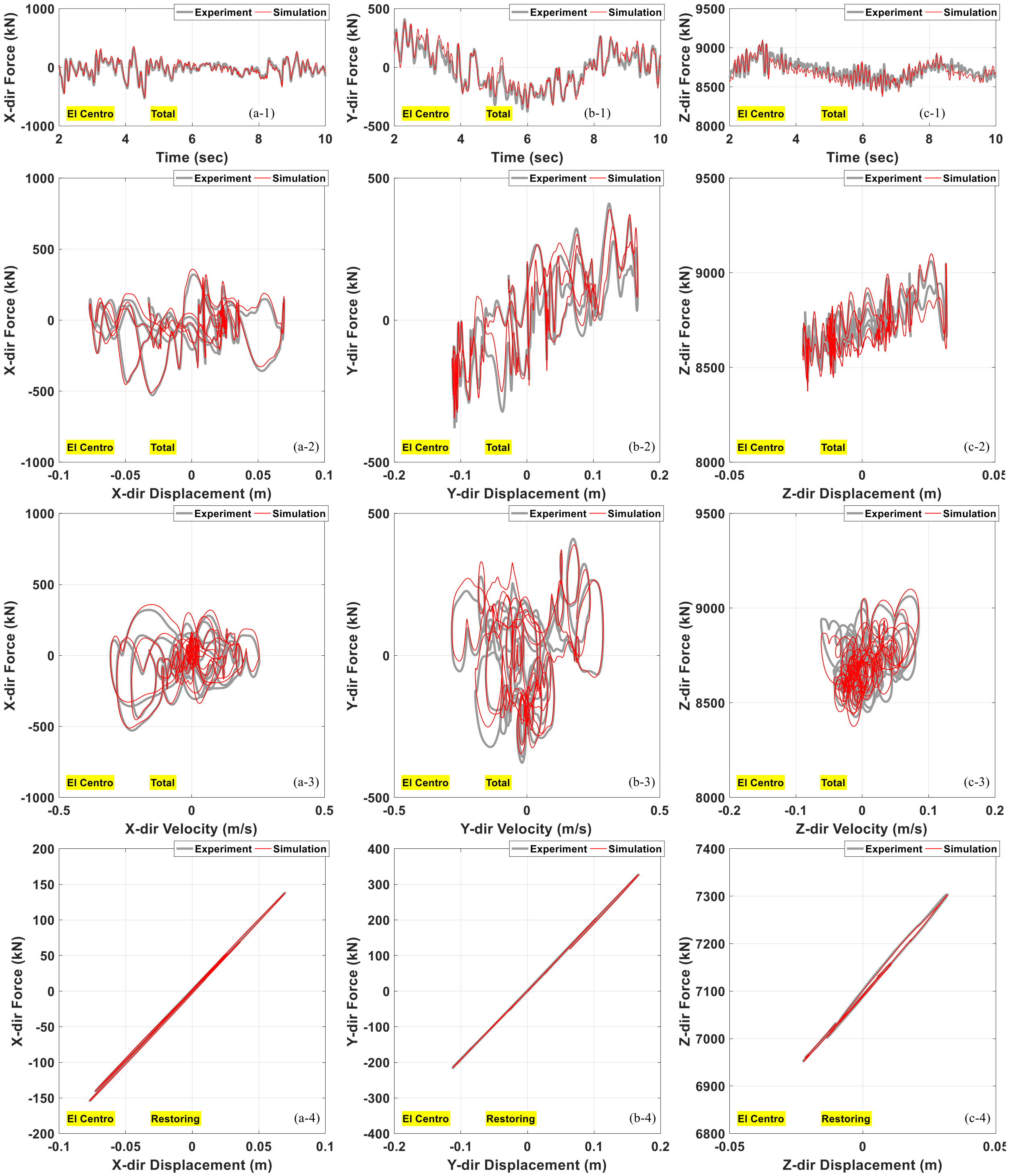

(Figure 6.8 is continued on next page)

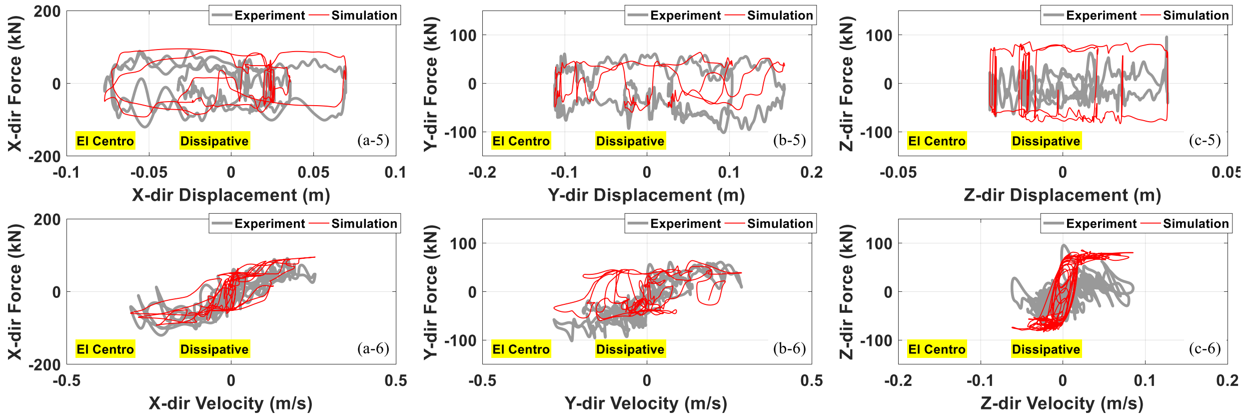

Figure 6.8 Tri-axial earthquake ground motion test El Centro: Comparison of numerically simulated and experimental results in frame {c} the total actuator force component time histories (in sub-figures a-1, b-1, c-1), total actuator force components vs. corresponding platen displacement components (in sub-figures a-2, b-2, c-2), total actuator force components vs. corresponding platen velocity components (in sub-figures a-3, b-3, c-3), HDS restoring force components vs. corresponding platen displacement components (in sub-figures a-4, b-4, c-4), total dissipative force components vs. corresponding platen displacement components (in sub-figures a-5, b-5, c-5), and total dissipative force components vs. corresponding platen velocity components (in sub-figures a-6, b-6, c-6).

6.2 COMPARISON OF NUMERICALLY SIMULATED AND EXPERIMENTAL OPEN-LOOP RESULTS

Only the hold-down strut dynamics subsystem and the kinematics and dynamics of the mechanical parts subsystem (as outlined in Chapter 5) are engaged in the numerical-experimental comparison study presented in Section 6.1, aimed at validating the corresponding sub-models and their associated parameter values. In this section, the recorded (feedback) displacements of the fourth-stage servovalve spools for all hydraulic actuators (both horizontal and vertical) in each shake table test considered here are applied as input to the open-loop version of the LHPOST6 numerical model to simulate the actuator forces (output of the hydraulic dynamics subsystem) and the resulting platen motion, including displacements, velocities, and accelerations, as depicted in Figure 6.19. Note that the simulated total actuator forces presented in this section differ from the simulation results shown in Section 6.1, where the inverse shake table dynamics was utilized without engaging the hydraulic dynamics subsystem. The numerical-experimental comparison study of the total actuator forces and achieved table motion also enables us to validate the parameter values of the hydraulic dynamics subsystem, given that the other parameters in the open-loop shake table model were previously validated in the preceding section.

Four tests are used in this section: (1) Test TX5 used in Section 6.1 (results shown in Figure 6.9), (2) Test SXH1 which consisted of a sinusoidal wave with a period of 2 sec and a displacement amplitude of 0.89 m in the X-direction (results shown in Figure 6.10), (3) seven tri-axial earthquake ground motion tests defined and used in Section 6.1 (results shown in Figure 6.11 through Figure 6.17), and (4) Test SFU (see Table 6.4) consisting of a six-degree-of-freedom synthetic earthquake displacement ground motion record (with both translational and rotational components) derived through elastodynamics for the 2004 Parkfield earthquake [Cao et al. 2018] recorded at the SFU station (results shown in Figure 6.18). A scaling factor of 1000 was applied to the rotational components of the SFU ground motion record to reach the order of magnitude of the rotational strokes of the LHPOST6. During Test SXH1, the peak table velocity in the X-direction (2.80 m/s) was near the velocity capacity of the LHPOST6 in the X direction (3.0 m/s, see Table 2.2). During Test SFU, the stroke capacity of one of the vertical actuators (5 in = 0.127 m) was reached when the Euler rotation angle about the X-axis (roll) was near 1.0 deg. These two tests allow for the evaluation of the predictive accuracy of the numerical model of the LHPOST6 under conditions close to the system's designed capacity.

Table 6.4 Characteristics of the six-axial synthetic earthquake ground motion test (SFU) conducted on the LHPOST6.

PGA (g)			**PGV (m/s)**			**PGD (m)**		
X	**Y**	**Z**	**X**	**Y**	**Z**	**X**	**Y**	**Z**
0.017	0.025	0.009	0.072	0.13	0.042	0.109	0.137	0.023
PGA (deg/s^2)			**PGV (deg/s)**			**PGD (deg)**		
RX	**RY**	**RZ**	**RX**	**RY**	**RZ**	**RX**	**RY**	**RZ**
4.836	3.57	6.238	1.949	1.654	1.91	1.119	0.886	1.184

Figure 6.9 through Figure 6.18 compare the experimental and numerically simulated platen motions (displacement(s), velocity(ies), and acceleration(s) in the first, second, and third column of each figure, respectively) and total hydraulic actuator force (in the fourth column) for each degree of freedom. These results show that the open-loop numerical model captures the dynamic characteristic of the LHPOST6 effectively. However, small discrepancies between the numerical and experimental results can be observed: (1) small, gradually increasing drifts in the platen displacement and small, constant offsets in the actuator force simulation results during earthquake tests, and (2) stronger oil column resonance effects in the platen acceleration simulation results for the six-axial earthquake test. The displacement drifts are most likely due to the cumulative error generated during the integration of platen velocity over time in the absence of table motion control in the context of the open-loop simulation presented in this section. Concerning the force offsets, it is noted that they manifest solely in the vertical forces and moments about the X and Y directions. This observation suggests potential physical distinctions between the effective inertial and gravity masses – assumed equal in the numerical model of the LHPOST6 – of the moving parts of the components attached to the shake table platen. The stronger oil column resonance effects in the simulation results are most likely due to the hydraulic fluid leaking across actuator piston seals, which is more significant than expected.

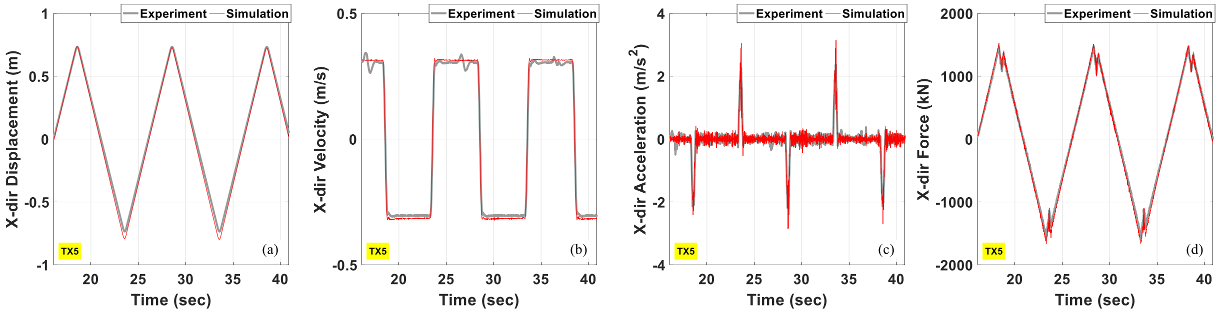

Figure 6.9 Comparison of open-loop numerically simulated and experimental results for triangular wave test TX5: time histories of (a) platen displacement, (b) platen velocity, (c) platen acceleration, and (d) total hydraulic actuator force in the X-direction expressed in frame {c}.

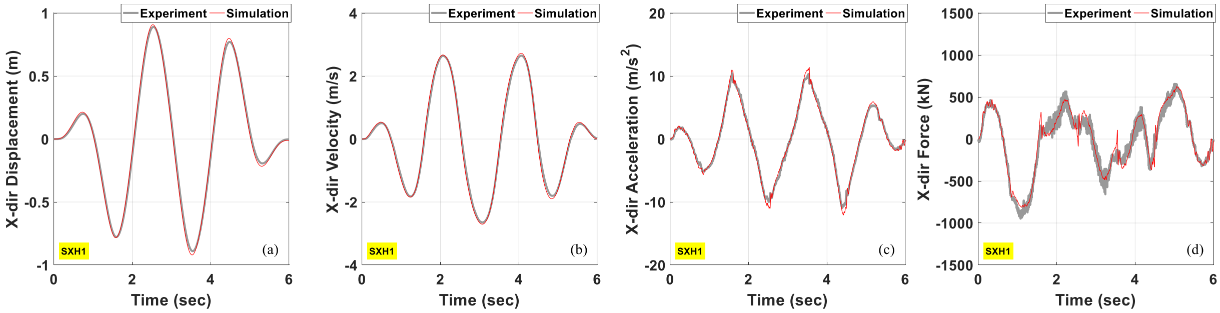

Figure 6.10 Comparison of open-loop numerically simulated and experimental results for sinusoidal wave test SXH1: time histories of (a) platen displacement, (b) platen velocity, (c) platen acceleration, and (d) total hydraulic actuator force in the X-direction expressed in frame {c}.

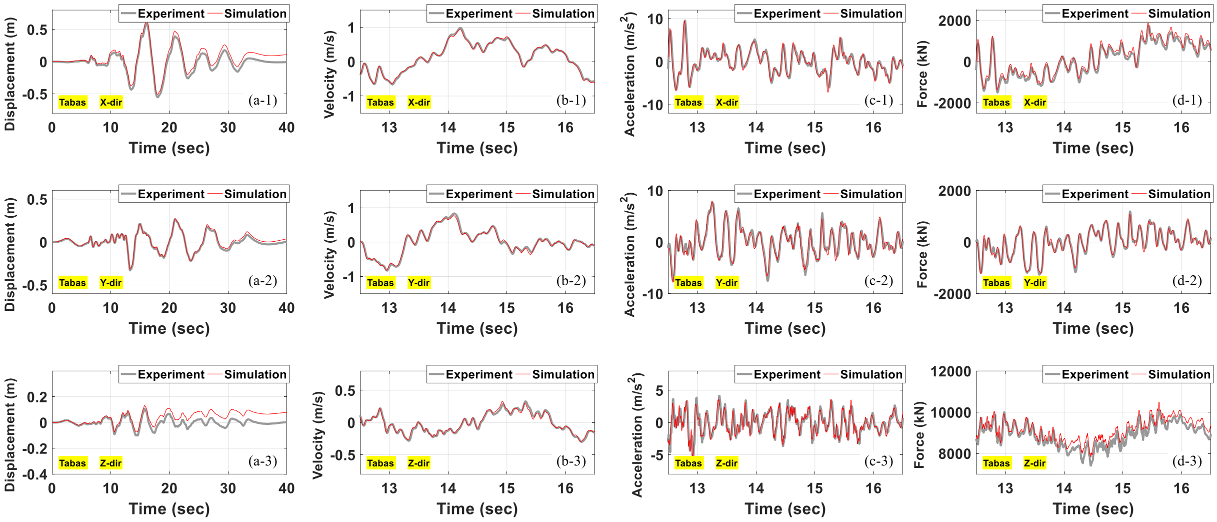

Figure 6.11 Comparison of open-loop numerically simulated and experimental results for tri-axial earthquake ground motion test Tabas: time histories of platen displacement components (sub-figures a-1 through a-3), platen velocity components (sub-figures b-1 through b-3), platen acceleration components (sub-figures c-1 through c-3), and total hydraulic actuator force components (sub-figures d-1 through d-3) expressed in frame {c}.

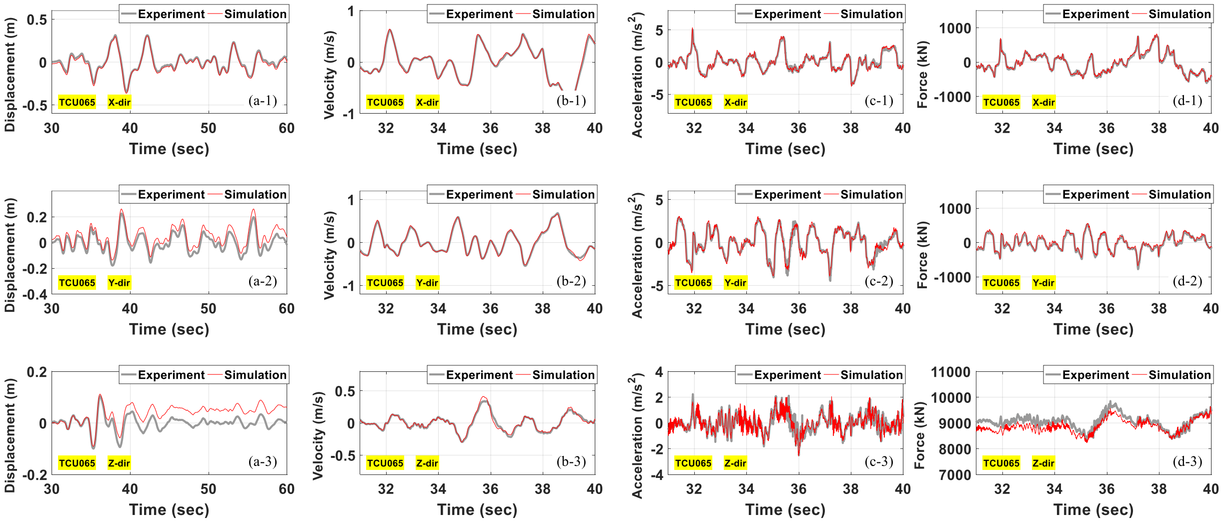

Figure 6.12 Comparison of open-loop numerically simulated and experimental results for tri-axial earthquake ground motion test TCU065: time histories of platen displacement components (sub-figures a-1 through a-3), platen velocity components (sub-figures b-1 through b-3), platen acceleration components (sub-figures c-1 through c-3), and total hydraulic actuator force components (sub-figures d-1 through d-3) expressed in frame {c}.

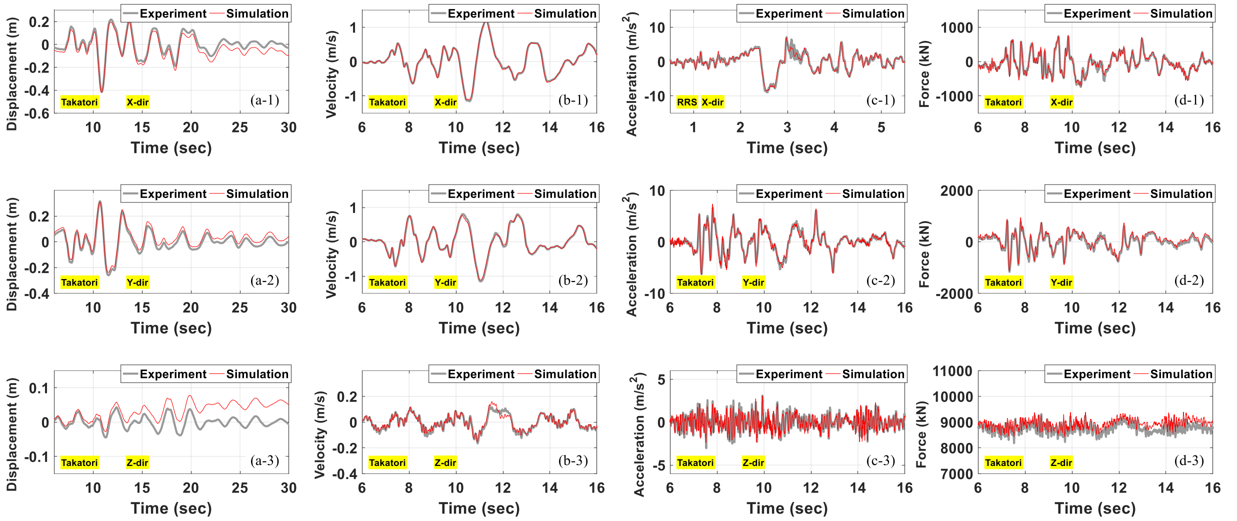

Figure 6.13 **Comparison of open-loop numerically simulated and experimental results for tri-axial earthquake ground motion test Takatori: time histories of platen displacement components (sub-figures a-1 through a-3), platen velocity components (sub-figures b-1 through b-3), platen acceleration components (sub-figures c-1 through c-3), and total hydraulic actuator force components (sub-figures d-1 through d-3) expressed in frame {c}.**

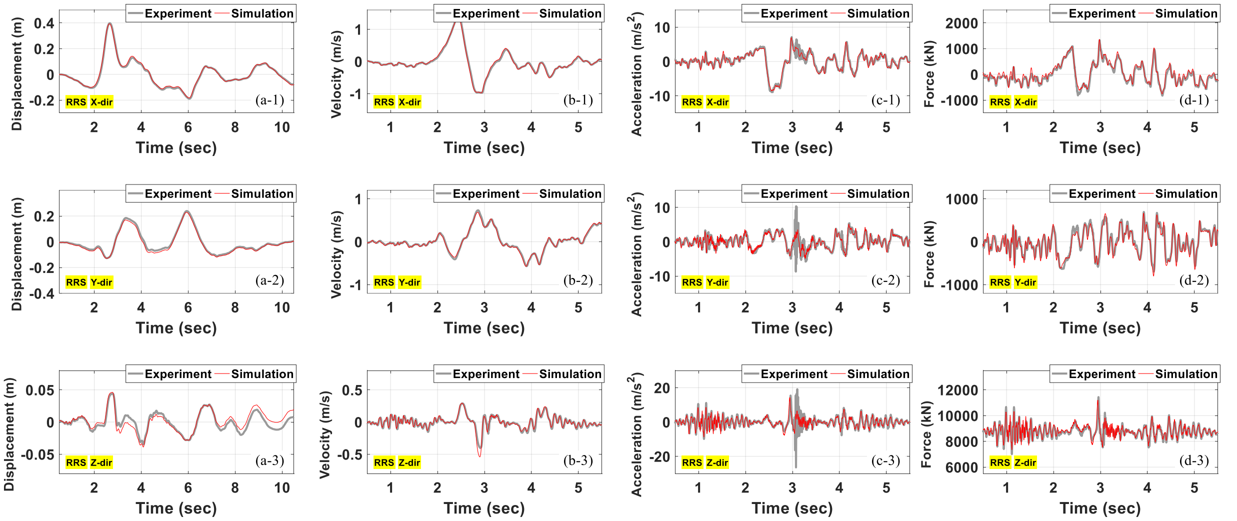

Figure 6.14 **Comparison of open-loop numerically simulated and experimental results for tri-axial earthquake ground motion test RRS: time histories of platen displacement components (sub-figures a-1 through a-3), platen velocity components (sub-figures b-1 through b-3), platen acceleration components (sub-figures c-1 through c-3), and total hydraulic actuator force components (sub-figures d-1 through d-3) expressed in frame {c}.**

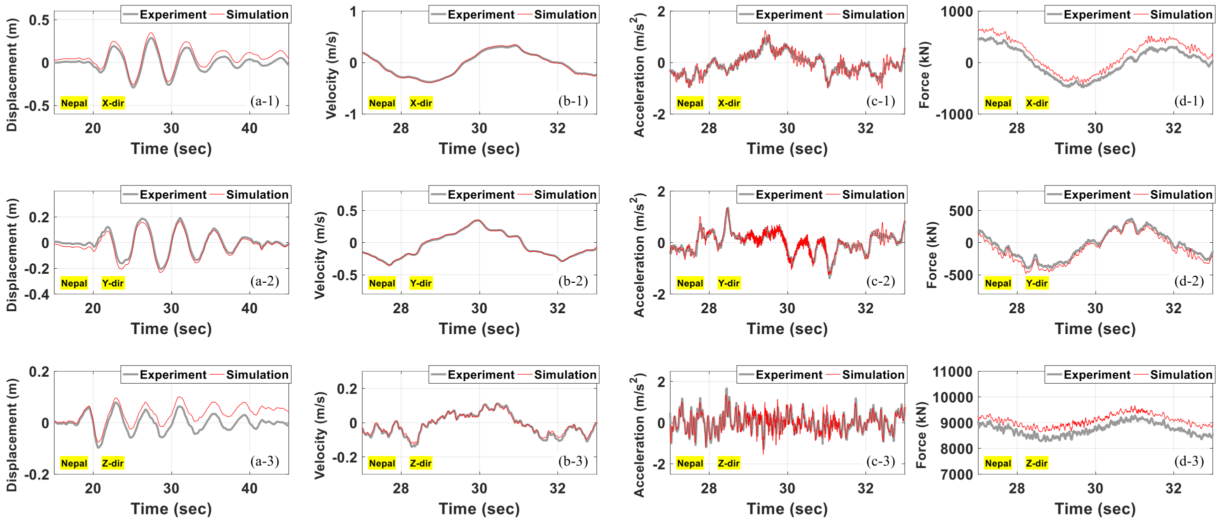

Figure 6.15 Comparison of open-loop numerically simulated and experimental results for tri-axial earthquake ground motion test Nepal: time histories of platen displacement components (sub-figures a-1 through a-3), platen velocity components (sub-figures b-1 through b-3), platen acceleration components (sub-figures c-1 through c-3), and total hydraulic actuator force components (sub-figures d-1 through d-3) expressed in frame {c}.

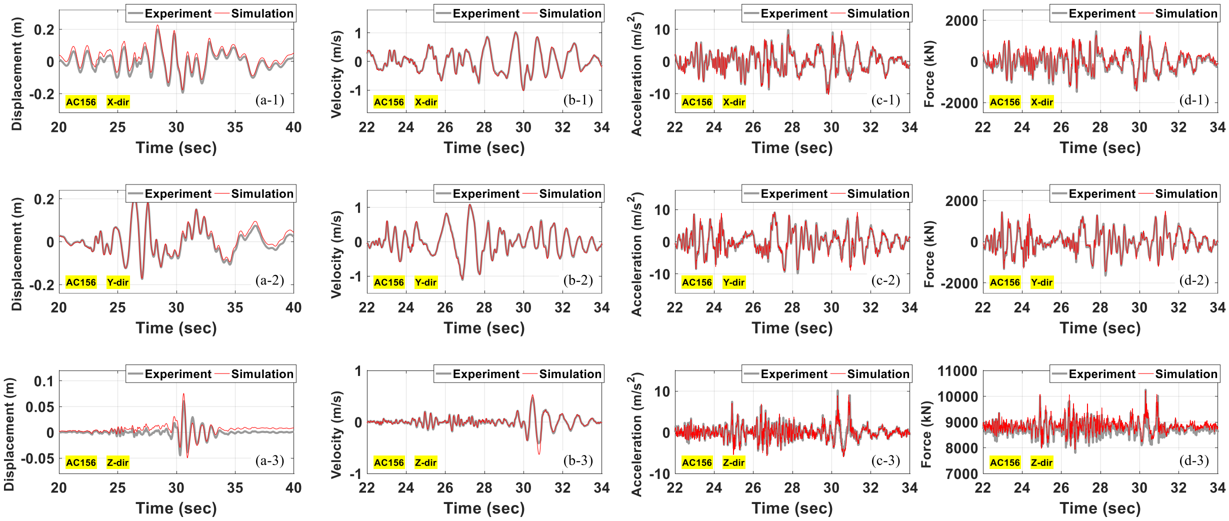

Figure 6.16 Comparison of open-loop numerically simulated and experimental results for tri-axial earthquake ground motion test AC156: time histories of platen displacement components (sub-figures a-1 through a-3), platen velocity components (sub-figures b-1 through b-3), platen acceleration components (sub-figures c-1 through c-3), and total hydraulic actuator force components (sub-figures d-1 through d-3) expressed in frame {c}.

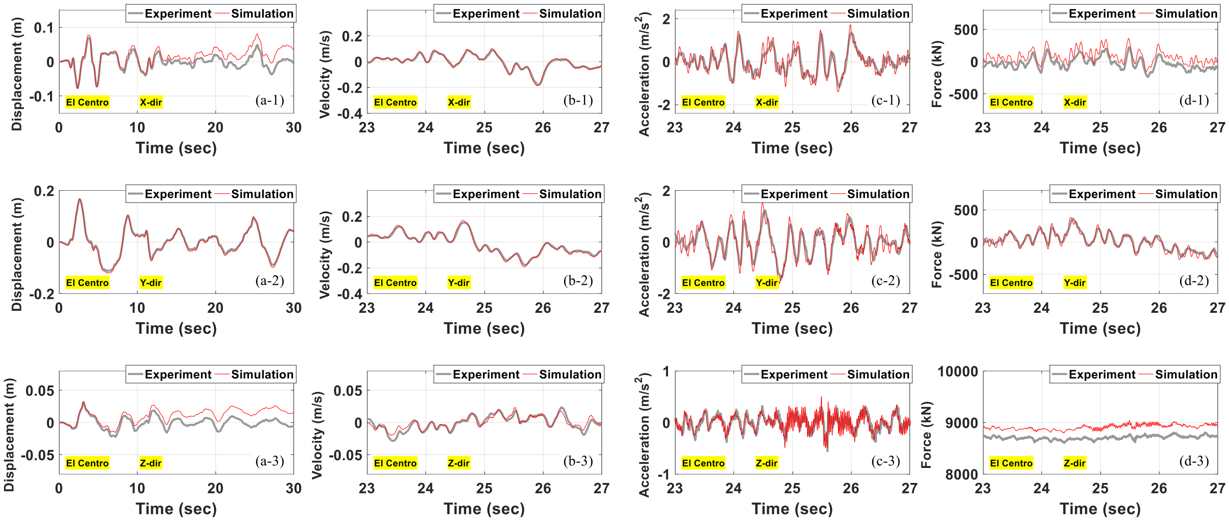

Figure 6.17 Comparison of open-loop numerically simulated and experimental results for tri-axial earthquake ground motion test El Centro: time histories of platen displacement components (sub-figures a-1 through a-3), platen velocity components (sub-figures b-1 through b-3), platen acceleration components (sub-figures c-1 through c-3), and total hydraulic actuator force components (sub-figures d-1 through d-3) expressed in frame {c}.

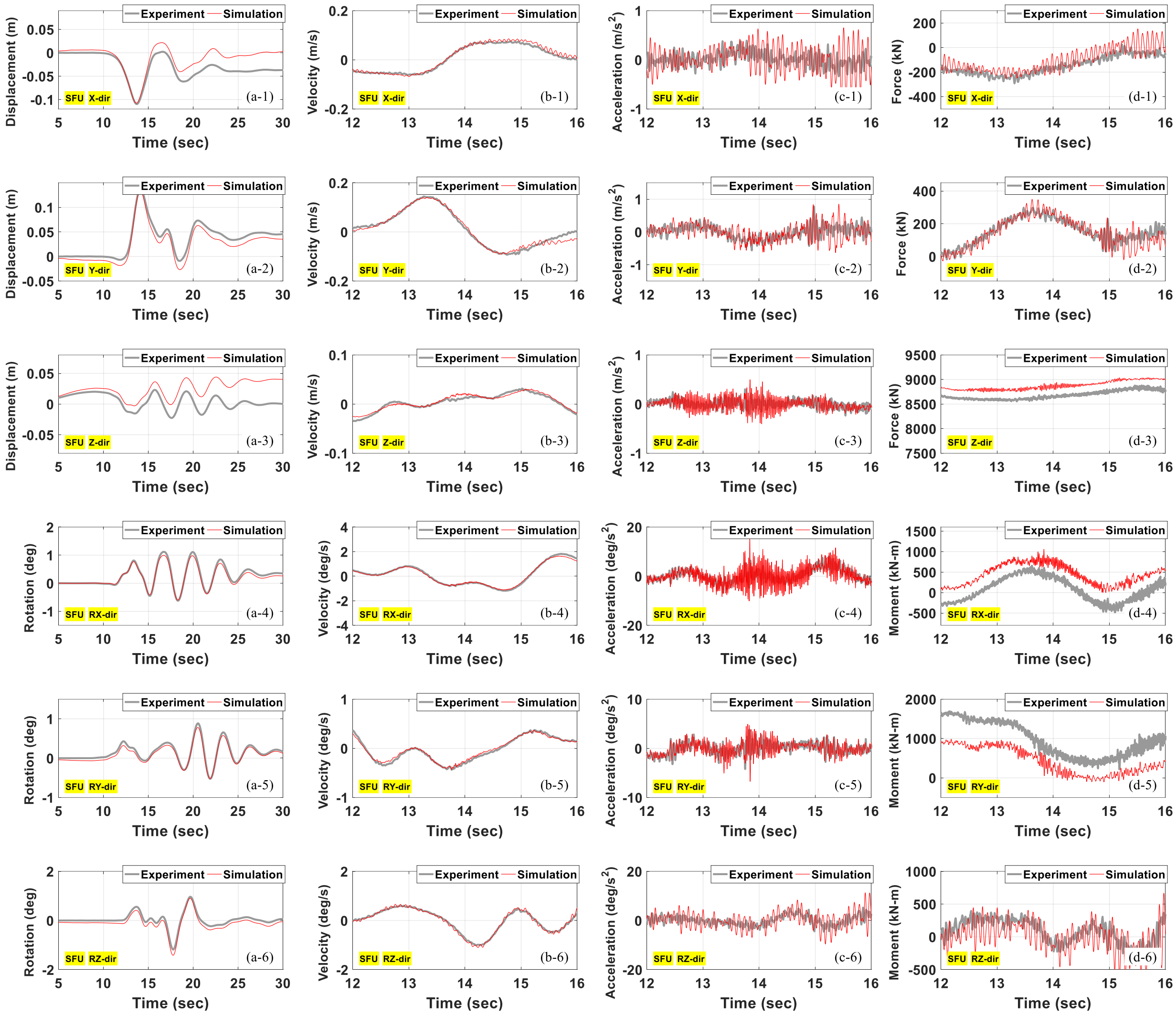

Figure 6.18 Comparison of open-loop numerically simulated and experimental results for the synthetic six-axial earthquake ground motion test SFU: time histories of platen displacement components (sub-figures a-1 through a-6), platen velocity components (sub-figures b-1 through b-6), platen acceleration components (sub-figures c-1 through c-6), and total hydraulic actuator force and moment components (sub-figures d-1 through d-6) expressed in frame {c}.

6.3 COMPARISON OF NUMERICALLY SIMULATED AND EXPERIMENTAL CLOSED-LOOP RESULTS

The closed-loop behavior of the LHPOST6 is studied in this section by integrating the MTS 469D controller (see Figure 5.1) and the open-loop LHPOST6 model (see Figure 5.2) in a closed control loop, as depicted in Figure 6.19. In other words, the 469D controller is integrated with the open-loop LHPOST6 numerical model in a closed control feedback loop. When conducting earthquake shake table tests, each test is iterated several times to derive the optimum drive signal (modified reference ground motion record) that minimizes the relative root mean square error between the measured (or achieved) platen motion and the original reference earthquake ground motion record. Repeating this earthquake test at a later time involves simply replaying the last or optimal drive signal, which serves as the input signal into the reference generator module of the 469D, as depicted in Figure 5.1. In the closed-loop simulation setup (see Figure 6.19), the open-loop numerical model of the LHPOST6 in Simulink interacts with the 469D controller via the UDP communication protocol. Two sets of signals are transferred between the 469D and Simulink: (1) the fourth-stage servovalve commands sent from the 469D to Simulink, and (2) the platen acceleration responses (computed at the feedback accelerometer locations), actuator displacements, and actuator forces transmitted from Simulink to the 469D. As per the TVC loop depicted in the 469D (see Figure 5.1), a control loop is designated for each of the 6 Cartesian DOFs of the LHPOST6. The 6-DOF TVC output is subsequently transformed into the 10 actuator (4 horizontal and 6 vertical) DOFs utilizing inverse kinematics (see Equations (3-31) and (3-33)). These transformed values represent the fourth-stage servovalve displacement command for each of the fourteen servovalves. Specifically, each horizontal actuator is ported by two servovalves, while each vertical is ported by one servovalve. Within the nested inner control loop of the four-stage servovalve spool displacement (see Figure **6.20**), the fourth-stage servovalve displacement command is converted into an analog electric current, measured in Amperes (Amps). This electric signal physically feeds into the electromagnetic flapper assembly in the first stage of the servovalve (see Figure **6.20**). The fourth-stage servovalve inner loop is simplified into a pure time delay, which is justified by measurement data corresponding to the fourth-stage spool displacement command and feedback signals depicted in Figure 6.21. During the earthquake shake table tests, the optimal drive signal and corresponding 469D controller settings (including feedforward and feedback gains) were meticulously documented and stored. These settings were directly applied without alteration (verbatum) to the 469D in the closed-loop numerical simulation of the LHPOST6.

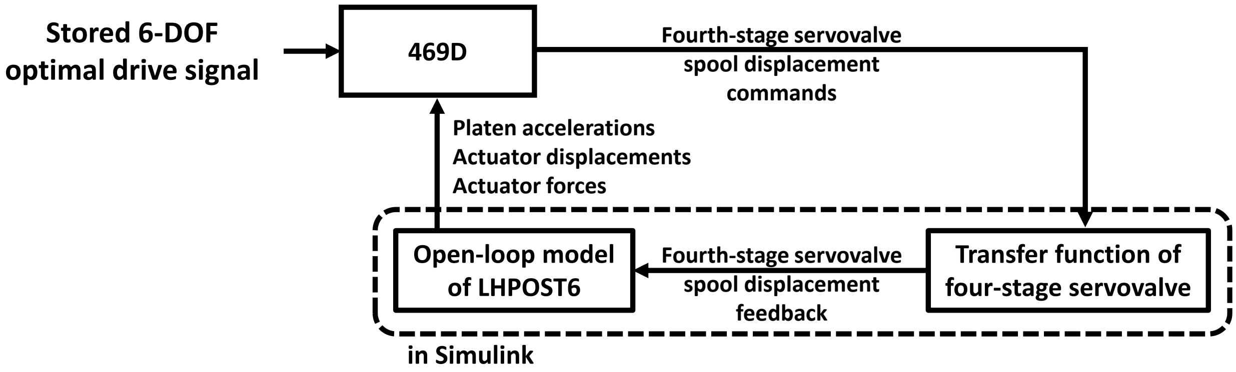

Figure 6.19 Block diagram of the closed-loop simulation (469D controller + open-loop LHPOST6 model); see Figure 5.1 for MTS 469D digital controller.

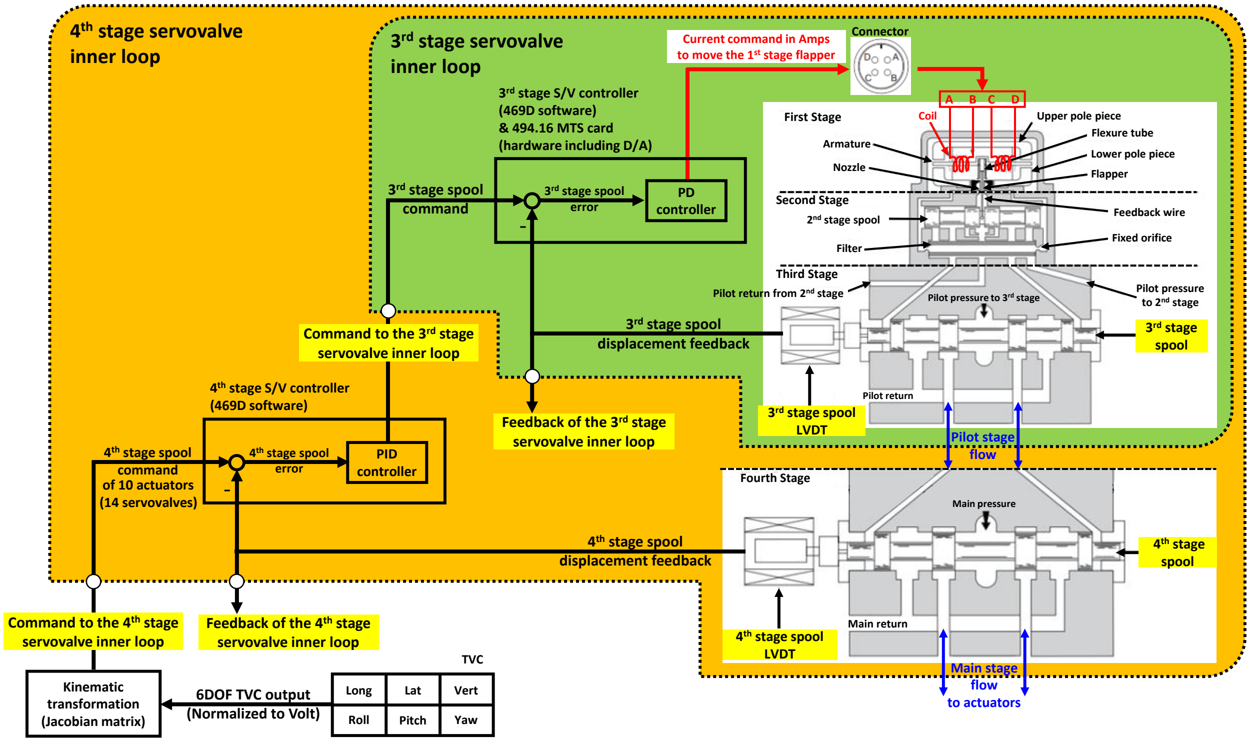

Figure 6.20 Block diagram of four-stage hydraulic servovalve with inner control loops.

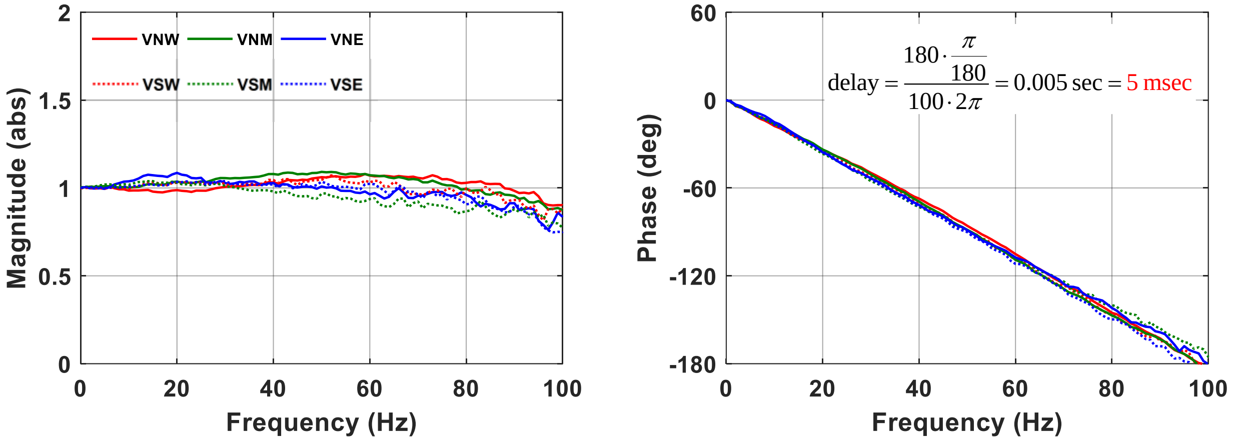

Figure 6.21 Experimental transfer functions between the measured servovalve fourth-stage spool displacement command and feedback signals (illustrated here for the six vertical actuators) and calculation of the four-stage servovalve time delay.

Next, comparisons between the closed-loop numerical simulation and experimental results are provided for seven tri-axial earthquake ground motion tests and one six-axial earthquake test as defined and utilized in Section 6.1. These comparisons are depicted in Figure 6.22 through Figure 6.35 for the tri-axial earthquake tests and in Figure 6.36 and Figure 6.37 for the six-axial earthquake test. Both numerical and experiment results are juxtaposed, not only for the platen motion (which is the primary concern of the user regarding the response of the closed-loop shake table system) but also for the fourth-stage servovalve commands. This comprehensive comparison of intermediate control signals within the closed-loop system enables a more thorough evaluation of the numerical model of the LHPOST6. Figure 6.22 (Test Tabas), Figure 6.24 (Test TCU065), Figure 6.26 (Test Takatori), Figure 6.28 (Test RRS), Figure 6.30 (Test Nepal), Figure 6.32 (Test AC156) and Figure 6.34 (Test El Centro) show the displacement, velocity and acceleration responses of the platen (at the center of its top surface). Additionally, these figures provide the corresponding relative root mean square errors (RRMSE′s) between simulated and experimental results. Similar comparative results are shown in Figure 6.34 for the displacement and rotational response components of the platen in the case of the six-axial earthquake test (Test SFU). The time delays between the reference (desired) earthquake motion and achieved/feedback table motion for both the physical and numerical LHPOST6 are in the range of 25 to 30 msec, with a few msec of difference between the experimental and numerical time delays. This disparity in time delays is corrected for before plotting (for comparison purposes) the experimental and numerical time history results and computing the relative roor mean square errors (RRMSEs). Figure 6.23 (Test Tabas), Figure 6.25 (Test TCU065), Figure 6.27 (Test Takatori), Figure 6.29 (Test RRS), Figure 6.31 (Test Nepal), Figure 6.33 (Test AC156) and Figure 6.35 (Test El Centro) and Figure 6.37 compare the fourth-stage servovalve command time histories from the physical and numerical LHPOST6 for each of the 4 horizontal actuators and six vertical actuators. It is important to note that for the seven tri-axial and one six-axial earthquake tests considered here, only one servovalve (servovalve A) of each of the four horizontal actuators of the physical (and therefore of the numerical) LHPOST6 was enabled. The comparative results in Figure 6.22 through Figure 6.37 show that the numerical simulation results are in close agreement with the experimental results, which represent the ground truth. This indicates that the numerical model of the LHPOST6 presented in this report (open-loop numerical model of the LHPOST6 closed with the 469D controller) accurately represents (i.e., is an accurate digital twin of) the actual LHPOST6. Note that the 469D TVC loop effectively eliminates the gradual platen displacement drifts observed in the open-loop simulation results (see Figure 6.11 through Figure 6.18). This capability stems from the inclusion of a displacement feedback control loop within the TVC.

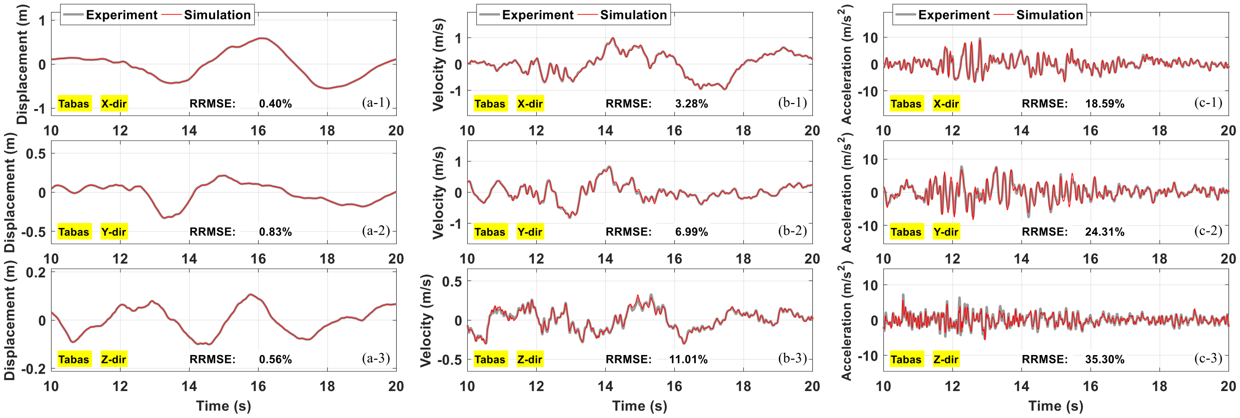

Figure 6.22 Comparison of closed-loop numerically simulated and experimental platen motion results for the tri-axial earthquake ground motion test Tabas: time histories of platen displacement components (sub-figures a-1 through a-3), platen velocity components (sub-figures b-1 through b-3) and platen acceleration components (sub-figures c-1 through c-3).

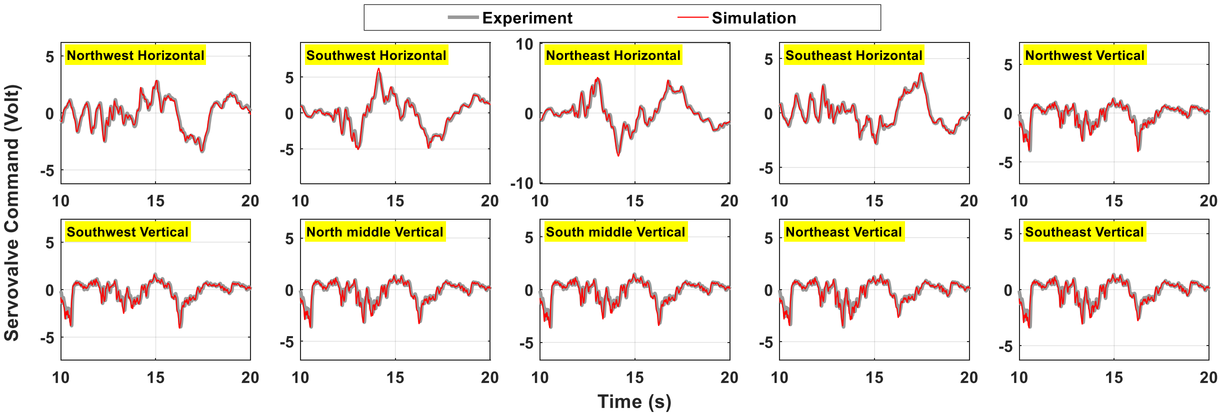

Figure 6.23 Comparison of closed-loop numerically simulated and experimental fourth-stage servovalve command time histories for each of the four horizontal and six vertical actuators in the case of the tri-axial earthquake ground motion test Tabas.

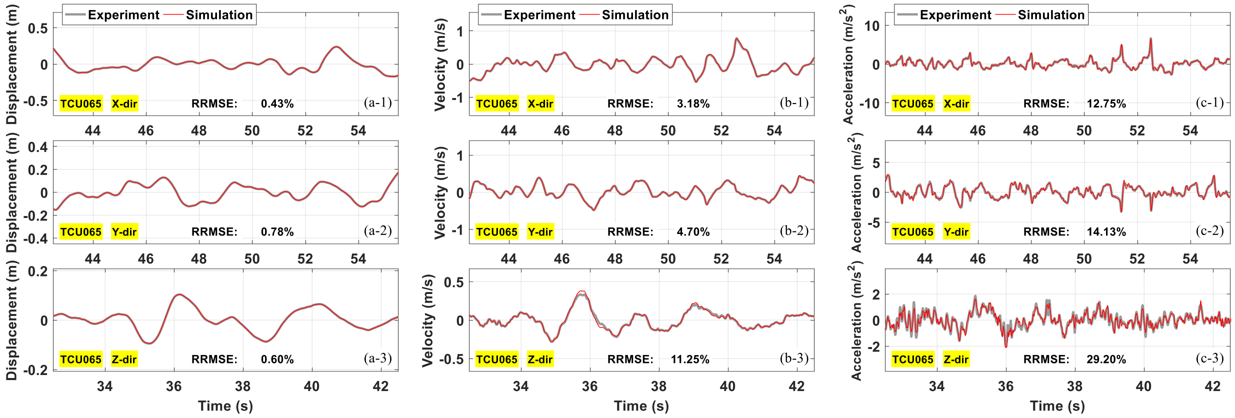

Figure 6.24 Comparison of closed-loop numerically simulated and experimental platen motion results for the tri-axial earthquake ground motion test TCU065: time histories of platen displacement components (sub-figures a-1 through a-3), platen velocity components (sub-figures b-1 through b-3) and platen acceleration components (sub-figures c-1 through c-3).

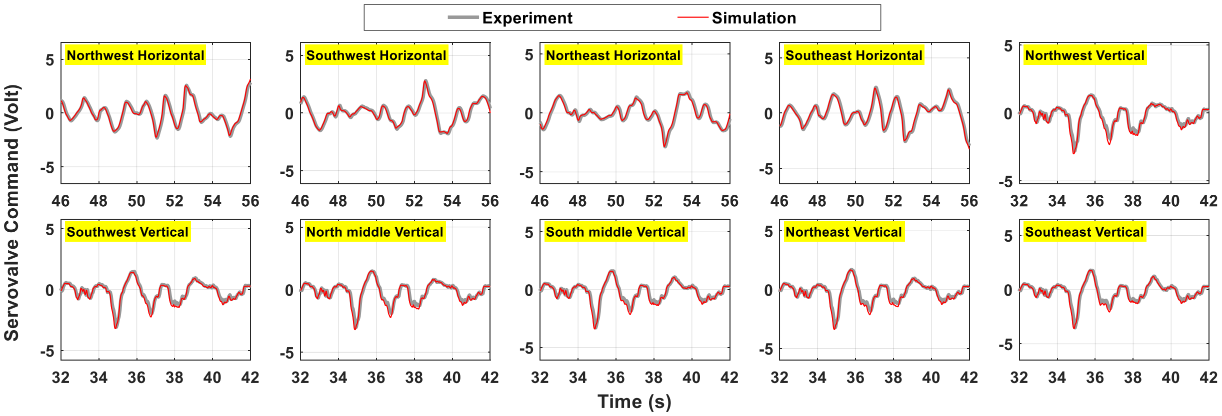

Figure 6.25 Comparison of closed-loop numerically simulated and experimental fourth-stage servovalve command time histories for each of the four horizontal and six vertical actuators in the case of the tri-axial earthquake ground motion test TCU065.

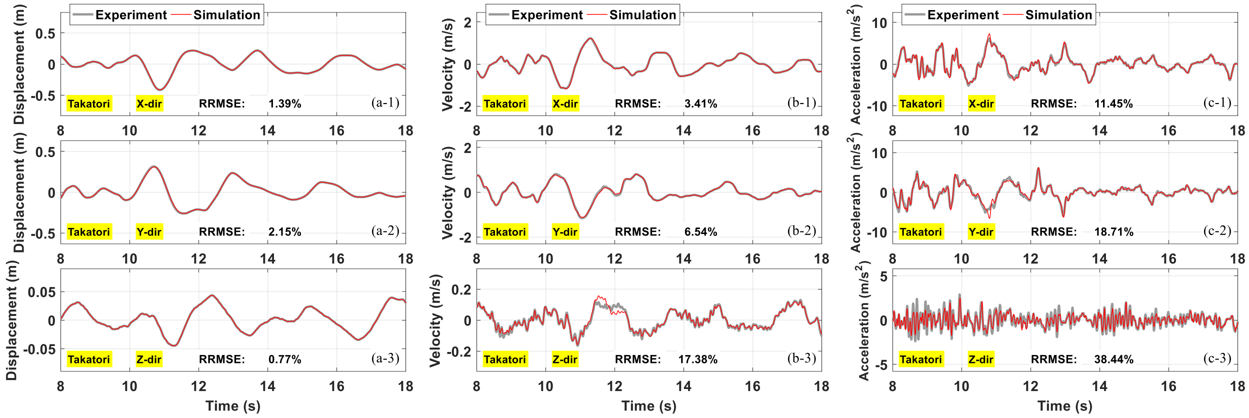

Figure 6.26 Comparison of closed-loop numerically simulated and experimental platen motion results for the tri-axial earthquake ground motion test Takatori: time histories of platen displacement components (sub-figures a-1 through a-3), platen velocity components (sub-figures b-1 through b-3) and platen acceleration components (sub-figures c-1 through c-3).

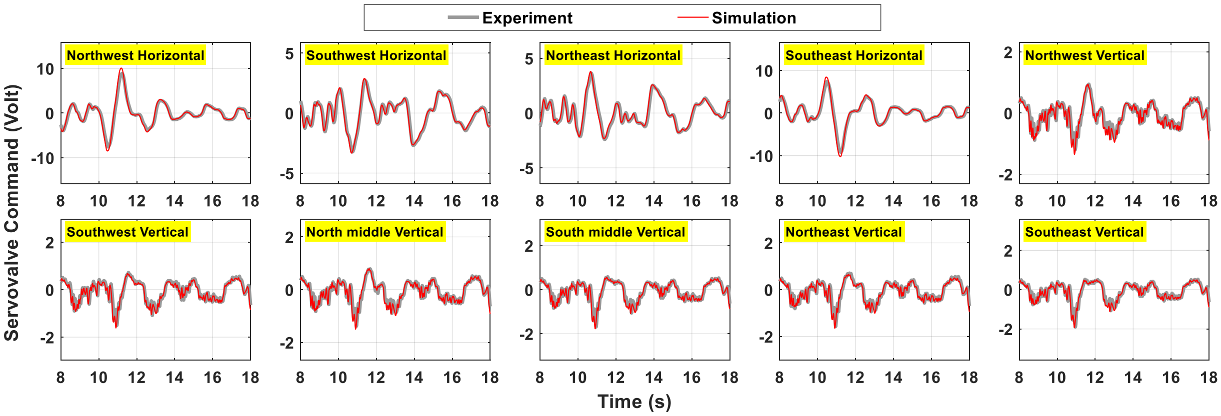

Figure 6.27 Comparison of closed-loop numerically simulated and experimental fourth-stage servovalve command time histories for each of the four horizontal and six vertical actuators in the case of the tri-axial earthquake ground motion test Takatori.

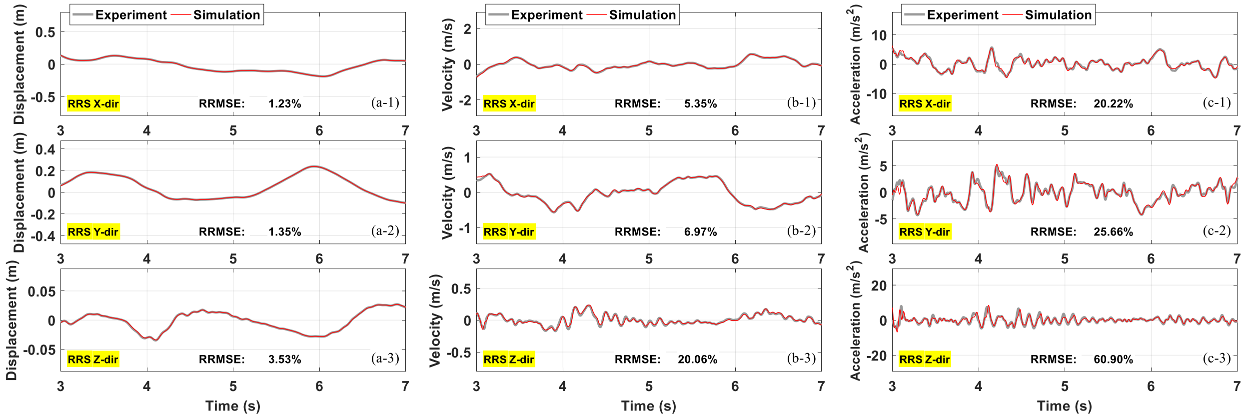

Figure 6.28 Comparison of closed-loop numerically simulated and experimental platen motion results for the tri-axial earthquake ground motion test RRS: time histories of platen displacement components (sub-figures a-1 through a-3), platen velocity components (sub-figures b-1 through b-3) and platen acceleration components (sub-figures c-1 through c-3).

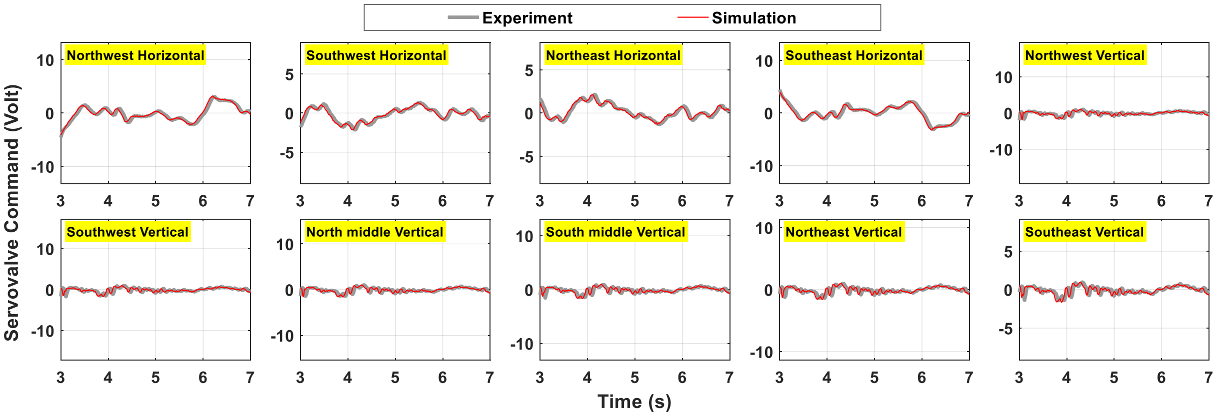

Figure 6.29 Comparison of closed-loop numerically simulated and experimental fourth-stage servovalve command time histories for each of the four horizontal and six vertical actuators in the case of the tri-axial earthquake ground motion test RRS.

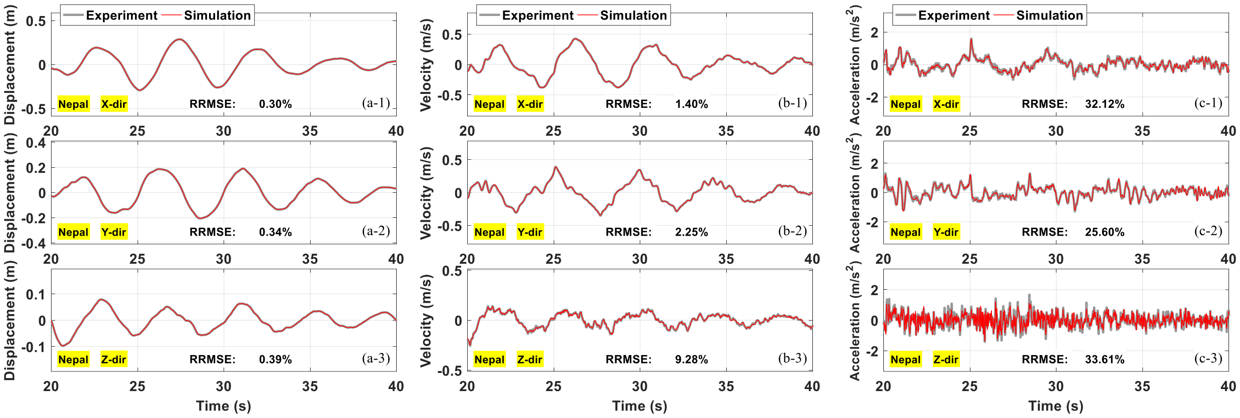

Figure 6.30 Comparison of closed-loop numerically simulated and experimental platen motion results for the tri-axial earthquake ground motion test Nepal: time histories of platen displacement components (sub-figures a-1 through a-3), platen velocity components (sub-figures b-1 through b-3) and platen acceleration components (sub-figures c-1 through c-3).

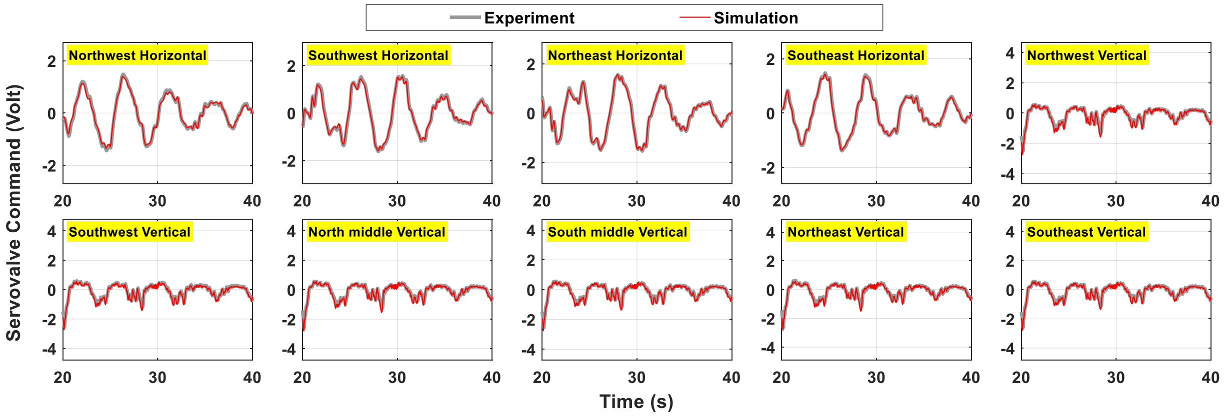

Figure 6.31 Comparison of closed-loop numerically simulated and experimental fourth-stage servovalve command time histories for each of the four horizontal and six vertical actuators in the case of the tri-axial earthquake ground motion test Nepal.

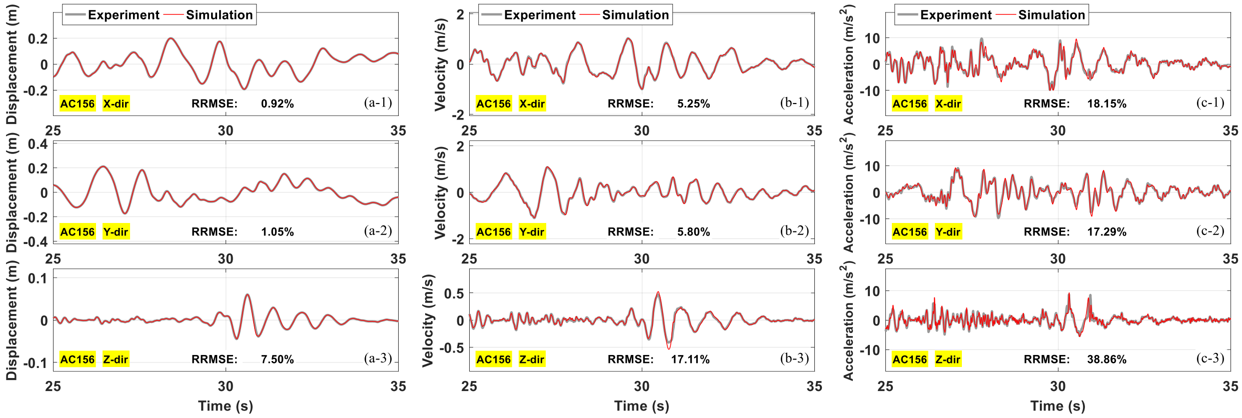

Figure 6.32 Comparison of closed-loop numerically simulated and experimental platen motion results for the tri-axial earthquake ground motion test AC156: time histories of platen displacement components (sub-figures a-1 through a-3), platen velocity components (sub-figures b-1 through b-3) and platen acceleration components (sub-figures c-1 through c-3).

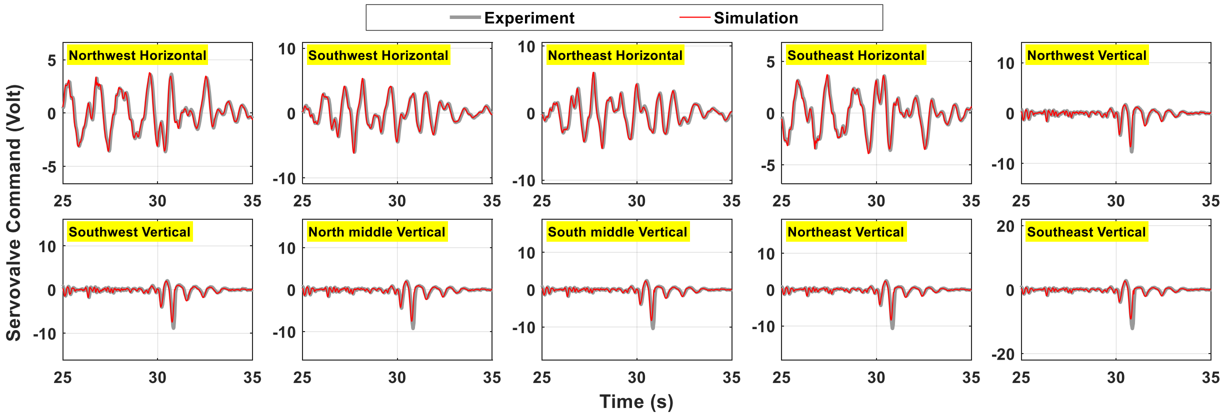

Figure 6.33 Comparison of closed-loop numerically simulated and experimental fourth-stage servovalve command time histories for each of the four horizontal and six vertical actuators in the case of the tri-axial earthquake ground motion test AC156.

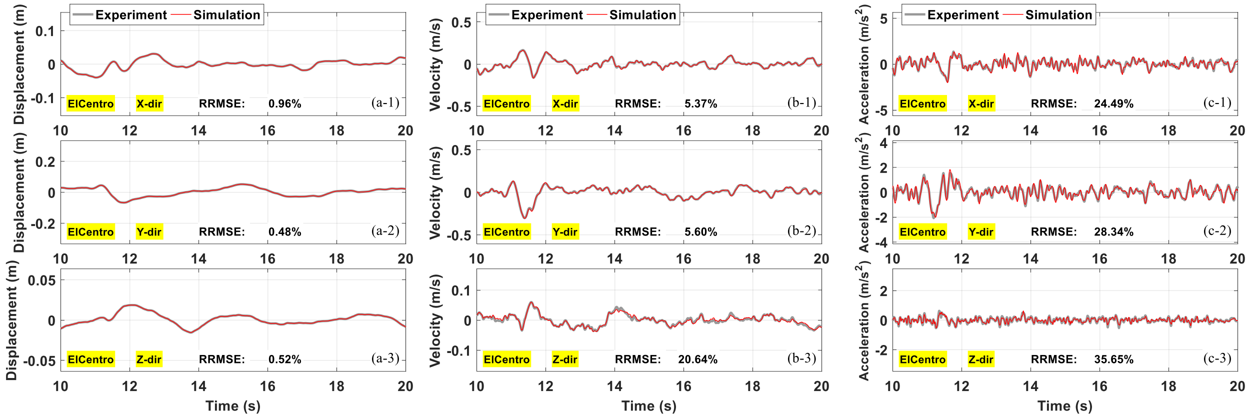

Figure 6.34 Comparison of closed-loop numerically simulated and experimental platen motion results for the tri-axial earthquake ground motion test El Centro: time histories of platen displacement components (sub-figures a-1 through a-3), platen velocity components (sub-figures b-1 through b-3) and platen acceleration components (sub-figures c-1 through c-3).

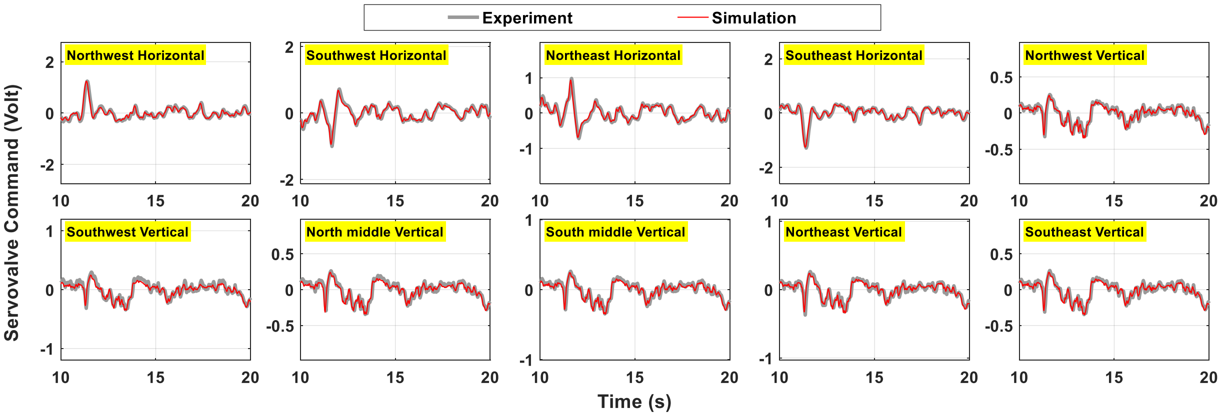

Figure 6.35 Comparison of closed-loop numerically simulated and experimental fourth-stage servovalve command time histories for each of the four horizontal and six vertical actuators in the case of the tri-axial earthquake ground motion test El Centro.

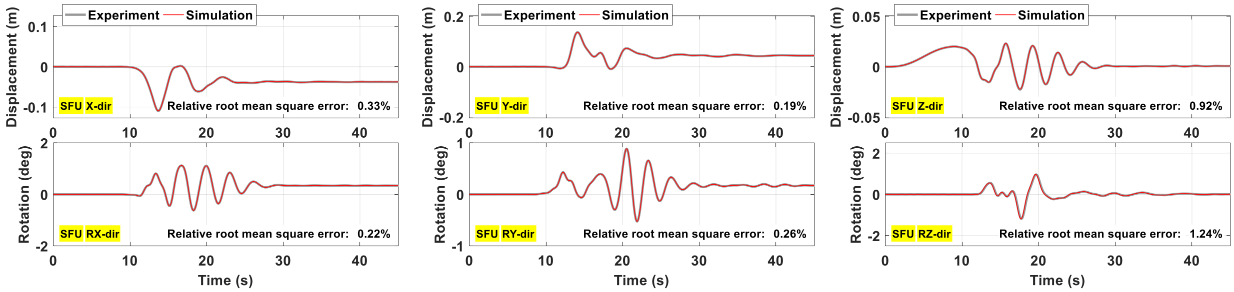

Figure 6.36 Comparison of closed-loop numerically simulated and experimental platen motion results for the synthetic six-axial earthquake ground motion test SFU: time histories of platen displacement (top 3 sub-figures) and rotation (bottom three sub-figures) components.

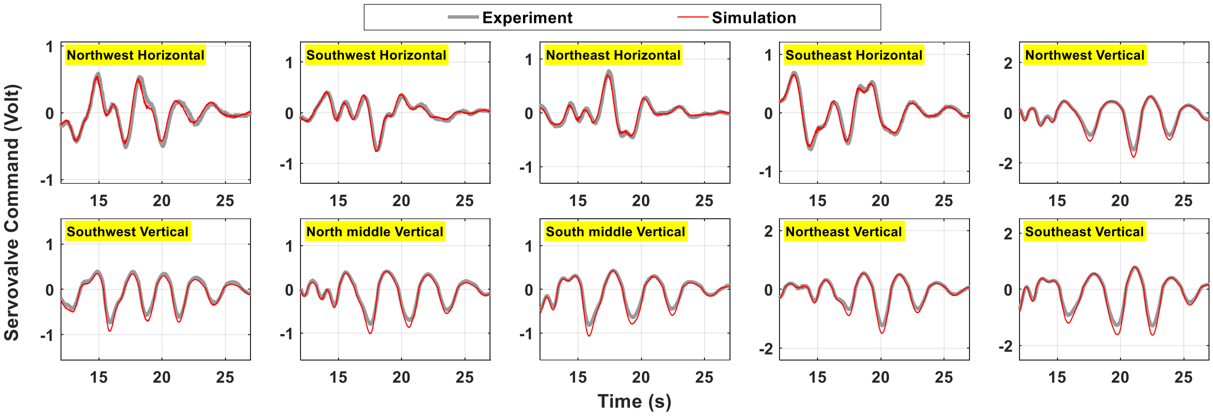

Figure 6.37 Comparison of closed-loop numerically simulated and experimental fourth-stage servovalve command time histories for each of the four horizontal and six vertical actuators in the case of the six-axial earthquake ground motion test SFU.

7 CONCLUSIONS

This report presents a mechanics-based numerical model of the NEHRI@UC San Diego Large High-Performance Outdoor Shake Table (LHPOST) in its six-degree-of-freedom configuration (LHPOST6) from its current upgrade and operating under bare table condition. This numerical model comprises several key components: (i) A rigid body kinematic model, defining the relationship between the shake table platen motion and the motions of attached components (horizontal and vertical actuators, hold-down struts). (ii) A hydraulic dynamic model utilizing Bernoulli's principle to calculate the flow through each servovalve based on its fourth-stage spool position, determining the hydraulic actuator forces governed by mass flow continuity of fluid in each actuator chamber. (iii) A hold-down strut (HDS) model to compute the forces exerted by the hold-down struts which prestress the platen against the top surface of the vertical actuators. This is based on the HDS displacements and assumes that the nitrogen gas in the bottom chamber behaves as an ideal gas following the polytropic process. (iv) A 2-D and various 1-D Bouc-Wen phenomenological models of hysteresis, representing sources of energy dissipation (i.e., dissipative forces) in the shake table system. (v) A 6-DOF rigid body dynamic model governing the platen motion under the total actuator, hold-down, and dissipative forces and moments acting on the platen. The equation of motion for the platen incorporates Newton's second law and Euler's rotation equation. It utilizes the platen twist (a six-component vector combining translational and rotational motions) as well as the platen wrench (a six-component vector combining forces and moments). The formulation employed here to describe the kinematics and dynamics of the 6-DOF rigid platen was adapted from the realm of robotic analysis. It has been noted for its efficacy in this context. The formulation utilized for the platen kinematics and dynamics is comprehensive and assumes large translations and rotations of the platen, despite the fact that the actual rotation capacity of the LHPOST6 is limited to a few degrees. This formulation necessitates the utilization of several reference frames (e.g., fixed frame, body frame, etc.) and transformations between them.

The numerical model of the LHPOST6 is validated through three phases of comparison studies: (I) In this phase, the inertia forces, total dissipative forces (obtained through inverse dynamics), and the hold-down strut restoring forces are simulated using the recorded/measured platen motion which is imposed on the model. The results indicate that the relevant sub-models and their parameter values effectively represent the characteristics of the LHPOST6, encompassing its inertial and dissipative properties, along with the gas model properties for the nitrogen inside the hold-down struts. The dissipative force sub-models integrated into the LHPOST6 model capture the total dissipative forces reasonably well, despite their complex physics and significantly lower magnitude compared to the inertial forces and hold-down strut restoring forces. (II) The open-loop simulation is performed by feeding the LHPOST6 model with the recorded fourth-stage servovalve commands of all hydraulic actuators obtained during shake table tests. The output, including the forces and moments acting on the platen and resulting platen motion, closely aligns with the corresponding experimental results. In the absence of closed-loop table motion control, small and gradually increasing drifts manifest in the simulated table displacement results. The small, constant offsets observed in the total actuator force simulation results may suggest discrepancies between the effective inertial and gravity masses of the horizontal actuators and hold-down struts, which are assumed to be equal in the numerical model. The simulation results exhibit stronger oil column resonance effects than the experimental results, which may suggest higher damping due to more hydraulic fluid leaking across actuator piston seals than expected. (III) The closed-loop simulation entails the utilization of the MTS 469D Digital Control System, employing the identical (optimal) drive signal and 469D controller settings as those recorded and saved during earthquake shake table tests conducted on the actual LHPOST6. The comprehensive comparative analysis between numerically simulated and experimental results for intermediate control signals (fourth-stage servovalve commands of all actuators) and system response (platen motion) demonstrate a high level of agreement, thereby validating the numerical model of the LHPOST6 system presented in this report.

The validated numerical model of the LHPOST6 serves various purposes, including: (1) Pre-test simulation (″dry-runs″) of shake table tests for example to assess the LHPOST6’s signal tracking performance before constructing the specimen. (2) Off-line tuning or pre-tuning of the shake table controller in a virtual setting with the specimen on the table. (3) investigation of table-specimen-control interaction (for example as a help to interpret results of shake table experiments) through coupling the LHPOST6 model (developed in Matlab/Simulink), the MTS 469D Digital Control System, and the numerical model of a specimen developed in another software platform. (4) Safe off-line training (shake table simulator) for shake table operators. (5) Development platform for next-generation shake table controllers.(6) Real-time hybrid shake table testing.

REFERENCES

Airouche, A., Bechtoula, H., Aknouche, H., Thoen, B. K., & Benouar, D. (2014). Experimental identification of the six DOF CGS, Algeria, shaking table system. *Smart Structures and Systems*, 13(1), 137-154. doi: 10.12989/sss.2014.13.1.137.

Asadi, F., & Sadati, S. H. (2018). Full dynamic modeling of the general Stewart platform manipulator via Kane's method. *Iranian Journal of Science and Technology, Transactions of Mechanical Engineering*, 42, 161-168. doi: 10.1007/s40997-017-0091-3.

Borgnakke, C. (2013). *Fundamentals of Thermodynamics*. John Wiley & Sons.

Cao, Y., Mavroeidis, G. P., & Ashoory, M. (2018). Comparison of observed and synthetic near-fault dynamic ground strains and rotations from the 2004 M_w 6.0 Parkfield, California, earthquake. *Bulletin of the Seismological Society of America*, 108(3A), 1240-1256. doi: 10.1785/0120170227.

Chase, J. G., Hudson, N. H., Lin, J., Elliot, R., & Sim, A. (2005). Nonlinear shake table identification and control for near-field earthquake testing. *Journal of Earthquake Engineering*, 9(04), 461-482. doi: 10.1080/13632460509350551.

Chen, P. C., Kek, M. K., Hu, Y. W., & Lai, C. T. (2018). Statistical reference values for control performance assessment of seismic shake table testing. *Earthquakes and Structures*, 15(6), 595. doi: 10.12989/eas.2018.15.6.595.

Constantinou, M., Mokha, A., & Reinhorn, A. (1990). Teflon bearings in base isolation II: Modeling. ASCE, *Journal of Structural Engineering*, 116(2), 455-474. doi: 10.1061/(ASCE)0733-9445(1990)116:2(455).

Conte, J. P., & Trombetti, T. L. (2000). Linear dynamic modeling of a uni-axial servo-hydraulic shaking table system. *Earthquake Engineering & Structural Dynamics*, 29(9), 1375-1404. doi: 10.1002/1096-9845(200009)29:9<1375::AID-EQE975>3.0.CO;2-3.

Dasgupta, B., & Mruthyunjaya, T. S. (1998). Closed-form dynamic equations of the general Stewart platform through the Newton–Euler approach. *Mechanism and Machine Theory*, 33(7), 993-1012. doi: 10.1016/S0094-114X(97)00087-6.

Dasgupta, B., & Mruthyunjaya, T. S. (2000). The Stewart platform manipulator: a review. *Mechanism and Machine Theory*, 35(1), 15-40. doi: 10.1016/S0094-114X(99)00006-3.

Dyke, S. J., Spencer Jr, B. F., Quast, P., & Sain, M. K. (1995). Role of control-structure interaction in protective system design. ASCE, *Journal of Engineering Mechanics*, 121(2), 322-338. doi: 10.1061/(ASCE)0733-9399(1995)121:2(322).

Featherstone, R. (2014). *Rigid Body Dynamics Algorithms*. Springer. doi: 10.1007/978-1-4899-7560-7.

Guo, H. B., & Li, H. R. (2006). Dynamic analysis and simulation of a six degree of freedom Stewart platform manipulator. *Proceedings of the Institution of Mechanical Engineers, Part C: Journal of Mechanical Engineering Science*, 220(1), 61-72. doi: 10.1243/095440605X32075.

Guo, W., Shao, P., Li, H. Y., Long, Y., & Mao, J. F. (2019). Accuracy assessment of shake table device on strong earthquake output. *Advances in Civil Engineering*, 2019(1), 9372505. doi: 10.1155/2019/9372505.

Huang, Y., Pool, D. M., Stroosma, O., Chu, Q. P., & Mulder, M. (2016). Modeling and simulation of hydraulic hexapod flight simulator motion systems. In *AIAA modeling and simulation technologies conference* (p. 1437). doi: 10.2514/6.2016-1437.

Harib, K., & Srinivasan, K. (2003). Kinematic and dynamic analysis of Stewart platform-based machine tool structures. *Robotica*, 21(5), 541-554. doi: 10.1017/S0263574703005046.

ICC Evaluation Services Inc. (2007). ICEE-ES AC 156, Acceptance Criteria for Seismic Qualification by Shake-Table Testing of Non-Structural Components and Systems. Whittier, CA.

Kusner, D. A., Rood, J. D., & Burton, G. W. (1992, July). Signal reproduction fidelity of servohydraulic testing equipment. *Proceedings*, *10th World Conf. on Earthquake Engineering* (pp. 2683-2688).

Kvrgic, V., & Vidakovic, J. (2020). Efficient method for robot forward dynamics computation. *Mechanism and Machine Theory*, 145, 103680. doi: 10.1016/j.mechmachtheory.2019.103680.

Lai, C. T. Yeh, S. W., Weng, P. W., Hsiao, F. P., Huang B. Y. (2022). Kinematics and identification study applied to the shaking table by using the actuator measurement: Take MAST for example. *Structural Engineering*, 37(3), 81-104. doi: 10.6849/SE.202209_37(3).0005.

Lebret, G., Liu, K., & Lewis, F. L. (1993). Dynamic analysis and control of a Stewart platform manipulator. *Journal of Robotic Systems*, 10(5), 629-655. doi: 10.1002/rob.4620100506.

Liu, M. J., Li, C. X., & Li, C. N. (2000). Dynamics analysis of the Gough-Stewart platform manipulator. *IEEE Transactions on Robotics and Automation*, 16(1), 94-98. doi: 10.1109/70.833196.

Luco, J. E., Ozcelik, O., & Conte, J. P. (2010). Acceleration tracking performance of the UCSD-NEES shake table. ASCE, *Journal of Structural Engineering*, 136(5), 481-490. doi: 10.1061/(ASCE)ST.1943-541X.0000137.

Lynch, K. M., & Park, F. C. (2017). *Modern Robotics*. Cambridge University Press.

Merritt H. *Hydraulic Control Systems* (1967). New York: John Wiley & Sons.

Nakashima, M., Nagae, T., Enokida, R., & Kajiwara, K. (2018). Experiences, accomplishments, lessons, and challenges of E-defense—Tests using world's largest shaking table. *Japan Architectural Review*, 1(1), 4-17. doi: 10.1002/2475-8876.10020.

Ozcelik, O., Conte, J. P., & Luco, J. E. (2021). Comprehensive mechanics-based virtual model of NHERI@ UCSD shake table—Uniaxial configuration and bare table condition. *Earthquake Engineering & Structural Dynamics*, 50(12), 3288-3310. doi: 10.1002/eqe.3510.

Ozcelik, O., Luco, J. E., & Conte, J. P. (2008). Identification of the mechanical subsystem of the NEES-UCSD shake table by a least-squares approach. ASCE, *Journal of Engineering Mechanics*, 134(1), 23-34. doi: 10.1061/(ASCE)0733-9399(2008)134:1(23).

Ozcelik, O., Luco, J. E., Conte, J. P., Trombetti, T. L., & Restrepo, J. I. (2008). Experimental characterization, modeling and identification of the NEES-UCSD shake table mechanical system. *Earthquake Engineering & Structural Dynamics*, 37(2), 243-264. doi: 10.1002/eqe.754.

Park, Y. J., Ang, A. H. S., & Wen, Y. K. (1985). Seismic damage analysis of reinforced concrete buildings. *Journal of Structural Engineering*, 111(4), 740-757. doi: 10.1061/(ASCE)0733-9445(1985)111:4(740).

Plummer, A. R. (2008). A detailed dynamic model of a six-axis shaking table. *Journal of Earthquake Engineering*, 12(4), 631-662. doi: 10.1080/13632460701457264.

Suzuki, T., Puranam, A. Y., Elwood, K. J., Lee, H. J., Hsiao, F. P., & Hwang, S. J. (2021). Shake table tests of seven-story reinforced concrete structures with torsional irregularities: Test program and datasets. *Earthquake Spectra*, 37(4), 2946-2970. doi: 10.1177/87552930211016869.

Thoen, B. K., & Laplace, P. N. (2004, August). Offline tuning of shaking tables. *Proceedings, 13th World Conference on Earthquake Engineering*.

Van Den Einde, L., Conte, J. P., Restrepo, J. I., Bustamante, R., Halvorson, M., Hutchinson, T. C., Lai, C.-T., Lotfizadeh, K., Luco, J. E., Morrison, M. L., Mosqueda, G., Nemeth, M., Ozcelik, O., Restrepo, S., Rodriguez, A., Shing, P. B., Thoen, B., & Tsampras, G. (2021). NHERI@ UC San Diego 6-DOF large high-performance outdoor shake table facility. *Frontiers in Built Environment,* 6, 580333. doi: 10.3389/fbuil.2020.580333.

The Pacific Earthquake Engineering Research Center (PEER) is a multi-institutional research and education center with headquarters at the University of California, Berkeley. Investigators from over 20 universities, several consulting companies, and researchers at various state and federal government agencies contribute to research programs focused on performance-based earthquake engineering.

These research programs aim to identify and reduce the risks from major earthquakes to life safety and to the economy by including research in a wide variety of disciplines including structural and geotechnical engineering, geology/seismology, lifelines, transportation, architecture, economics, risk management, and public policy.

PEER is supported by federal, state, local, and regional agencies, together with industry partners.

PEER Core Institutions

University of California, Berkeley (Lead Institution)
California Institute of Technology
Oregon State University
Stanford University
University of California, Davis
University of California, Irvine
University of California, Los Angeles
University of California, San Diego
University of Nevada, Reno
University of Southern California
University of Washington

Pacific Earthquake Engineering Research Center
University of California, Berkeley
325 Davis Hall, Mail Code 1792
Berkeley, CA 94720-1792
Tel: 510-642-3437
Email: peer_center@berkeley.edu

ISSN 2770-8314
https://doi.org/10.55461/JSDS5228